Numerical Investigations of Spin Waves at the Nanoscale

by

Mykola Dvornik

Submitted to the University of Exeter

as a thesis for the degree of

Doctor of Philosophy in Physics

In September 2011

I certify that all material in this thesis which is not my own work has been identified and that no material has previously been submitted and approved for the award of a degree by this or any other university.

Signature: ……..

Magnetic Materials Group

University of Exeter

To the bright light at the end of the dark corridors of physics

To my endless love

To you, Annutka

Abstract

This thesis contains results of numerical investigations of magnetisation dynamics in nanostructed ferromagnetic materials. Magnetic systems have been simulated using the open source micromagnetic solver: Object Oriented Micromagnetic Framework (OOMMF), and thoroughly analysed using my own software: *semargl*.

A systematic study of collective magnonic modes confined in 2D and 3D systems of rectangular ferromagnetic nano-elements is presented. The collective character of the excitations results from the dynamic magnetic dipole field. The magnetization dynamics of isolated rectangular elements is found to be spatially non-uniform which means that the dynamic dipolar coupling is highly anisotropic. A semi-analytical theory of collective magnonic modes has been developed to evaluate the properties of the dynamic magnetic dipole field. It was found that the theory is only valid for certain eigenmodes of the isolated element. In particular the modes where the magnetic dipole coupling between the elements is much lower than the internal energy of the corresponding eigenmodes of the isolated element.

It is then demonstrated that the confinement of spin waves is strongly affected by the ground state of the system. In particular it has been found that symmetry

properties of the topology of 2D arrays affect the dynamics of the strongly localised modes. The effect is found to be significant for arrays of any number of elements. At the same time the relative contribution of the localized modes to the uniform response decreases with the number of elements in the array.

The dispersion relation of spin waves in 2D arrays of rectangular nano-elements has been calculated for the first time using micromagnetic simulations. The form of the dispersion is used to estimate the spatial anisotropy of the dynamic dipolar coupling.

Simulations of the 3D confinement of spin waves in stacks of magnetic nano-elements have been performed. The calculation of both the dispersion and spatial profiles of the corresponding magnonic modes facilitates the investigation of the localisation of collective spin waves. Furthermore the dispersion of collective magnonic modes has been calculated for stacks of rectangular nano-elements for a range of in-plane aspect ratios.

Finally, a numerical method has been developed to extract the scattering parameters of magnonic logic devices. This method has been demonstrated by applying it to the simplest possible magnonic device so that the results could be compared to an analytical expression of the scattering parameters.

Table of Contents

Table of Figures and Tables

Acknowledgments

Thanks to everyone all over the world. We are all connected together, so that we can share, get or lose.

The special “thank you” to the one I love. Without you my world would be dark and eyes blind. Please forgive me for all these physics.

Thanks to my family, my father Oleksandr Dvornik, my mother Natalya Dvornik and my awesome brother Kostyantyn Dvornik. They brought me to life and changed it in a right direction when it was necessary. They always listen to and understand me no matter what a tough person I am. My brother, man, you will always be my best friend and the person of my strongest believe.

Thanks to my school and lyceum teachers. You were always supporting me in my beginnings and mistakes. I cannot imagine me doing physics without that educational route which I undertake.

Many thanks to Prof. Andrei Kuchko and Prof. Igor Lyubchanskii for their help during my Master degree course. I did a lot of mistakes at that time, but only now I have

realized this. Thanks to Prof. Vladimir Yurchenko who suggested that I would never obtain PhD degree. Nevertheless it was a great fun when I was arguing with you. I was lucky to study in a group of Dr. Victor Finokhin, the person of my endless respect for the depth of his knowledge of physics.

Many thanks to our collaborators Pavlo Bondarenko and Prof. Boris Ivanov, your emails with analytical theories keep my theoretical background alive.

Thanks everybody in the Magnetic Materials Group of University of Exeter for the warm environment. Special thanks to Dr. Paul Keatley, who was my office-mate for almost a year. I think he is now 10% Ukrainian and I am 20% English. I hope that our future collaboration will be as good as it was during my PhD. Special thanks to Max Marcham for reading trough this manuscript and proofing it.

Without any doubts my supervisor Dr. Volodymyr Kruglyak is the one who offers me the biggest opportunity in my life. The one who did all these things to me that turns me in a proper researcher. I THANK YOU for all of these.

Finally, thanks to the European FP7 projects DYNAMAG and MAGNONICS and Overseas Research Studentship scheme and University of Exeter for the financial support of the work presented here.

Declaration

The numerical results presented in this manuscript reflect the work of me (the author of the manuscript) and my supervisor Dr Volodymyr Kruglyak. The analytical theories in Section V have been developed by Pavlo Bondarenko and Prof Boris Ivanov. The contributions (of my collaborators to this work) are outlined below for each chapter.

Chapter II: Background

This chapter contains my own work. Some of the images are taken from the previously published works of other authors. Where this is the case I have referenced the authors accordingly.

Chapter III: Object Oriented Micromagnetic Framework

This chapter contains my own work. The technical details about the implementation of OOMMF have been extracted from the OOMMF userguide, which is referenced.

Chapter IV: Semargl: A Tool for Advanced Processing of Real Space Sampled Data

This chapter represents my own work. All the figures have been extracted from simulations performed by myself.

Chapter V: Collective precessional modes of pairs of closely spaced magnetic nano-elements

The numerical simulations presented in the chapter were performed by myself. The theory of collective modes of arrays of magneto-dipolar coupled magnetic elements has been developed by Pavlo Bondarenko and Prof. Boris Ivanov.

Chapter VI: Collective magnonic modes in finite sized 2D arrays of magnetic nano-elements

The numerical simulations presented in the chapter were performed and analysed by myself.

Chapter VII: Localized magnon states in finite stacks of magnetic nanoelements

The results in this chapter have been obtained entirely by myself. An estimation of the critical value for the ellipticity was performed by myself using the theory of collective modes of arrays of magneto-dipolar coupled magnetic elements that has been developed by Pavlo Bondarenko and Prof. Boris Ivanov.

The main contributor to the results presented in this thesis (except the author) is my PhD supervisor Dr. V. V. Kruglyak. He is responsible for the formulation of the physical problems solved here within.

I Introduction

Many aspects of the modern world require an enormous amount of computational power to be available to the user. With increases in computational power frequently opening previously inaccessible avenues of investigation and implementation, the impact that the continued improvement in computing power has on advancement of the modern world is clear. In particular, as life becomes more *'digital'*, more storage space and computational resources are required to satisfy the needs of each individual. However, semiconductor technology is fast approaching its inherent limits. According to studies of the various semiconductor vendors downscaling of semiconductor transistors cannot be done below 16 nm[1], while industry already has reached the value of 32 nm. According to the Moore's law[2] the transistor packing density increases by approximately a factor of two every two years. Therefore it is expected that in the upcoming few years this well-known law will be broken. Thus alternatives to semiconductor technology are required if the progress predicted by Moore's law is to continue. The possible alternatives to semiconductor technology are: quantum computing[3], graphene technology[4], optical computing[5] and bio-computing[6]. Essentially, only graphene technology can adopt the ecosystem of semiconductor

technology (by replacing semiconductor transistors with those made using graphene[7]). In contrast, other technologies require a completely new approach to computation[8].

Meanwhile it is known that spin waves (periodic disturbances in the order of magnetic moments in magnetic materials) have characteristic frequencies in the gigahertz[9] and sub-terahertz[10] bands. Thus, it is expected that spin waves could be utilized in computer processors with high computational performance. This could potentially increase the computational power of computers as their performance is generally fixed by their clock rates[11]. Spin wave devices could be either integrated into semiconductor chips (by means of hybrid chips) or pure spin wave architecture could be developed. The latter is the preferred solution as no additional spin wave-to-current (and vice versa) conversion would be required. Such a conversion could potentially reduce the performance of the circuit and increase its power consumption due to the finite efficiency of the conversion. Nevertheless, if required, the conversion could be done by several methods, for instance by utilizing the inverse spin Hall effect[12], spin Seebeck effect[13] or by using spin transfer torque oscillators[14]. It has been shown numerically that digital logic devices could be realised using spin waves[15]. Moreover it has been found that by utilising so-called "magnonic crystals" (magnetic media with periodic modulation of the magnetic parameters) it is possible to process analogue signals in the gigahertz band without the need for additional conversion of the frequency or analogue to digital conversion of the signal, as is the case for the existing semiconductor technology. This ensures higher performance and dynamic range. In particular, signal filters and delay lines have been demonstrated experimentally[16] and numerically[17]. The main advantage of these devices over semiconductor devices is that it is possible to tune them using an externally applied magnetic field. Semiconductor devices on the other hand cannot be easily tuned and usually operate within fixed frequency bands. The other advantage is that the dynamic properties of the magnetic structure can be tuned by

patterning the magnetic medium[18]. The magnetic interactions have a very complex anisotropic character and therefore even minor changes of the geometry of the magnetic structures could result in significant changes of their dynamic properties.

The very complex structure of the magnetic energies of magnetic nano-systems is also the subject of fundamental research. The main properties of spin waves have been studied extensively in systems supporting collective magnonic modes, such as 1D[19], 2D[20] and 3D arrays[18] of magnetic nano-elements. It has been found that the dispersion of collective spin waves in such structures is strongly anisotropic. Moreover the form of the dispersion is found to be dependent on the history of the applied field, an effect known as hysteresis. Therefore, it can be concluded that the behaviour of such magnetic systems has several degrees of freedom and that each of these is of a very complex nature. Moreover, spin waves are found to interact with different excitations of the lattice such as phonons[21] and excitons[22]. Furthermore, in metals spin waves interact with free electrons, which typically enhance the spin wave relaxation[23].

The dynamics of spin waves is described by the non-linear Landau-Lifshitz equation[24] and a wide range of non-linear effects has been observed[25,26,27,28]. Some of these effects (such as the self-focusing of spin waves[25]) have analogues in non-magnetic structures and are due to the strong anisotropy of magnetic interactions in the aforementioned systems. Finally, the Bose-Einstein condensation of magnons (the quanta of spin waves) has been observed recently[29]. Nevertheless, the dynamical properties of the Bose-Einstein condensate of magnons have not been studied numerically so far.

As lasers operating on femtosecond timescales are now available it is possible to investigate spin waves on timescales of hundreds of femtoseconds[30]. In particular it is possible to switch the magnetization on timescales of around 100 fs, a process that

cannot be described by the theory developed by Landau and Lifshitz[31]. Such processes typically involve the modification of the electronic structure of the magnetic materials and so have to be addressed by a quantum approach.

Despite the fact that the majority of observed effects involving spin waves could be described by the Landau-Lifshitz equation it does not allow one to derive the analytical solution in most cases. Moreover, the ground state of nanoscale magnetic structures is typically non-uniform. This makes the form of the Landau-Lifshitz equation even more complicated. Thus for some cases only numerical solutions can be evaluated, and so there are a growing number of numerical studies on the topic of spin waves as magnonics (the study about spin waves) continues to develop[32].

In this thesis I present examples of numerical studies performed in the magnonics group of the University of Exeter in collaboration with the Institute of Magnetism and Donetsk National University in Ukraine. I developed a set of unique methods developed by myself and my supervisor Dr. Volodymyr Kruglyak. These methods have allowed us to numerically study several magnetic systems in ways commonly adopted in the other fields of solid state physics. It will be demonstrated that problems typically addressed by analytical theories can also be solved using numerical calculations. Lastly, I will show how numerical simulations can be used to predict new results in the field of magnonics.

Chapter II describes the theoretical background of the topic of magnetism. Although the described theoretical results have been derived for bulk materials or infinite thin films they are crucial in understanding spin wave phenomena on the nanoscale. Moreover, they serve to illustrate that a full theoretical description of magnetic systems is an involved and complex task.

Chapter III describes the numerical tool used in our studies – the Object Oriented Micromagnetic Framework (OOMMF) and the main principles and methods of the numerical calculations that were performed are presented. Finally a comparison of OOMMF with other numerical tools is presented in attempt to demonstrate that OOMMF has the highest degree of versatility and performance currently available.

Chapter IV describes the numerical methods developed by myself and Dr. Volodymyr Kruglyak to analyse the results of our numerical calculations. The software used to implement said numerical methods has been developed by myself during my PhD. Each method is accompanied by examples of the analysis so that the reader can understand how the method should be applied. In addition an insight into the architecture of the developed software is provided to illustrate to the reader that our software provides unique options for data analysis as well as having outstanding computational performance.

Chapter V describes the numerical and theoretical study of several dynamic properties of pairs of magnetic nano-elements. The spatial anisotropy of the dynamic dipolar coupling is addressed in this study. It has been found that despite the simplicity of the investigated system the latest theoretical approach does not fit with the numerical observations for the various parameters of the system.

Chapter VI describes the study of collective oscillations of 2D arrays of magnetic nano-elements and thereby extends the study presented in Chapter V. In particular we have found that the frequencies of the localised modes of the arrays are strongly correlated with the parity of the array (in terms of the number of elements in one column of the array). Additionally, we have found that some eigenmodes of the elements comprising the array have a non-rigid character, and so their spatial profile can be altered by strong inter-element interaction. Thus, when the elements form a closely

packed array, the eigenstates of the elements change, and so the collective bands of the arrays may not simply originate from the eigenstates of the isolated element.

Chapter VII represents a numerical study of the 3D confinement of spin waves in stacks of magnetic nano-elements. In particular we have found that the sign of the dispersion of collective spin waves is strongly correlated with the ellipticity of the eigenmodes of the isolated nano-element. Moreover we have found that the finite width of the magnonic bands results in localisation of spin waves in the regions of increased internal field.

Chapter VIII describes a method of numerical calculation that facilitates the extraction of the scattering parameters of the system. This method could be used to characterise magnonic devices in a way similar to that used to characterise modern day electronics. The scattering parameters could be measured experimentally by Vector Network Analyser Ferromagnetic Resonance (VNA-FMR) technique[33]. The results presented in this chapter also highlight the limitations of numerical calculations and provide some insight into the areas where a classical theoretical approach could be implemented. Finally we have found that imperfections in magnetic systems could cause an accumulation of the energy of the propagating spin waves resulting in the formation of localised modes. This effect has been observed experimentally[34], however the experimental work on this topic is still an emerging field.

II Background

II.1 History of magnetism

It has long been known that particular materials show magnetic properties. Nevertheless the first step towards a quantitative understanding of this phenomenon was made only in the 19th century by Ampere. He discovered that circulating currents are responsible for the creation of magnetic fields. He therefore attributed the magnetic properties to the presence molecular currents of unknown nature. An attempt was then made by Langevin[35] and Weiss[36], independently, to make a quantitative theory of paramagnetic and ferromagnetic properties of materials. Langevin introduced an empirical theory of paramagnetism based on the assumption that only the external field acts on the magnetic moments of the paramagnetic material resulting in a small net magnetic moment in the direction of the applied field. In order to explain the significant net magnetic moment of ferromagnets Weiss introduced so-called "molecular fields" that are proportional to the net magnetic moment of the ferromagnets. However, the origin of the molecular fields has not been explained. The first explanation for the origin of the molecular field was made by Frenkel[37] and Heisenberg[38] based on the principles of quantum mechanics. In fact, the electrostatic (Coulomb) interaction between two

electrons depends on the relative orientation of their spins. The corresponding part of the Coulomb interaction is the so-called exchange interaction. This follows from the Pauli principle and the fact that wave functions (or "electron clouds") of the atoms (molecules) overlap. In ferromagnets the minimum exchange interaction energy is realised when the spins are parallel to each other, therefore the exchange interaction is responsible for the magnetic ordering observed in ferromagnetic materials. Usually the exchange interaction is found to be isotropic. Therefore the exact orientation of the net magnetization is attributed to the presence of other magnetic interactions. In particular it is related to the energy of the magnetocrystaline anisotropy (Akulov[39]) and magnetic-dipole interaction (Frenkel[40] and Heisenberg[41]). The interplay between these interactions is responsible for the spatial configuration of the magnetisation in ferromagnetic samples.

Furthermore, it was found that ferromagnetic materials support dynamic behaviour of the magnetization. Landau and Lifshitz developed a phenomenological theory to describe the dynamics and relaxation in ferromagnetic materials[31]. The Landau – Lifshitz theory predicts, that the ground state of the magnetic system is realized when the magnetization $\mathbf{M}(\mathbf{r})$ is parallel to the so-called "internal field" of the ferromagnet, $\mathbf{H}_{int}(\mathbf{r})$.

The theory developed by Landau and Lifshitz is phenomenological and is based on classical principles. More strict phenomenological theory based on the principles of quantum mechanics was later proposed by Heisenberg[42] and Holstein and Primakoff[43].

II.2 Paramagnets

Paramagnetic materials show an increase of the net magnetic moment when subject to external magnetic field. This effect is attributed to the fact that atoms of the paramagnetic elements have non-compensated electron spins, as required by the Pauli principle, thus each atom has a non-zero magnetic moment. The interaction energy between the magnetic moments of different atoms is smaller than the thermal energy. This means that in the absence an applied field the orientation of the magnetic moments is highly disordered and the net magnetic moment vanishes. When a magnetic field, of magnitude *H,* is applied the magnetic moments align along the direction of the applied field due to the Zeeman interaction and the net magnetic moment no longer vanishes (Figure II.2-1).

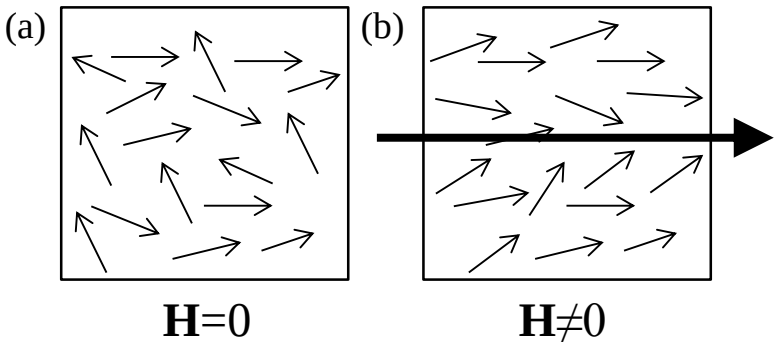

Figure II.2-1 Schematics of the paramagnetic order in the absence (a) and presence (b) of an applied magnetic field.

Langevin derived a simple expression that relates the magnetic moment of the unit atom (M_0) with the net magnetic moment of the paramagnet (M) as given by

$$M = NM_0 L\left(\frac{M_0 H}{k_B T}\right) \qquad \text{(II.2-1)}$$

where N is the total number of atoms in the system and $L(x) = coth(x) - \frac{1}{x}$ is the Langevin function. In the high temperature limit $T \to \infty$ the Langevin function becomes zero $L(x) \to 0$. In contrast, for low temperature $T \to 0$ the Langevin function approaches to unity $L(x) \to 1$. Thus either by increasing the value of the applied field or by decreasing the temperature of the sample it is possible to align the magnetic moments along a given direction so that the net moment will reach the value of NM_0.

The paramagnetic susceptibility of paramagnets, χ, is inversely proportional to the temperature and is defined by *Curie's law* as

$$\chi = \frac{C}{T} \tag{II.2-2}$$

where $C = \frac{NM_0^2}{3k_B}$ is a constant. For paramagnetic materials χ is small and is in the range of $10^{-5}$to 10^{-3}.

According to quantum theory, in the absence of a magnetic field, states with different projections of the magnetic moment on a given axis are degenerate. When an external magnetic field is applied, the degenerate states split into levels separated by intervals of

$$\delta E = \gamma \hbar H, \tag{II.2-3}$$

where γ and $\hbar$ are the gyromagnetic ratio and the reduced Planck's constant, respectively. Transitions between these states as a result of the absorption of photons of energy $\hbar\omega$ is known as electron paramagnetic resonance. The resonant condition is given by

$$\omega_H = \gamma H. \tag{II.2-4}$$

II.3 Ferromagnets

In contradistinction to paramagnetic materials, there is a class of materials that can have a significant net magnetic moment without the presence of an externally applied magnetic field. Such materials are called ferromagnets. It follows that there is a magnetic interaction between the magnetic moments of the system that leads to the observed magnetic ordering. Weiss attempted to quantitatively describe the phenomenon of ferromagnetism by expanding the theory developed by Langevin. In particular he introduced molecular fields in the form of

$$H_m = \Lambda M \tag{II.3-1}$$

where Λ is a large constant. The molecular fields are assumed to be specific to the ferromagnetic materials. The net magnetic moment of the system is now defined by

$$M = NM_0 L\left(\frac{M_0(H+\Lambda M)}{k_B T}\right). \tag{II.3-2}$$

Thus the susceptibility is given by

$$\chi_f = \frac{C}{T-T_c}, \tag{II.3-3}$$

where T_c is known as the Curie temperature. Above this temperature ferromagnets lose their magnetic ordering and become paramagnetic. This effect can be explained by the fact that the energy of the thermal motion of the magnetic moments overcomes that responsible for the ferromagnetic ordering.

Despite the fact that the Weiss theory gives some quantitative agreement with the experiment it does not give an explanation of the origin of the molecular fields on which it relies. Moreover it does not predict the direction of the net magnetic moment of the system.

II.4 Exchange interaction

The energy of the dipolar coupling of two magnetic moments is small compared to the thermal energy kT. Therefore at room temperature the magnetic dipole interaction cannot be responsible for the magnetic ordering observed in ferromagnets. Nevertheless, the Coulomb interaction of two electrons separated by the same distance as the magnetic dipoles described above is large enough to overcome the energy of the thermal motion.

Quantum mechanics predicts that the mean energy of the Coulomb interaction of two electrons depends on the relative orientation of their spins. Electrons are Fermions and so are subject to the Pauli Exclusion Principle which states that no two indistinguishable fermions can occupy the same quantum state. Thus the exact form of the wavafunction of system of electrons depends on the spin coordinates.

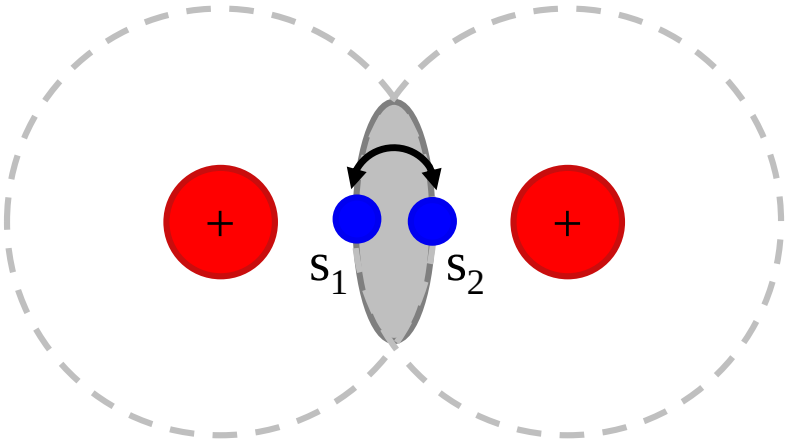

Figure II.4-1 Schematic representation of the exchange interaction between two atoms.

Let us consider a molecule consisting of two atoms[46]. If the wave functions of the electrons of the two atoms overlap, then there is a possibility for the electrons to be

exchanged within the two atoms (Figure II.4-1). According to the Pauli principle, this process changes the spatial form of the wave function of the molecule.

In cases of magnetic interaction of electrons spins could be neglected, the wavefunction of the system of interacting atoms (molecules) could be expressed as a dot product of spatial and spin dependant parts, which are independent from each other. It is worth to point that according to Pauli principle, the full wavefunction (consisting of spatial and spin-dependant parts) is anti-symmetric with respect to the coordinates and spins. Therefore, anti-symmetric spin-dependant part corresponds to the symmetric spatial and vice-versa. In other words, total spin of the exchanged electrons defines the symmetry of the spatial wavefunction. If the total spin of the system is either $S = s_1 + s_2 = 0$ or $S = s_1 + s_2 = 1$, then the spatial part of the wavefunction of the molecule becomes either anti-symmetric or symmetric respectively. Such modifications to the form of the wavefunction change the energy state of the molecule. Microscopically configurations with different total spin localizes in different points of the space, thereby enhancing or reducing Coulomb interaction.

Van Vleck[44] derived the expression for the energy of the exchange interaction

$$E_{ex} = C - \frac{1}{2}J_{ex}(\mathbf{r}) - 2J_{\alpha\beta}(\mathbf{r})s_\alpha s_\beta, \qquad \text{(II.4-1)}$$

where C and J_{ex} are constants and $J_{\alpha\beta}$ is the so-called exchange integral, and characterises the type and strength of the interaction between the two spins. Dirac[45] showed that the first two terms in (II.4-1) could be neglected as they are independent of the spins of the interacting electrons, so that the exchange interaction between two spins becomes

$$E_{ex} = -2J_{\alpha\beta}(\mathbf{r})s_\alpha s_\beta, \qquad \text{(II.4-2)}$$

Therefore if $J_{\alpha\beta}(\mathbf{r}) > 0$, then the exchange energy is minimised when the two spins are parallel. Such magnetic ordering corresponds to the ferromagnetic state. In contrast, if $J_{\alpha\beta}(\mathbf{r}) < 0$, then the exchange energy minimum is realised for the anti-parallel orientation of the two spins. This state corresponds to anti-ferromagnetic ordering. It is worth noting that the exchange integral $J_{\alpha\beta}(\mathbf{r})$ decays rapidly with distance, as the overlapping between electron orbits of interacting atoms (molecules). Therefore the exchange interaction is a local phenomenon, and so only the neighbouring atoms can effectively interact via the exchange interaction.

The macroscopic expression for the exchange interaction energy can also be derived phenomenologically[46] by expressing density of exchange energy into Taylor series. By taking into account symmetry of the magnetisation with respect to time and assuming that sample is infinite, the exchange energy takes the form of

$$W = \int_V \frac{1}{2}\alpha_{ij}\frac{\partial \mathbf{M}}{\partial x_i}\frac{\partial \mathbf{M}}{\partial x_j}d\mathbf{r}, \tag{II.4-3}$$

where α_{ij} is a second-rank tensor that denotes the strength of the exchange interaction. The vector multiplication is dot product if it is not stated otherwise. If the material is isotropic then the second-order tensor reduces to a scalar: α. The components of the exchange tensor are related to the exchange integral by

$$\alpha_{ij} \sim \frac{J_0}{4\mu_0^2}a^5, \tag{II.4-4}$$

where J_0 is the exchange integral of the neighbouring atoms and a is the lattice constant of the material.

Expressions (II.4-2) and (II.4-3) apply to the case of a direct exchange interaction. However in most ferromagnets the magnetic moments are placed at large distances from each other, and so they cannot interact directly due to the highly

localised nature of the exchange interaction. In ionic crystals, e.g. Yttrium Iron Garnet (YIG), the exchange interaction is realised through the anions placed in between the interacting magnetic moments. In contrast the exchange interaction in metals propagates via conducting electrons. Nevertheless, the form of the exchange interaction remains the same for any type of indirect exchange interaction, while the value of the exchange integral (exchange tensor) should be renormalized.

Despite the fact that the exchange interaction is responsible for the magnetic ordering some ferromagnetic materials do not show a net magnetic moment in the absence of an applied magnetic field. This phenomenon is related to the formation of magnetic domains[47] whereby the entire volume of the ferromagnet is subdivided into sub regions known as magnetic domains. Such domains are characterized to a first approximation by a parallel alignment of the magnetic moments within their volume - the relative orientation of the magnetic moments within a domain can vary. The formation of magnetic domains cannot be explained in terms of the exchange interaction detailed above.

II.5 Magnetic dipole energy

Although the exchange interaction is responsible for the magnetic ordering of the system it is independent of the orientation of the ordered spins relative to the crystallographic axes. Therefore the exchange interaction cannot lead to the steady state of the magnetic system.

In addition to the strong and short range exchange interaction, there is another class of relatively weak but important magnetic interactions that should be considered. These interactions are anisotropic, which means that the equilibrium magnetization has

preferred orientations (directions that correspond to the minimum of the energy of the interactions). These interactions define the ground state of the system.

The first and most important of these weak interactions is the magnetic dipole (or simply dipole) interaction. The dipole interaction is due to the fact that each atom of the magnetic material has a dipole moment, so that the atoms interact as an array of magnetic dipoles, given by

$$E_d = \frac{1}{2}\sum_{i \neq j} \frac{(\mathbf{m}_i \mathbf{m}_j)\mathbf{r}_{ij}^2 - 3(\mathbf{m}_i \mathbf{r}_{ij})(\mathbf{m}_j \mathbf{r}_{ij})}{\mathbf{r}_{ij}^5} \tag{II.5-1}$$

where $\mathbf{m}_i$and $\mathbf{m}_j$ are the magnetic moments of atoms (molecules) at the i^{th} and j^{th} sites of the lattice, while $\mathbf{r}_{ij}$ is the radius vector between them. The dipolar interaction decays much slower with distance than the exchange interaction and is non-local. By this it is meant that each magnetic moment in the system interacts with every other magnetic moment.

In the continuous approximation expression (II.5-1) reduces to a simpler form given by

$$W_d = -\frac{1}{2}\int_V dV \mathbf{M}\mathbf{H}_d \tag{II.5-2}$$

where $\mathbf{H}_d$ is known as the dipolar field. It can then be seen by inspection that the dipolar part of the free energy density of the ferromagnet is given by

$$w_d = -\tfrac{1}{2}\mathbf{M}\mathbf{H}_d, \tag{II.5-3}$$

The value of the dipolar field can be derived by solving the magnetostatic Maxwell equations with appropriate boundary conditions, as given by:

$$\mathrm{rot}\,\mathbf{H}_d = 0 \qquad \text{(II.5-4)}$$

$$\mathrm{div}(\mathbf{H}_d + 4\pi\mathbf{M}) = 0.$$

Thus, the dipolar field is frequently referred to as the magnetostatic field. The magnetostatic approximation is valid only if the group velocity of electromagnetic waves in the chosen medium is far greater than that of magnetic excitations (e.g magnons). If this is not the case then the full time-dependent Maxwell equations have to be solved in order to find the dipolar field. The solution of the system of equations (II.5-4) is given by:

$$\mathbf{H}_d = -\nabla\varphi(\mathbf{r}), \qquad \text{(II.5-5)}$$

$$\varphi(\mathbf{r}) = \int_V d\mathbf{r}'\mathbf{M}(\mathbf{r}')\frac{\partial}{\partial r_i}\left(\frac{1}{\mathbf{r}-\mathbf{r}'}\right)$$

where $\varphi(\mathbf{r})$ is the magnetostatic potential.

If the ferromagnet is magnetized uniformly (for instance, by a substantially large applied magnetic field) then expression (II.5-5) reduces to the form

$$\mathbf{H}_d = -4\pi N_{ij}(\mathbf{r})\mathbf{M}(\mathbf{r}), \qquad \text{(II.5-6)}$$

$$N_{ij}(\mathbf{r}) = \frac{1}{4\pi}\frac{\partial^2}{\partial \mathrm{r}_i \partial \mathrm{r}_j}\int_V \frac{d\mathbf{r}'}{|\mathbf{r}-\mathbf{r}'|},$$

where $N_{ij}(\mathbf{r})$ is the demagnetising tensor. In the system of coordinates where the axes are defined by the axes of symmetry of the sample under investigation, the demagnetising tensor can be diagonalised. The sum of the diagonal components (the trace) of the tensor is always equal to unity

$$\mathrm{Sp}\left(N_{ij}(\mathbf{r})\right) = 1 \qquad \text{(II.5-7)}$$

In the case of a perfectly spherical ferromagnet the diagonal components of the demagnetizing tensor are equal to each other: $N_{xx} = N_{yy} = N_{zz} = \frac{1}{3}$ Therefore the

demagnetizing field inside the sphere is uniform (while the field could be non-uniform outside).

According to the Eq. (II.5-6) the tensor of demagnetising coefficients $N_{ij}(\mathbf{r})$ depends only on shape of the system, and therefore magnetostatic interaction is mainly sensitive to the shape of the sample.

The equilibrium state of the unsaturated ferromagnet is defined by the interplay between the exchange and dipolar interactions. The minimum of the dipolar energy is only possible if the value of the dipolar field is reduced as follows from (II.5-2). To this end the ground state of the sample is subdivided into magnetic domains, so that the net magnetisation vanishes. An example of magnetic domains formed in a Ni_xFe_{1-x} (Permalloy) film is presented below in Figure II.5-1.

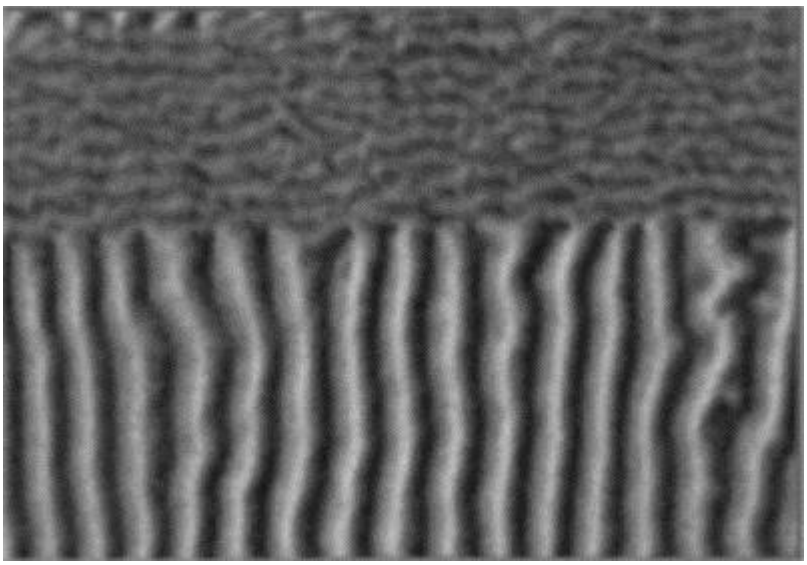

Figure II.5-1 Coexisiting weak and strong stripe domains in a sputtered 1800 nm thick Permalloy film with a small perpendicular anisotropy[48]

II.6 Magnetic anisotropy energy

It has been found that bulk magnetic materials can be relatively easily magnetized along certain directions (easy axis), while a greater external field is required

along other directions (hard axis)[39]. Typically the easy axis is related to the crystallographic axes of the sample and therefore the magneto-crystalline anisotropy. In magnetic thin films, the magneto-crystalline anisotropy is also derived from the broken symmetries of the crystal at the lateral edges of the sample or at interfaces with other materials.

In general the magneto-crystalline anisotropy is due to the spin-orbit interaction. In particular the full magnetic moment of the system (orbital moment plus spin) interacts via Coulomb interaction with the electrostatic field of the crystal lattice, created by ions which are external to the considered full magnetic moment. The problem of the evaluation of the magneto-crystalline anisotropy is complicated from the quantum mechanical standpoint. Nevertheless, phenomenologically magneto-crystalline anisotropy can be defined more easily. Assuming that the absolute value of the magnetization is a constant it is possible to express the magneto-crystalline anisotropy energy in the form of a power series in the magnetization. Only even powers of the magnetization are meaningful since the system should obide by symmetry constraints in time. Finally, the series should contain only those combinations of magnetization vectors that follow the crystallographic symmetry of the sample. For instance, for the simple case of uniaxial anisotropy the corresponding energy density can be written as

$$w_a = -K_2(\mathbf{Mn})^2 \qquad \text{(II.6-1)}$$

where K_2 and $\mathbf{n}$ define the strength and direction of the uniaxial magneto-crystalline anisotropy respectively. If $K_2 > 0$ then the energy of magneto-crystalline anisotropy is minimised when $\mathbf{M} \parallel \mathbf{n}$, and so vector $\mathbf{n}$ defines direction of easy magnetisation**.**

II.7 Zeeman energy

The Zeeman interaction is the interaction of the magnetic moments of atoms with an external magnetic field. The energy density of the Zeeman interaction is given by

$$w_Z = -\mathbf{H}_b \mathbf{M}(\mathbf{r}) \tag{II.7-1}$$

where $\mathbf{H}_b$ is the external field. There are no restrictions on the form of the applied field, (i.e. it could be a static field, a time-dependent field etc.). In micromagnetic simulations a time-dependent applied field is often used to excite magnetisation dynamics (Sections V-VIII).

II.8 Equation of motion of the magnetization

The phenomenological theory of magnetization dynamics and relaxation was developed by Landau and Lishitz[31]. They assumed that the absolute value of the magnetization is constant so that the dynamics of the magnetization are expected to have a processional form. By analogy with the classical equation of precession of a magnetic moment in an external field they derived an equation that includes contributions from all of the magnetic energies described above. This equation is called the Landau-Lifshitz equation and is given by

$$\frac{\partial \mathbf{M}}{\partial t} = -\gamma\left[\mathbf{M} \times \mathbf{H}_{eff}\right] + \mathbf{R} \tag{II.8-1}$$

where $\mathbf{H}_{eff}$ and $\mathbf{R}$ are the effective magnetic field and the relaxation term respectively. The Landau-Lifshitz equation keeps the length of the magnetization vector constant $\frac{\partial \mathbf{M}^2}{\partial t} = 0$ (which could be showed by multiplying both sides of (II.8-1) by $\mathbf{M}$); however different relaxation terms could alter it. A schematic representation of magnetization precession is shown in Figure II.8-1. According to the Landau-Lifshitz equation, the magnetization precesses about the direction of the internal effective field. The first term

of the Landau-Lifshitz equation represents the torque that causes the magnetic moment to precess, while the relaxation term causes the magnetization to move towards the equilibrium state.

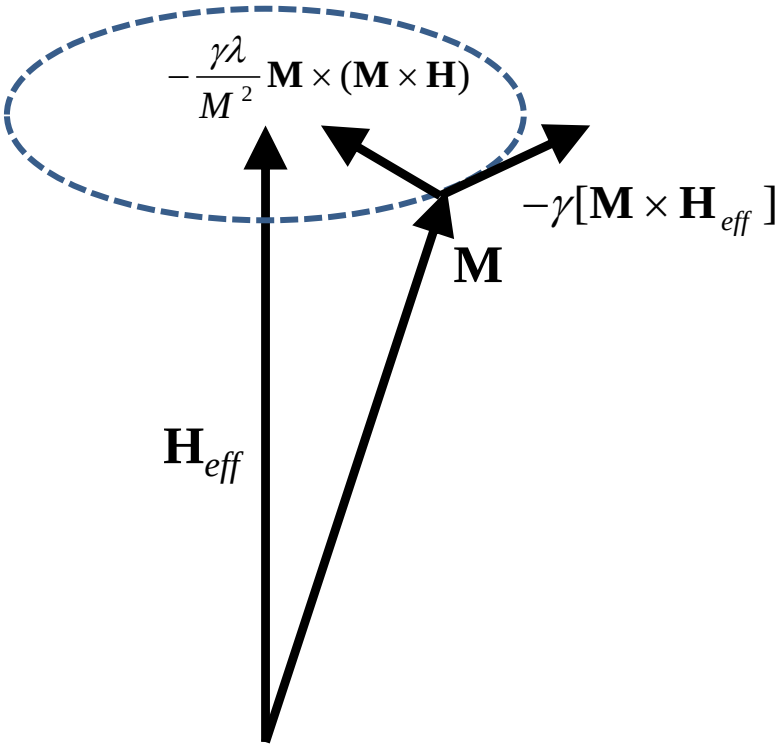

Figure II.8-1 Schematic representation of the magnetization precession around the direction of the internal effective magnetic field.

The metastable state of the system is given by:

$$[\mathbf{M}\times\mathbf{H}_{eff}]=0 \qquad \text{(II.8-2)}$$

Therefore in metastable the magnetization is parallel to the effective field as it was mention before. The equilibrium state of the magnetisation requires internal field becomes zero $\mathbf{H}_{eff}=0$.

The value of the effective field is derived from the free energy density of the magnetic medium

$$\mathbf{H}_{eff}=-\frac{\delta w}{\delta \mathbf{M}} \qquad \text{(II.8-3)}$$

The free energy density includes contributions from all magnetic energies present in the magnetic system.

In general, the relaxation term is given by

$$\mathbf{R} = \hat{\lambda}_1 \mathbf{H}_{eff} - (\nabla \hat{\lambda}_2 \nabla)\mathbf{H}_{eff} \tag{II.8-4}$$

where $\hat{\lambda}_1$ and $\hat{\lambda}_2$ are the relaxation tensors[49] of rank 3. The relaxation term given by expression (II.8-4) includes relaxation processes that do not preserve the absolute value of the magnetization. An equation of motion that also does not preserve the length of the magnetization vector was proposed by Bloch[50]. The modified Bloch equation is given by

$$\frac{\partial \mathbf{M}}{\partial t} = -\gamma\left[\mathbf{M} \times \mathbf{H}_{eff}\right] + \omega_\Gamma(\mathbf{M} - \frac{M_0}{H_0}\mathbf{H}_{eff}) \tag{II.8-5}$$

where ω_Γ is the relaxation frequency, while M_0 and H_0 are the initial value of the magnetization of saturation and the absolute value of applied field, respectively.

However, if the relaxation preserves the length of the magnetization vector, then the relaxation term could be represented by one of the following forms

$$\mathbf{R} = -\frac{\gamma\lambda}{M_s^2}\left[\mathbf{M} \times \left[\mathbf{M} \times \mathbf{H}_{eff}\right]\right] \tag{II.8-6}$$

$$\mathbf{R} = -\frac{\alpha}{|M_s|}[\mathbf{M} \times \frac{\partial \mathbf{M}}{\partial t}]$$

The first and second forms of the expression for the relaxation term shown in (II.8-6) were proposed by Landau-Lifshitz, and Gilbert respectively. λ is the Landau-Lifshitz dissipation constant, while α is the Gilbert damping constant. If the Landau-Lifshitz equation is used with the Gilbert damping term, then it is called the Landau-Lifshitz-Gilbert (LLG) equation. All numerical studies presented in this manuscript have been performed using the LLG equation. In the limit of small angle precession (linear

approximation), all three forms of the dissipative term given by expressions (II.8-5) and (II.8-6) are equivalent.

Typically garnets are characterized by small magnetic losses around 10^{-5}. Metals show much larger damping of around 10^{-2} due to interactions between magnons and free electrons.

Spatially non-uniform dynamical solutions to the Landau-Lifshitz equation are called spin waves (SW).

II.9 Uniform magnetization precession

Despite the fact that solutions of the Landau-Lifshitz equation can be non-uniform in space, the spatially uniform solutions are of particular interest because they could be both easily measured[51] and derived analytically.

Uniform precession is characterized by the in-phase motion of magnetic moments within a magnetic system. Thus it is not possible to distinguish a particular magnetic moment from the rest. From this point of view it is possible to reduce the Landau-Lifshitz equation to the case of only one magnetic moment precessing in an internal field. Such an approximation is a widely used analytical approach and is called the *macrospin approximation*.

The frequency of uniform precession can be directly derived from the LLG equation. For the isotropic ferromagnetic ellipsoid magnetized along one of its symmetry axes (e.g. z-axis) by a applied field H_b, the frequency of uniform precession in the ellipsoid is given by

$$\omega_u = \gamma\sqrt{(H_b + (N_{xx} - N_{zz})M_s)(H_b + (N_{yy} - N_{zz})M_s)} \qquad \text{(II.9-1)}$$

The above expression (II.9-1) was derived by Kittel[52], and is known as the Kittel formula. In experimental studies uniform precession is referred to as uniform ferromagnetic resonance.

For the case of a ferromagnet of a spherical shape, the Kittel formula (II.9-1) reduces to

$$\omega_u = \gamma H_b \tag{II.9-2}$$

Therefore for a spherical sample the frequency of uniform precession does not depend on its magnetisation.

For a magnetic thin film magnetized in-plane, only one component of the demagnetisation tensor has a non-zero value[24]. Therefore the frequency of uniform precession is given by

$$\omega_u = \gamma\sqrt{H_b(H_b + 4\pi M_s)} \tag{II.9-3}$$

Thus for magnetic thin films the frequency of uniform precession depends upon the value of the saturation magnetisation M_s. This property is widely used in experiments to determine the value of the magnetization of saturation of the sample by measuring the frequency of uniform precession.

Finally the frequency of the ferromagnetic resonance does not depend on the exchange stiffness, since all magnetic moments of the system are oriented along the same (precessing) direction. Thus the energy of the exchange interaction remains of zero value.

II.10 Non-uniform precession of the magnetisation. Magnetostatic waves

In the general case solutions of the LLG equation are spatially non-uniform. Thus the macrospin approximation could not be applied and the LLG equation has to be

solved in both the spatial and temporal domains. As the magnetization becomes non-uniform the dynamic dipolar field cannot be described in terms of the demagnetizing tensor, and so Maxwell equations have to be solved with appropriate boundary conditions to find magnetic dipolar field. In addition if the spatial profiles of the magnetization are non-uniform then the exchange interaction is expected to contribute to the magnetisation dynamics.

In the limiting case of spin waves with wavelength much longer than the exchange length the contribution of the exchange interaction becomes negligible compared to that of the dipolar interaction. If in addition the spin wave vector of, *k*, is much greater than that of light

$$k \gg \frac{\omega}{c} \tag{II.10-1}$$

then it is possible to neglect the dynamical part of the Maxwell equations so that the dipolar field can be described by the magnetostatic Maxwell equations alone. The corresponding solutions of Landau-Lifshitz equation are known as magnetostatic waves.

The dispersion of magnetostatic waves can be derived from the generalised Walker equation[53]

$$\text{div}\,(\hat{\mu}\nabla\varphi) = 0 \tag{II.10-2}$$

where $\hat{\mu}$ is the high frequency permeability tensor that describes the temporal dispersion of spin waves and is derived from the solution of the LLG equation. The solution of equation (II.10-2) must satisfy the following boundary conditions[24]

$$\frac{\partial\varphi_1}{\partial\boldsymbol{\tau}} = \frac{\partial\varphi_2}{\partial\boldsymbol{\tau}} \tag{II.10-3}$$

$$\hat{\mu}_1\nabla_{\mathbf{n}}\varphi_1 = \hat{\mu}_2\nabla_{\mathbf{n}}\varphi_2$$

where $\boldsymbol{\tau}$ and $\mathbf{n}$ denote tangent and normal vectors of the boundary.

The exact form of the magnetostatic potential given by the solution of equation (II.10-2) is divided into two classes of magnetostatic waves. If the magnetostatic potential is localized in the entire volume of the sample then the spin waves are called volume magnetostatic waves. In contrast, if the magnetostatic potential is only significant near the lateral surfaces of the sample, then the corresponding spin waves are called surface waves.

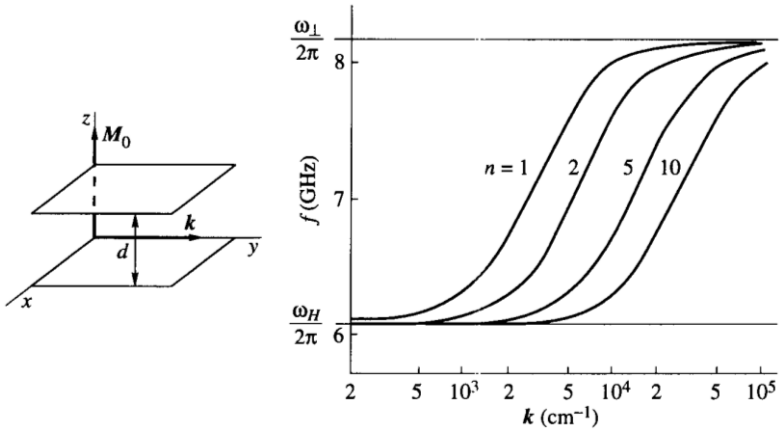

Figure II.10-1 Schematic representation of forward-volume magnetostatic spin waves geometry is shown together with their dispersion for the case of a normally magnetized thin magnetic YIG film (the illustration is taken from Ref. 24).

In the general case of magnetostatic waves equation (II.10-3) is not easily solved. Nevertheless it is possible to derive analytical solutions in some limiting cases so that the properties of the corresponding spin waves can be investigated.

Let us consider the case of an infinite isotropic magnetic thin film magnetized normal to the plane. We will also consider spin waves of with small wavevectors, and so the exchange interaction could be neglected. For spin waves propagating in the plane of the film (Figure II.10-1), the magnetostatic potential has the following form[24]:

$$\varphi(\mathbf{r}) = (\mathrm{A}\sin k_z z + B\cos k_z z)\, e^{-ik_y y} \qquad \text{(II.10-4)}$$

where A and B are some constants defined by the boundary conditions (II.10-3). Hence the potential has a volume form and so here we have a case of volume magnetostatic waves whose dispersion is given by[24]

$$\omega_{FVMSSW} = \gamma \sqrt{H_b \left(H_b + \frac{4\pi M_s}{1 + \frac{n^2\pi^2}{k^2 d^2}} \right)} \tag{II.10-5}$$

where $n > 1$ denotes the order of the standing modes in the confined direction and d is the thickness of the film. The dispersion of the volume magnetostatic waves considered above is positive so that the signs of the group and phase velocities are the same. Thus, the energy of the wave propagates along with its wavefront. Such waves are called Forward-Volume Magnetostatic Spin Waves (FVMSSW).

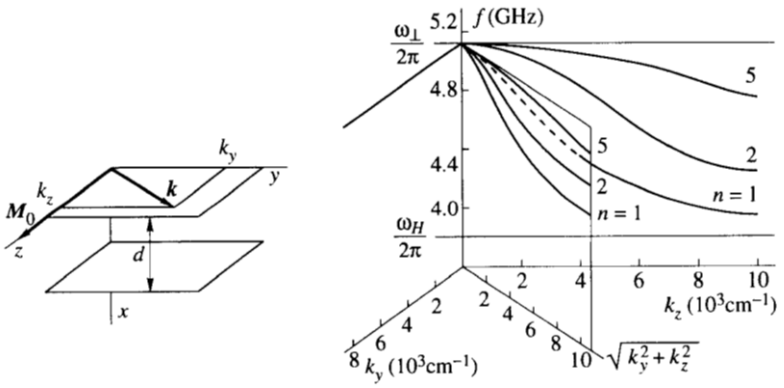

Figure II.10-2 Schematic representation of the backward volume magnetostatic spin waves geometry is shown together with their dispersion for the case of the tangentially magnetized thin magnetic film of YIG (the illustration is taken from Ref. 24).

If the film is magnetized tangentially (Figure II.10-2), the magnetostatic potential has a volume form given by[24]

$$\varphi(\mathbf{r}) = (\mathrm{A}\sin k_x x + B\cos k_x x)\, e^{-ik_y y - ik_z z}. \tag{II.10-6}$$

The dispersion of such waves is then given by [24]

$$\omega_{BVMSSW} = \gamma \sqrt{H_b \left(H_b + \frac{4\pi M_s}{1 + \frac{\cos^2\theta}{\sin^2\theta + \frac{n^2\pi^2}{k^2 d^2}}} \right)} \qquad \text{(II.10-7)}$$

where θ denotes the angle between the equilibrium magnetisation and the wave vector of the propagating volume magnetostatic wave. The dispersion of such waves is negative and so energy and phase travel in opposite directions. As a result such waves are called Backward Volume Magnetostatic Spin Waves (BVMSSW).

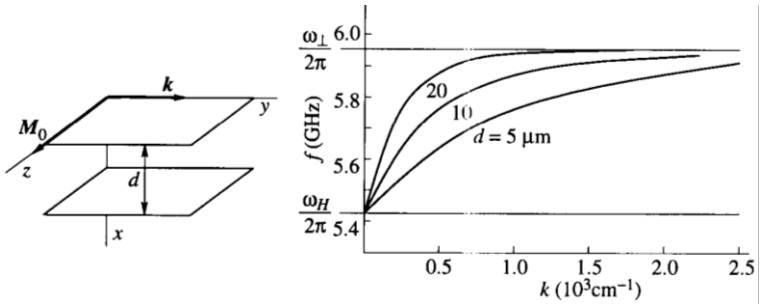

Figure II.10-3 Schematic representation of the Damon-Eshbach magnetostatic waves geometry is shown together with their dispersion relation for the case of a YIG thin film magnetised tangential to the plane. The wave vector of the propagating spin waves is perpendicular to the equilibrium magnetization (the illustration is taken from Ref. 24).

The form of the dispersion of BVMSSW depends monotonically on the angle between their wave vector and the static magnetisation (Figure II.10-2). In the limiting case of the wave vector perpendicular to the static magnetization (Figure II.10-3), the form of the magnetostatic potential becomes[24]

$$\varphi(\mathbf{r}) = (\mathrm{A}\, \mathrm{e}^{-k_x x} + B\, \mathrm{e}^{-k_x x - kd}) e^{-ik_y y} \qquad \text{(II.10-8)}$$

The potential has a surface form and so the magnetostatic waves have surface character. Their dispersion is given by[24]

$$\omega_{\mathrm{DE}} = \gamma \sqrt{\left(H_b + \frac{4\pi M_s}{2}\right)^2 - \left(\frac{4\pi M_s}{2}\right)^2 \mathrm{e}^{-2kd}} \qquad \text{(II.10-9)}$$

The group velocity of the surface spin waves is positive as in case of FVMSSW. The expression for the dispersion of the surface magnetostatic waves (II.10-9) was obtained by Damon and Eshbach[54], therefore surface magnetostatic waves are often called Damon-Eshbach magnetostatic waves.

Despite the fact that an analytical expression for the dispersion of magnetostatic spin waves can be easily derived for the geometries considered it is not possible to derive such an expression for more complicated systems, such as unsaturated samples of finite dimension.

II.11 Conclusions

Ferromagnetic systems are characterized by a wide range of magnetic interactions of different origins and the magnetisation dynamics in such systems has a complex character. In addition the Landau-Lifshitz equation is non-linear adding a further complication. Magnetization dynamics in realistic samples is not readily described analytically in the most cases. Therefore for some cases it is only possible to solve the Landau-Lifshitz equation numerically. In particular this applies to the problems of magnonics - an emerging area of magnetism that focuses on the investigation of spin waves on the nanoscale[32].

III Object Oriented Micromagnetic Framework

III.1 Introduction

The Object Oriented Micromagnetic Framework (OOMMF) is an open-source software package[55] that generates numerical solutions of the Landau-Lifshitz-Gilbert (LLG) equation in the time and spatial domains. OOMMF utilizes the well-established Finite Difference Time Domain (FDTD) method to solve the LLG equation. The principal idea of this method is to replace the continuous volume of the sample with a discrete mesh of rectangular cells (with uniform magnetic moment), and so the LLG equation can be solved for each individual cell separately. The differential operators underlying the LLG equation are replaced by the corresponding finite difference operators[56]. The spatial discretization is fixed by the user while the temporal discretization is estimated dynamically by the OOMMF solver.

The rectangular discretization used in OOMMF can lead to artefacts due to the "step-like" sampling of the surfaces of the sample. Such sampling artefacts could potentially distort the results of simulations. Nonetheless real world nanoscale samples also have rough surfaces and so the spatial discretization can in principle be used to recreate edge and surface roughness which are common features of devices fabricated on the nanoscale.

OOMMF calculates both the effective field and the solution of the LLG equation. It supports calculation of various magnetic energies, including the Zeeman, magnetostatic, exchange, two-fold and four-fold magnetic anisotropies energies.

As compared to analytical theories, OOMMF does not make any particular assumptions on the dynamics of magnetic moments (such as the approximation of small angle precession) or assumptions related to the calculations of the magnetic energies. Therefore in many cases results obtained using OOMMF can be more general than those obtained from analytical theories. This is why OOMMF has become widely used to analyse experimental data for cases where analytical theories cannot be developed. By varying the numerical model one aims to reveal the origin of the effects observed in the experiment.

In principle OOMMF and other micromagnetic packages could be used to evaluate the limitations of analytical theories, as will be shown in Section V**.** If results obtained with micromagnetic simulations and analytical theories are different, micromagnetic packages could then be used to estimate the origin of the difference, depicting additional terms which should be taken into account in the analytical theory as discussed in Section V.

Finally, micromagnetic simulations can be used to predict new effects even in cases where experimental and, or, analytical approaches could not be as easily applied. An example of such predictions is provided in Section VII.

However, any numerical simulations are limited by the available computational resources. This means that samples with micrometre dimensions could not be simulated using fine meshes. For some applications one can use larger cell sizes to simulate even micrometre sized samples. Using of the large cells (as compared to exchange length which defines the range of exchange interaction) gives rise to error in the numerical

calculation of the exchange energy. Therefore if large cells are used the results of the micromagnetic simulations should be always validated by performing simulations with different cell dimensions so as to estimate the effect of their size upon the results. If the difference is acceptable in terms of the studied model then one can proceed with the simulations that utilise large cells.

From other end, one cannot refine the mesh used in the simulation beyond limits of the continuous approximation[46] underling the LLG equation. Therefore OOMMF cannot be used to solve problems where the continuous approximation is not valid, e.g. for cells having dimensions comparable to the lattice constant.

III.2 A History of Object Oriented Micromagnetic Framework

OOMMF has been developed by Mike Donahue and Don Porter at the Applied and Computational Mathematics Division (ACMD) of the National Institute of Standards and Technologies (NIST) in close cooperation with the Micromagnetic Modelling Activity Group (μMAG). The first public demo was released at the Joint MMM-Intermag conference (San Francisco, January 6-9, 1998). At that point, evaluation of the 3D spins on 2D meshes was the main goal of the software. After the first public demonstration OOMMF became more widely used within the magnetic community. Since then micromagnetic problems attempted have become more complicated, requiring a more flexible 3D solver to be developed.

The first public release of OOMMF with a 3D solver was made at the OOMMF Workshop 2000, held at NIST/Gaithersburg MD on 18-August-2000. Along with the ability to simulate 3D meshes the new solver provided more flexibility in terms of specifying the model to be used in the simulations. In particular any magnetic parameters of the system (such as the magnetisation of saturation, the exchange stiffness

etc.) could be defined point-wise. For this purpose OOMMF began to provide a powerful scripting engine. Additionally, a new Application Programming Interface (API) was presented to third-party developers who could extend the 3D solver already built in to OOMMF so as to support new energy terms or equations of motion of magnetisation. Currently there are a growing number of extensions developed for OOMMF's 3D solver[57]. The list includes; spin-transfer torque, thermal energy and other effects.

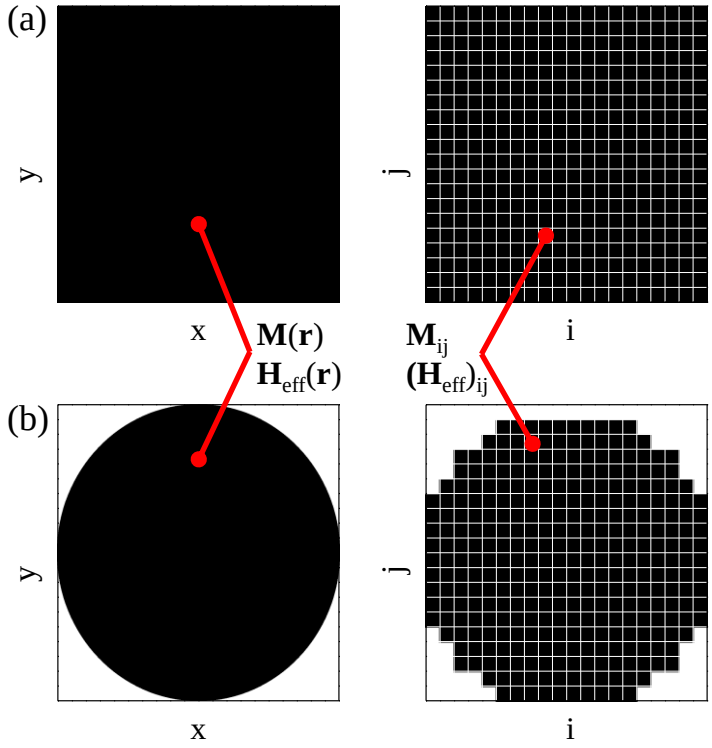

Figure III.2-1 The schematic images of the spatial discretization into regular rectangular cells are shown for rectangular (a) and circular (b) geometries.

The growing demands of 3D simulations pushed OOMMF developers to adapt their software for multicore environments so that the software could utilize the full power of modern computers. This modification significantly decreases the time required

for large scale simulations which is of great benefit to any study. Currently there is no public release of the parallelized version of OOMMF. Nonetheless developer builds are available on-demand from Mike Donahue[58]. The set tests provided in[59] show an almost linear relationship between the OOMMF performance and the number of CPU cores available in the system. This means that simulations performed on a four-core computer are four times faster than those performed on a single-core system. As the number of CPU cores increases rapidly from year to year OOMMF becomes ever more powerful opening new opportunities for micromagnetic simulations.

III.3 Finite Difference Method

The 3D micromagnetic solver in OOMMF is based on the FDTD scheme. This means that differential operators in the LLG equation are replaced with corresponding finite difference operators so that the LLG equation can be integrated by use of one of several well-known numerical schemes (such as the Euler or Runge-Kutta schemes). More specifically a Finite Difference (FD) method means that the volume of the problem is discretised into rectangular cells. The magnetization is assumed to be uniform within each cell. An example of such a discretization is presented in Figure III.2-1. OOMMF utilizes the so-called central difference scheme; in which spins are located in the centre of the rectangular cells of the mesh. The coordinates $\mathbf{r}_{ijk}$ of each given spin on the mesh are given by, $\mathbf{r}_{ijk} = (\frac{\Delta x}{2} + i\Delta x, \frac{\Delta y}{2} + j\Delta y, \frac{\Delta z}{2} + k\Delta z)$, where Δx, Δy and Δz denote the dimensions of the discrete cells. By estimating the difference between the volumes of the continuous and discretised samples we can quantify the significance of artefacts due to the process of discretisation as given by

$$\Delta \mathrm{V} = \int_{V} f(\mathbf{r}) d^3\mathbf{r} - \sum_{i \in V} \sum_{j \in V} \sum_{k \in V} x_i x_j x_k \tag{III.3-1}$$

where $f(\mathbf{r})$ defines the volume of the sample. If the $|\Delta V/V| << 1$ then the effect of the induced artefacts will be negligible.

Figure III.2-1(a) shows that the discretization of rectangular geometries does not lead to artefacts. In particular, the volume and shape of the discretised sample are preserved so that $|\boldsymbol{\Delta V/V}| = \mathbf{0}$. Meanwhile for the elliptical geometry (Figure III.2-1(b)), the volume is not preserved, $|\boldsymbol{\Delta V/V}| > \mathbf{0}$, and so artefacts are introduced due to the discretisation. Nevertheless by decreasing the cell dimensions we can make the difference in the two volumes approach the limit $|\boldsymbol{\Delta V/V}| \to \mathbf{0}$ where the artefacts would be negligible. However, as discussed above, one cannot reduce the dimensions of the cell below the natural physical limits, e.g. below the lattice constant. In particular the lattice constant of Permalloy (*Py*) is 0.3 nm, which defines the lower limit of the mesh refinement. Moreover as the cell size decreases the required computational power increases, making the duration of the simulations considerably longer. OOMMF does not have dedicated algorithms to control the spatial discretization so it must be controlled by the user.

Assuming that the sample is discretized, the LLG equation takes the form

$$\frac{\partial \mathbf{M}_{ijk}}{\partial t} = -\gamma_{ijk}\left[\mathbf{M}_{ijk} \times \mathbf{H}_{ijk}^{eff}\right] + \frac{\alpha_{ijk}}{M_{ijk}^{s}}\left[\mathbf{M}_{ijk} \times \frac{\partial \mathbf{M}_{ijk}}{\partial t}\right] \tag{III.3-2}$$

where $\mathbf{M}_{ijk}$, $\mathbf{H}_{ijk}^{eff}$, γ_{ijk}, α_{ijk} and M_{ijk}^{s} denote the values of the magnetisation, the internal field, the gyromagnetic ratio, the Gilbert damping constant and the saturation magnetisation respectively, at the site in the mesh with the i, j and k indices. The LLG equation can now be rewritten as

$$\frac{\partial \mathbf{M}_{ijk}}{\partial t} = f(t, \mathbf{M}_{ijk}) \tag{III.3-3}$$

where $f(t, \mathbf{M}_{ijk})$ is an as yet unspecified function that depends on time and the dynamic magnetisation.

To integrate the discrete LLG equation in the time domain the first order time derivatives of the magnetisation $\frac{\partial \mathbf{M}_{ijk}}{\partial t}$ are replaced by the corresponding finite difference operators. Thus the time domain becomes discretised and each particular point of time, t_n, is given by: $t_n = t_0 + n\Delta t_n$, where Δt_n is set of time steps chosen by the solver during the integration. For the classical Runge-Kutta method[60] (which is among the integration methods of the 3D solver of the OOMMF) the value of the magnetization, $\mathbf{M}_{ijk}(t_{n+1})$ at the $n+1$ time step is given by

$$\begin{aligned}
\mathbf{M}_{ijk}(t_{n+1}) &= \mathbf{M}_{ijk}(t_n) + \frac{1}{6}(k_1 + 2k_2 + 2k_3 + k4) \\
k_1 &= f\left(t_n, \mathbf{M}_{ijk}(t_n)\right)\Delta t \\
k_2 &= f\left(t_n + \frac{1}{2}\Delta t, \mathbf{M}_{ijk}(t_n) + \frac{1}{2}k_1\right)\Delta t \\
\mathrm{k}_3 &= f\left(t_n + \frac{1}{2}\Delta t, \mathbf{M}_{ijk}(t_n) + \frac{1}{2}k_2\right)\Delta t \\
k_4 &= f(t_n + \Delta t, \mathbf{M}_{ijk}(t_n) + k_3)\Delta t
\end{aligned} \tag{III.3-4}$$

Then the error of numerical calculation is estimated. If for every cell in the mesh the error is smaller than some predefined value the time step becomes successful and the solver proceeds to the next time step. If the error is larger than the predefined value then the time step is reduced and the entire calculation is repeated. One step of the *rk4* method involves 11 evaluations of $\frac{\partial \mathbf{M}_{ijk}}{\partial t}$. The *rk4* is the fourth-order method and so

the absolute value of the error per step and its accumulation are of the order Δt^5 and Δt^4 , respectively.

III.4 Exchange energy

The local character of the exchange energy was discussed in Section II.4. This means that for each particular point of space the exchange energy is calculated in the vicinity of that point and no other points of the sample contribute to the exchange energy of the cell.

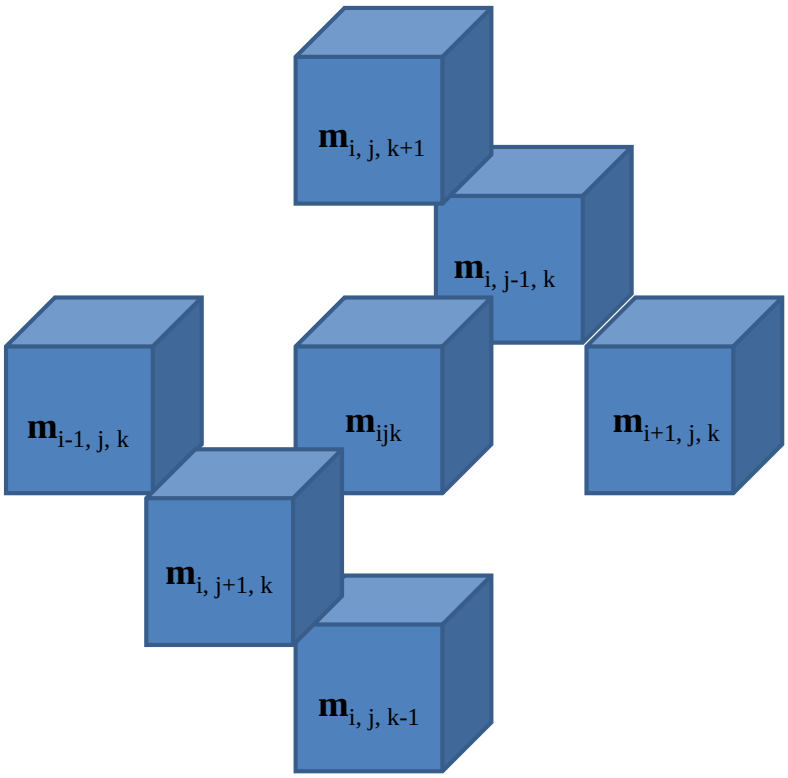

Figure III.4-1 The schematic representation of the spatial kernel that is used in the calculation of the exchange energy.

The Laplace operator in the expression of the exchange energy (II.4-3) is replaced with its finite difference equivalent. Thus for a given cell with indices i, j and k, the discretized form of the expression of the exchange energy could be represented as

a convolution of the exchange stiffness tensor A_{mnl} with the combination of the magnetic moments of the neighbouring cells.

In OOMMF, the exchange energy is calculated by means of the six-neighbour scheme. The schematic image of the convolution kernel is shown in Figure III.4-1. For a given cell with indices *i*, *j* and *k* the exchange energy is given by

$$E_{ijk}^{exch} = \sum_{m,n,l \in dV} A_{ijk,mnl} \frac{\mathbf{m}_{ijk}(\mathbf{m}_{ijk} - \mathbf{m}_{mnl})}{\left(\mathbf{r}_{ijk} - \mathbf{r}_{mnl}\right)^2} \tag{III.4-1}$$

where dV represents the volume that contains those six neighbouring cells, and $\mathbf{m}_{ijk}$ and $\mathbf{m}_{mnl}$ represent reduced magnetizations $\frac{\mathbf{M}_{ijk}}{M_s}$ and $\frac{\mathbf{M}_{mnl}}{M_s}$ respectively. In the case of quasi-2D meshes the six-neighbour scheme reduces to the four-neighbour scheme.

The six-neighbour scheme does not include the diagonal elements in the vicinity of the given cell and so only the cells on the major axes contribute to the exchange energy. Thus, if two magnetic materials are connected together, but the connected cells are laying on the diagonals of the mesh for the given cell, these materials will not interact through the exchange coupling.

The exchange stiffness tensor could be represented in terms of exchange length as

$$A_{ijk,mnl} = \frac{\mu_0 M_s^2 l_{ijk,mnl}^2}{2} \tag{III.4-2}$$

where l_{ijk}^2 is the exchange length of the magnetic moments with indices i, j, k and m, n, l. By substituting (III.4-2) into (III.4-1), we obtain

$$E_{ijk}^{exch} = \sum_{m,n,l \in dV} \frac{\mu_0 M_s^2 l_{ijk,mnl}^2}{2} \frac{\mathbf{m}_{ijk}(\mathbf{m}_{ijk} - \mathbf{m}_{mnl})}{\left(\mathbf{r}_{ijk} - \mathbf{r}_{mnl}\right)^2} \quad \text{(III.4-3)}$$

The exchange length defines the range of the exchange interaction in the material. Therefore only the magnetic moments that lie at the sphere whose radius is that of exchange length are can interact with one another via the exchange interaction. However expression (III.4-3) could be used to estimate the energy of the exchange interaction if the distance between the spins is larger than the exchange length. In this case the value of the exchange interaction will be reduced relative to the case where the distance between moments is less than the exchange length. If the exchange interaction is of particular interest for simulations and, or, plays a significant role in the observed effects then in order to calculate its energy correctly one should use a mesh formed by cells with dimensions such that $\left|\mathbf{r}_{ijk} - \mathbf{r}_{mnl}\right| < l_{ijk,mnl}$. In particular the value of the exchange length in *Py* is approximately *5nm*. Therefore each dimension of the rectangular cells forming the mesh of the sample should be smaller than *5nm*. Nevertheless if for some reason certain dimensions of the mesh are expected to have a reduced impact of the exchange energy then the cell size could be increased above the value of the magnetostatic-exchange length for those directions as described in Sections V-VII.

III.5 Magnetostatic field

The magnetostatic interaction described in Section II.5 has a non-local character. Therefore for each particular point in space the value of the magnetostatic field is a superposition of those magnetostatic fields created by all other points within the volume of the sample. If the sample is discretized then the calculation of the magnetostatic field within a given cell requires the summation of the magnetostatic

contributions from every cell of the mesh. Such a straightforward approach requires significant computational resources and is therefore impractical in most cases.

To calculate the value of the magnetostatic field the 3D solver in OOMMF utilizes the convolution theorem[61]. If the magnetostatic interaction has a non-local character in real space it becomes local in reciprocal space. If we assume that the magnetization is uniform within each cell then the demagnetizing tensor of the cell, N_{ijk} can be calculated with high accuracy using the expression developed in Refs. 62,63. If the mesh is discretised in the regular way so that the cell size is constant across the mesh then the demagnetizing tensor needs to be calculated only once i.e. $N_{ijk} = N$. Therefore in the discretised reciprocal space the value of the demagnetizing field at the cell with indices i, j and k is given by:

$$\widetilde{\mathbf{H}}_{ijk}^{demag} = -4\pi M_s(\widetilde{N} \cdot \widetilde{\mathbf{m}}_{ijk}) \tag{III.5-1}$$

where "~" denotes the Fourier image of the given variable. The value of the demagnetizing field in real space is calculated by taking an inverse Fourier transform of equation (II.5-1)

$$\mathbf{H}_{ijk}^{demag} = -4\pi M_s FFT^{-1}(\widetilde{N} \cdot \widetilde{\mathbf{m}}_{ijk}), \tag{III.5-2}$$

Where FFT^{-1} denotes backward FFT.

The Fourier image of the demagnetizing tensor is calculated only once when the simulation is initialised. Thus the calculation of the demagnetizing field requires one forward and one backward Fast Fourier transformation in 3D. This method has great computational advantages over the straightforward calculation detailed earlier and is also used in other micromagnetic packages[157].

III.6 Magnetic anisotropy

The anisotropy has a local character and so its energy depends on the magnetic moment of a particular point in the sample. When the volume of the sample is discretised the expression for the energy of the uniaxial anisotropy (II.6-1) becomes

$$E_{ijk}^{uniax} = K_{1_{ijk}} \mathbf{m}_{ijk} (\mathbf{m}_{ijk} \mathbf{n}_{ijk}), \tag{III.6-1}$$

where $K_{1_{ijk}}$ and $\mathbf{n}_{ijk}$ denote the cell-wise values of the uniaxial anisotropy constant and the directions of the anisotropy axis respectively.

III.7 Other energy terms

As soon as a version of OOMMF containing a 3D LLG solver was released the comprehensive API become open to third-party developers. Therefore, the out-of-the-box functionality of OOMMF could be extended by means of additional extensions written for particular purposes. Several such extensions have become publically available since the initial release of the 3D solver in OOMMF. A complete list of the extensions can be found in Ref. 57. Here is a partial list of the extensions:

a) Modelling of the finite temperature via a field term of the Langevin type[64].

b) One-dimensional periodic boundary conditions[65].

c) Uniaxial anisotropy with a fourth order term[66].

d) Cubic anisotropy with sixth and eighth order terms[67].

e) Spin-torque terms describing current-induced domain wall motion[68].

f) Two-dimensional periodic boundary conditions[69].

In addition the 3D solver in OOMMF provides an extension for calculating the spin-transfer torque by means of the Slonczewski term[70]. Therefore one can conclude

that OOMMF covers the major aspects of magnetization dynamics described by the LLG equation.

III.8 Multi-Threaded Micromagnetic framework

When the parallelized version of the 3D solver in OOMMF was not available I modified the serial version of OOMMF to gain performance improvements in multi-core computing environments. The project acquired the name of Multi-Threaded Micromagnetic Framework (MTMF). The main purpose of this project was the calculation of magnetization dynamics in 2D arrays of rectangular elements, with the number of elements higher than in the recent studies[89], (typically, *3x3* or *5x5*). The serial version of OOMMF did not provide sufficient computational power to simulate such arrays on practical timescales. I therefore utilised the OpenMP framework to partially parallelize the serial code of OOMMF. In particular, calculation of the exchange and magnetostatic energies and the Runge-Kutta solver were thoroughly parallelized. In addition the FFT and vector operations within the core of the 3D solver in OOMMF were rewritten in terms of SSE instructions[71], rather than the pure C++ code.

Measurements performed on a test sample containing $\sim 1.5 \cdot 10^5$ cells showed a performance improvement of around ~2.8 when running on four computational cores. Thus our group acquired a powerful tool before the public availability of the parallelized version of OOMMF. This allowed us to simulate the magnetization dynamics of arrays of rectangular elements containing more elements than all previous studies. The majority of the data presented in Section VI was calculated using this MTMF software.

However the OpenMP parallelization has some weak points limiting the performance enhancement that one can ultimately achieve with this method. In particular, in a system with several CPUs each processor has its own local memory and the software should take this into account since access to the non-local memory generates performance penalties and thereby reducing overall computational performance. The scenarios of such memory access patterns are called Non-Uniform Memory Access (NUMA)[72] and are supported by the majority of the available operating systems. However the developer should manually take care of the memory access patterns in the software in order to achieve maximum performance. The OpenMP framework does not support NUMA explicitly, and so, the MTMF software does not scale as well on systems with several physical CPUs.

III.9 OOMMF as compared to the other micromagnetic packages

OOMMF has been extensively used by the magnetic community and has proven its capability in describing experimental results and giving insight into the physical phenomena underlying the experimental observations. Nevertheless there are other micromagnetic solvers available. A list of the major packages is given in Table III.9-1.

Package name	Type of license	PBC	Spin transfer-torque support	Method of calculation	Multicore support	Supported platforms
OOMMF	Freeware	2D	Yes	FDTD	Yes	Win32 UNIX Linux
NMag	Freeware	3D	Yes	Finite Elements	Yes	UNIX Linux
MagPar	Freeware	No	Yes	Finite Elements	Yes	Win32 UNIX Linux
LLG	Commercial	2D	Yes	FDTD	No	Win32
MicroMagus	Commercial	2D	Yes	FDTD	Yes	Win32

Table III.9-1 A comparison chart of the available micormagnetic solvers.

The table shows that OOMMF is among the most flexible packages available. It provides support for virtually any computational platform on the basis of a free software licence. The memory requirements of the Finite Elements Method (FEM) are an order of magnitude greater than those of the FDTD method. Therefore calculations of large samples require amounts of memory that are not always available for regular users without access to computational clusters or supercomputers.

Commercial packages (such as LLG and MicroMagus) have very limited features and suffer from relatively poor performance on multicore machines. In addition the algorithms of the calculations used in the commercial software are “closed” providing the user with little insight into the methods by which the calculation carried out. However they do provide a graphical interface to the user together with data

analysis functions which sometimes considered being more important than other features.

III.10 Conclusions

Here I have described how OOMMF, which is used for the studies described in this thesis, is a very versatile tool for micromagnetic studies. It provides a comprehensive set of features together with support for state-of-the-art computational techniques. The algorithms for the calculations used in OOMMF have been widely adopted and validated within the other fields of physics. There is also a number of studies available suggesting that OOMMF provides the most adequate solutions of the LLG equation as compared to the other micromagnetic packages[73].

The functionality of OOMMF can be expanded by means of additional extensions. The development of OOMMF is still on-going and the development of such extensions is supported by the OOMMF core developers upon request.

IV Semargl: A Tool for Advanced Processing of Real Space Sampled Data

IV.1 Introduction

OOMMF and other numerical micromagnetic packages solve the LLG equation in real space and the time domain. In order to gain an insight into the magnetic processes underlying the simulations one has to analyse the data thoroughly. However the currently available micromagnetic packages do not provide tools for in depth data analysis and so only simple data manipulations can be done (such as the spatial averaging of the data). Any extensive data processing requires third-party tools to be developed and implemented.

There are many possibilities in terms of data analysis. One way is to use commercially available software (such as Origin[74]). The main disadvantage of this method is that commercial software is made to be simple and user-friendly and so the performance of software is reduced at the expense of the user experience. For instance such packages keep several instances of the data in order to perform so-called "undo" operations. Therefore large amounts of data cannot be analysed because of the limited size of the computer memory. Moreover commercial software is usually designed to be

compatible with several recent and legacy computational platforms. Thus most recent computational technologies are usually not supported by professional third-party software. So, the performance of the commercial software is usually far below the possibilities of the recent computational platforms and architectures meaning that only results from small simulations (in terms of the number of cells in the mesh) can be analysed on practical timescales.

Another approach is to use high-level programming languages (e.g. MatLab[75]) in order to develop custom software for the data analysis. Nevertheless in the fault-tolerant environments (such as MatLab) some assumptions are made on the memory layout and computational technologies in order to prevent software from crashes and, or, security vulnerabilities. Therefore in high-level programming languages the memory initialization and access patterns are not optimised. This limits the maximum amount of data that can be analysed. In addition the memory access performance is limited which provides the main bottleneck for calculations. The high-level computational languages do not provide tools for the low-level tuning of the code and developers must therefore rely on the optimization capabilities of the compilers of high-level programming languages. Typically the compilers do not include the most recent computational capabilities such as the latest processor instruction sets. Therefore the performance of the compiled code is further limited. In summary, despite the fact that data analysis using a code written in a high-level programming language has benefits over the use of third-party software the computational performance and memory consumption of such implementations are still below the limits required for the analysis of large sets of data.

Finally, one can use regular programming languages (such as C/C++) in order to develop the data analysis software. This gives the developer full control over the memory management and computational features. Therefore the custom code can

include all recent computational technology and can be thoroughly optimised for high performance calculations. This approach gives the developer the possibility to use the properties of particular data set in order to make assumptions within the code that can lead to major performance improvements.

I present custom software called *semargl* that has been developed by myself for the analysis of large amounts of data produced by micromagnetic simulations. The software is free to use and it is available for download from www.magnonics.org/semargl/ and includes unique methods of data analysis. Initially it was written in order to analyse data generated by OOMMF. However any data probed on a regular mesh could be analysed. For instance, the *Nmag* package has special extensions that transform data on an irregular mesh (widely used by FEM packages) into the form usable in OOMMF. Therefore *semargl* can be used to analyse data generated by *Nmag* as reported in Ref.73. At the present stage of development *semargl* is parallelized using the OpenMP framework. Its performance in single processor systems scales linearly with the number of computational cores. The parallelization is tuned to support NUMA by means of local-to-processor memory allocation. Therefore the performance of *semargl* scales almost linearly with the number of processors available in the system. *semargl* is not implicitly optimised for modern processor architectures. For this we rely on the compilation capabilities of C/C++ compilers. The DFT routines used in *semargl* are derived from the AMD ACML library[76] as permitted by its license. Our tests have shown that the AMD ACML library utilises the processor power on both AMD and Intel processor architectures excellently.

IV.2 Data pre-processing

The main advantage of custom data analysis software using low-level languages is the full control over the memory management afforded to the user. In

particular all operations with large arrays of data are done in-place and so no additional memory is required for the processing, except perhaps some small fraction of the temporal storage. The data operations in *semargl* are non-reversible and so the software does not store several instances of the data thereby reducing the workload on the memory.

semargl software has been developed with the analysis of linear magnetization dynamics in mind as described in Ref.24. Therefore we assume that the amplitude of the magnetization precession is small.

The result of micromagnetic simulation is the set of magnetisation vectors $\mathbf{M}(\mathbf{r}_{ijk}, \mathrm{t}_n)$ defined on discrete meshes both in time and spatial domains, and so $\mathbf{r}_{ijk}$ is the radius-vector of the cell of the 3D mesh with indices i, j, k, and t_n denotes the value of the time corresponding to the n^{th} time step. Due to the nature of the analysis our software requires that the spatial and time discretization be regular. Therefore results produced by the micromagnetic solvers based on the FEM scheme have to be interpolated to form a regular mesh. The latter interpolation is not a part of *semargl* and must to be done using other third-party software tools, as it is done for instance in *nmagprobe*[160]. The ground state of the magnetization is of the form $\mathbf{M}_0(\mathbf{r}_{ijk}, \mathrm{t}_n)$.

Then the deviation of the system from the ground state is calculated as follows

$$\mathbf{m} = \mathbf{m}\left(\mathbf{r}_{ijk}, \mathrm{t}_n\right) = \mathbf{M}\left(\mathbf{r}_{ijk}, \mathrm{t}_n\right) - \mathbf{M}_0(\mathbf{r}_{ijk}, \mathrm{t}_n), \qquad \text{(IV.2-1)}$$

This approach is valid even for large angle precession as long as the ground state is not altered by the excitation field. If necessary the subtraction of the magnetization of the ground state can be bypassed by user with the full magnetization vector being analysed in this case.

In linear approximation the form of the dynamic magnetization is given by

$$\mathbf{m} = \mathbf{m}_0 e^{i\omega t}, \qquad \text{(IV.2-2)}$$

where $\mathbf{m}_0$ is the amplitude of precession and ω is the corresponding frequency. Therefore spectral analysis requires only one component of the dynamic magnetization to be analysed in order to extract the resonances of the system. This component is orthogonal to the magnetization vector of the ground state, since the dynamic component of the magnetization parallel to the magnetization vector of the ground state is expected to be zero in the linear case. Therefore *semargl* allows the user to analyse *only one* component of the magnetization and thereby reduces the memory footprint by a factor of three. Nevertheless if the trajectory of precession is of interest to study then *semargl* can be used to analyse separately each particular component of the magnetization. The results can then be combined using third-party software. By performing the analysis in three stages we introduce a performance overhead caused by the multiple data loading from the storage devices. However the memory footprint is reduced allowing us to analyse larger data sets. At the same time the time for the data to load could be reduced by using *Solid State Drive (SSD) based Storage* which allows one to load data almost *5* times faster than when a regular magnetic data storage device is used.

IV.3 Probes

There are situations where it is necessary to analyse data from only a part of the simulated sample. This could be used for example to reproduce experimental conditions in the form of the profile of the optical spot used to probe the magnetic signal[92] in pump probe experiments that utilise ultra-fast lasers. There are also cases where the system exhibits a very complex dynamic response and so it is more convenient to analyse some of its parts separately so as to understand the origin of the overall response. Therefore *semargl* allows one to choose the part of the sample to be

analysed by using the concept of "probes". In particular *semargl* allows one to specify rectangular probes and can simulate the skin-depth and profile of the optical spot, which is assumed to have a Gaussian distribution. In this case, the general form of the probe is given by

$$p(\mathbf{r}_{ijk}) = e^{-\frac{\left(\mathbf{r}_{ijk}-\mathbf{r}_{0_{ijk}}\right)^2}{2\mathbf{d}^2}} e^{-\frac{\mathbf{r}_{ijk}-\mathbf{r}'_{0_{ijk}}}{\boldsymbol{\delta}}}, \tag{IV.3-1}$$

where $\mathbf{d}$, $\mathbf{r}_{0_{ijk}}$, $\boldsymbol{\delta}$ and $\mathbf{r}'_{0_{ijk}}$ denote the diameter and position of the centre of the optical spot and skin depth and surface of the sample, respectively. The probe can be applied not only to the entire sample, but to any of its rectangular regions.

In general, the probes affect all other calculations performed by *semargl*. The probe should be specified only once since all operations performed by *semargl* are non-reversible.

semargl software provides the user with an abstract representation of the sample based upon the absolute values of the magnetisation in the ground state or at one of the time steps, depending on the type of data pre-processing used. If the pre-processing involves the ground state of the magnetisation, then the image is extracted from the ground state. Otherwise, one of the time steps is used.

IV.4 Real space - time domain data analysis

In certain situations, analysis of the data in the real space time domain has some advantages over those in the real space frequency and reciprocal space frequency domains. In particular data represented in this way could be used to study scattering processes.

After the pre-processing described above the data takes the form of an array of scalar values. The data could be projected onto the (0, 1) interval and mapped to the predefined colour space. The colour space used by *semargl* takes gradation of blue and red for negative and positive values, respectively. *semargl* allows one to visualize the projection of the data onto each axis of the system under investigation. In particular to visualize the m_l component of the magnetization along the $\hat{r}_i$ axis and data can be averaged along the other axes by taking

$$\mathbf{m}(r_i, t_n) = \frac{1}{MN} \sum_j \sum_k p(\mathbf{r}_{ijk}) \mathbf{m}(\mathbf{r}_{ijk}, t_n), \tag{IV.4-1}$$

where M and N denote the number of cells in the mesh along the $\hat{r}_j$ and $\hat{r}_k$ axes respectively. The main disadvantage of such an averaging scheme is that any anti-symmetric magnetization dynamics along $\hat{r}_j$ and $\hat{r}_k$ will be averaged out. Nevertheless by configuring the probe function in such a way as to break the symmetry of the anti-symmetric modes it is possible to detect them.

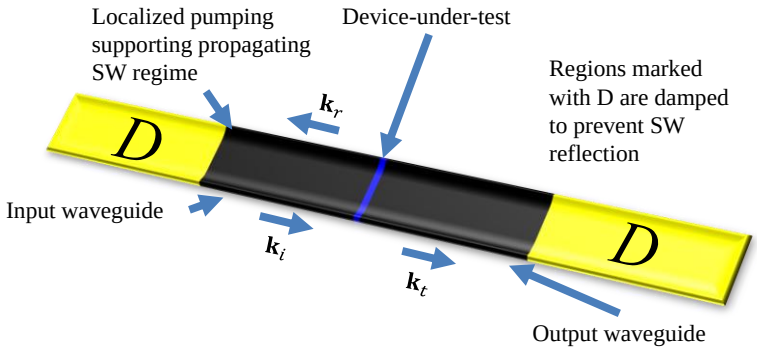

Figure IV.4-1 A schematic diagram of a simple magnonic device is shown. The device is represented by the Co layer in-between the Py waveguides. The regions marked *"D"* have magnetic parameters of Py with high damping so as to prevent back reflections of spin waves.

The real space time domain analysis detailed above has been applied to the geometry presented in Figure IV.4-1. The results are presented in Figure IV.4-2.

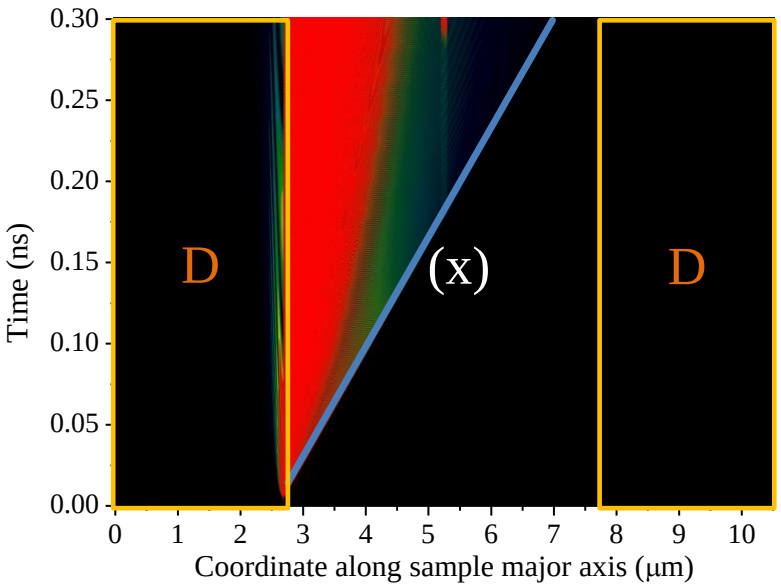

Figure IV.4-2 The propagation of spin waves is shown in the real space - time domain. The blue line represents the wave front of spin waves (marked as (X)).

The sample under investigation is a 1D Py nanowire. The end regions of the sample have an increased value of the damping constant - marked *"D"*. A Co layer is placed in the centre of the nanowire. Magnetization dynamics are excited by a small transient pulsed magnetic field localized in the small region near the left edge of the wire. We observe propagating spin waves moving along the length of the nanowire from the region on the left where the pulsed excitation was localised. The sloping line (X) represents the wave front of the spin waves. At some point the spin wave reaches the Co layer and is scattered from it. Some portion of the spin waves reflects back from the Co layer, while another part propagates through it. The interference of spin waves inside the Co layer leads to the formation of standing spin waves localized with the Co

layer. Figure IV.4-2 suggests that propagation of the spin waves in the layers with increased damping is negligible.

Thus by analysing the data in the real space - time domain allows one to use micromagnetic simulations to study the scattering of spin waves from non-uniformities in 1D magnonic waveguides and has the potential for further studies in 2D and 3D samples.

IV.5 Real space - frequency domain data analysis

In the time domain the magnetization dynamics at each point in the sample are a superposition of the different modes excited in the system. Therefore one cannot analyse the spatial character of each mode separately. However by transforming the magnetization dynamics into the frequency domain one can study the real space evolution of individual modes independently. For example this method could in principle be used to analyse the efficiency of magnonic crystals at desired operational frequencies. This could allow the prediction of the formation of band gaps and their size by analysing the spatial attenuation of spin waves.

This method is closely related to the one described earlier in Section IV.4. The only difference is that the data is transformed into the frequency domain prior to the spatial averaging. The absolute value of the amplitude of the Fourier image is spatially averaged as

$$\bar{\mathbf{m}}(r_i, \omega_n) = \frac{1}{MN} \sum_j \sum_k p(\mathbf{r}_{ijk}) \left| \tilde{\mathbf{m}}(\mathbf{r}_{ijk}, \omega_n) \right|, \qquad \text{(IV.5-1)}$$

In doing so, we exclude any phase information from the analysis. Therefore the spatial averaging performed using expression (IV.5-1) does not cancel any anti-symmetric modes. This gives one a great advantage over the real space time domain

analysis described in Section IV.4. Finally the spatially averaged data are then mapped onto the colour space as described in Section IV.4

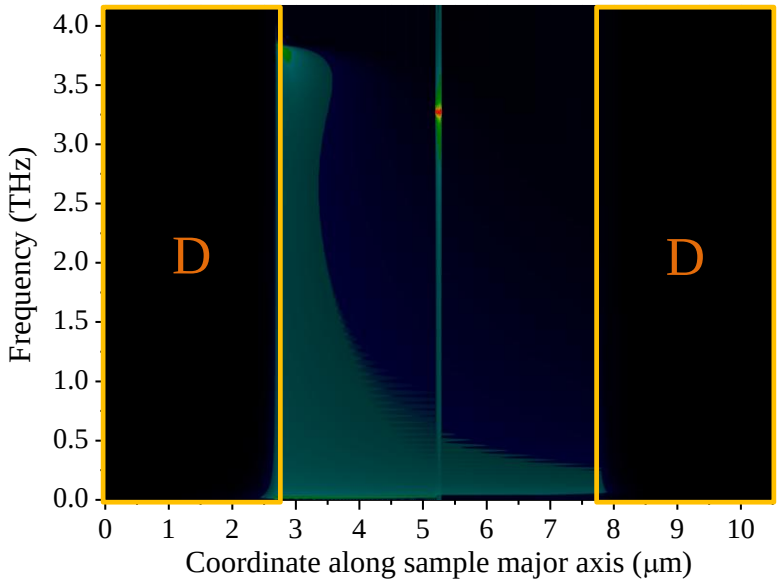

Figure IV.5-1 The propagation of spin waves as a function of their frequencies is shown.

An example of the real space frequency domain is shown in Figure IV.5-1. The geometry of the problem is identical to that described in Section IV.4. Essentially, Figure IV.5-1 represents a temporal Fourier image of Figure IV.4-2.

The data presented in Figure IV.5-1 suggests that the Co layer acts as a frequency selector for spin waves. In particular some spin waves pass through the Co layer while some are almost completely reflected from it. The Co layer accumulates some energy from the incident spin waves as is seen from the increased amplitude of the spin waves within the *Co* layer. Moreover resonant energy absorption is observed at higher frequencies of around 3.3 THz. In addition it is seen that at the lower frequencies the efficiency of the excitation of the spin waves is small. This could be attributed to the fact that spin waves cannot be excited below the FMR frequency of Py. The FMR frequency of Co is higher than that of Py in large part due to the higher value of the

saturation magnetization in Co. Within the range of frequencies between the FMR frequencies of the Py and Co the incident spin waves are completely reflected from the Co interface through which their propagation is not allowed.

The analysis of the data in the real space - frequency domain yields new advantages as compared to those in the real space - time domain. In particular one can study the spatial character of spin waves separately for each particular mode of the system.

IV.6 Frequency domain data analysis

Spectral analysis is one of the crucial methods for the investigation of the resonances of a magnetic systems. *semargl* software has three different methods by which to extract the frequency response of the system from the spatially and time resolved data produced by micromagnetic simulations.

Experimental techniques only have access to the spatial response of the system averaged over length scales which are limited by their spatial resolution. In particular current optical techniques have a diffraction limited spatial resolution of around *400 nm*[92,77]. Thus the magnetisation dynamics in truly nanoscale samples cannot be resolved in space at present and only the spatially averaged response can be measured. Therefore the first method realised in *semargl* simply reproduces the process of the data acquisition used in time-resolved experiments. At each time step the data is averaged over the volume of the sample in the real space and then transformed into the frequency domain by applying Discrete Fourier Transformation (DFT) as

$$\bar{\mathbf{m}}(\omega_n) = DFT_t\left(\frac{1}{MNL}\sum_i\sum_j\sum_k p(\mathbf{r}_{ijk})\mathbf{m}(\mathbf{r}_{ijk}, t_n)\right), \qquad \text{(IV.6-1)}$$

where L is the number of cells along $\hat{r}_i$ axis and DFT_t is the temporal DFT. This method has several disadvantages. First of all any anti-symmetric excitations of the system will be suppressed as discussed above. Nevertheless this is on par with experimental observations. The second disadvantage is the lack of spatial resolution when the simple averaging scheme is applied. In particular in order to understand the nature of the resonances of the system it is vital to investigate the spatial profile of each particular mode.

The second method implemented in *semargl* is free from the disadvantages described above. In particular it can be used to reconstruct the spatial profiles of the magnonic modes. Moreover the method does not suppress anti-symmetric modes. Therefore using the second method one should be able to extract virtually all possible resonances of the system limited only by the type of the excitation used in the simulations. Indeed if the symmetry of the excitation is orthogonal to that of a particular mode then either it will not be excited at all or its amplitude will be vanishingly small.

For the second method the temporal Fourier image is calculated for each cell in the mesh prior to the averaging as

$$\tilde{\mathbf{m}}(\mathbf{r}_{ijk}, \omega_n) = DFT_t\left(p(\mathbf{r}_{ijk})\mathbf{m}(\mathbf{r}_{ijk}, t_n)\right), \tag{IV.6-2}$$

The total spectrum is then calculated by averaging the Fourier amplitudes $\left|\tilde{m}_l(\mathbf{r}_{ijk}, \omega)\right|$ from

$$\bar{\mathbf{m}}(\omega_n) = \frac{1}{MNL}\sum_i \sum_j \sum_k \left|\tilde{\mathbf{m}}(\mathbf{r}_{ijk}, \omega_n)\right|, \tag{IV.6-3}$$

The spatially resolved temporal Fourier images of the magnetization calculated using expression (IV.6-2) are essentially the set of profiles of the magnetisation for any

particular frequency. Therefore the image of a particular mode could be reconstructed by mapping the amplitude of the mode onto the colour space at the frequency of ω_i

$$\mathbf{m}(\mathbf{r}_{ijk}) = \tilde{\mathbf{m}}(\mathbf{r}_{ijk}, \omega_n)\big|_{\omega=\omega_i}, \tag{IV.6-4}$$

The frequency of the resonances ω_i can be extracted from the calculated spectra using either expression (IV.6-1) or (IV.6-3). Therefore the second method gives much greater insight into the dynamical processes occurring in the investigated system as compared to the first method described earlier.

The spectrum calculated using the second method contains contributions from all modes of the system. Sometimes it is more convenient to analyse only lower-order modes (modes having a low number of nodal lines) while excluding higher-order modes from the analysis. The presence of the higher-order modes can effectively increase the line width of the resonances making the spectrum insufficiently clear for the analysis. Moreover by reducing the impact of the higher-order modes it is possible to suppress some artefacts of the simulations; this will be described in Section IV.8. The third method of spectrum calculation aims to address the problem of the analysis of the modes within a certain range of values of wave vector.

In order to exclude the impact of higher-order modes on the response of the system one has to transform the real space frequency domain data into the reciprocal space by applying the spatial DFT as follows

$$\tilde{\mathbf{m}}(\mathbf{k}_{ijk}, \omega_n) = DFT_r\left(\tilde{\mathbf{m}}(\mathbf{r}_{ijk}, \omega_n)\right), \tag{IV.6-5}$$

where DFT_r denotes the spatial *DFT*. Then only modes with whose wave vectors lay within a certain range $|\mathbf{k}, \mathbf{k} + \Delta\mathbf{k}|$ are averaged in the reciprocal space as shown by

$$\bar{\mathbf{m}}(\omega_n) = \frac{1}{N'}\sum_i \sum_j \sum_k \left|\tilde{\mathbf{m}}(\mathbf{k}_{ijk}, \omega_n)\right|, \quad \text{(IV.6-6)}$$

where N' denote the number of cells in the reciprocal space lying within the range of the wave vectors spanning $|\mathbf{k}, \mathbf{k} + \Delta\mathbf{k}|$.

The only disadvantage of the third method is the lack of possibility to reconstruct the spatial profiles of the modes as the entire data is transformed into the reciprocal space. Nevertheless it is possible to reconstruct the spatial profiles of the resonances using the second method with the frequencies extracted from the spectrum calculated using expression (IV.6-6).

Examples of the spectral analysis performed using the three different methods are presented in Figure IV.6-1. The different methods of analysis were applied to an isolated nano-element made of Py. The lateral dimensions of the element are 100x50x10 nm. An external field of 1.5 kOe was applied along the long axis of the element. The profiles of the Fourier amplitude and the phases of the modes were extracted using the second method. The spectrum acquired with the first method shows a reduced number of resonant peaks, as expected. The third method suppresses the mode of frequency at approximately 29.27 GHz. The spatial profile of this mode suggests that it is perfectly anti-symmetric, so that the phase of the oscillations is shifted by π between the adjacent cells. This mode is expected to have a frequency far above the considered range because of the large effect of the exchange interaction. Therefore we attribute the observation to artefacts in the simulations. Since such artificial modes have very large wave vectors they can be easily suppressed by using the third method of analysis.

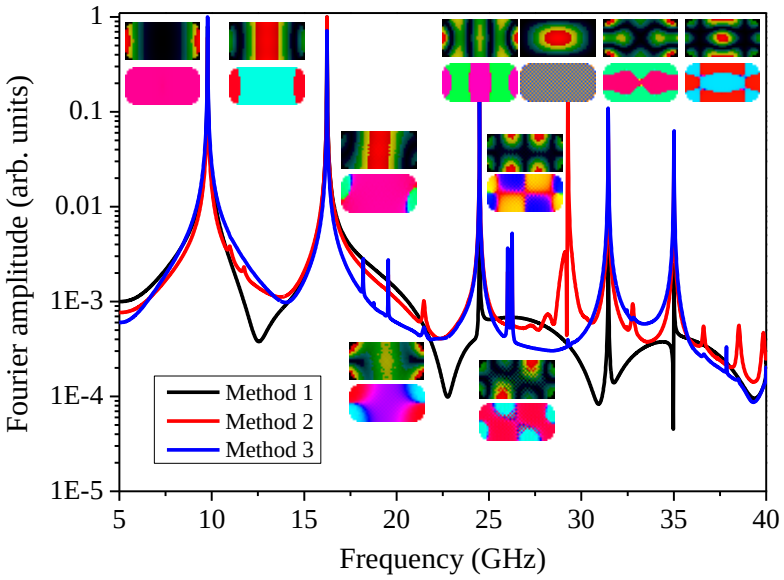

Figure IV.6-1 The spectra of magnetization dynamics along with the spatial profiles of the dominant magnonic modes are shown for an isolated nanoscale rectangular element.

The reduced amplitude of non-uniform modes can be explained by their reduced coupling to the uniform excitation normally used in the simulations.

Finally by utilizing the three methods of analysis described above it is possible to extract the entire set of resonances of the system along with their spatial profiles. Such an approach is very useful for studies of spin wave confinement in a variety of magnetic structures. However this method does not allow one to investigate the dispersion of spin waves quantitatively. Only qualitative analyses could be performed by estimating the dependence of the mode frequencies on the number of nodal lines in the mode spatial profiles.

IV.7 Reciprocal space - frequency domain data analysis

The dispersion of excitations is the most widely used approach for the characterization of systems in solid state physics. As compared to the data represented

in the real space time domain the dispersion gives complete information about the system in a form that is most suitable for gaining understanding as well as further analysis. For instance band-gaps in the dispersion relation are an indication of some spatial periodicity of particular parameters of the system. The width of the band-gap gives insight into the depth of the periodic modulation of said parameters. In addition the dispersion could be used to detect localized modes since they have no spatial dispersion. Therefore in order to investigate spin waves in magnetic systems it is essential to be able to extract the full magnonic dispersion relation from micromagnetic simulations.

To calculate the dispersion of spin waves one should transform the real space time domain data into the reciprocal space frequency domain as given by expression (IV.6-5). As spin waves are characterized by spatial dispersion, in the reciprocal space frequency domain they exist only in particular points as given by their dispersion relation ($\mathbf{k}$). Therefore local maxima of the magnetization amplitude $\tilde{\mathbf{m}}(\mathbf{k}_{ijk}, \omega_n)$ in the reciprocal space frequency domain correspond to spin wave excitations. Thus, by applying a suitable algorithm to estimate the coordinates of the local maxima of $\tilde{\mathbf{m}}(\mathbf{k}_{ijk}, \omega_n)$, it is possible to extract the frequencies and the wave vectors of spin waves in the given system. In particular the spin wave dispersion could be extracted by estimating the roots of the following equation

$$\left.\frac{\partial \tilde{\mathbf{m}}(\mathbf{k}_{ijk}, \omega_n)}{\partial \mathbf{k}_{ijk}}\right|_{\omega_n = const} + \left.\frac{\partial \tilde{\mathbf{m}}(\mathbf{k}_{ijk}, \omega_n)}{\partial \omega_n}\right|_{\mathbf{k}_{ijk} = const} = 0. \qquad \text{(IV.7-1)}$$

However equation (IV.7-1) cannot be easily solved in the general case. Moreover the system can have several dispersion branches with very close differential parameters (such as gradients). Thus, the reconstruction of the shape of the dispersion curve requires sophisticated algorithms to distinguish different dispersion branches to be

developed. Therefore at the present stage of its development the *semargl* software cannot extract quantitatively the dispersion of spin waves in the form of tabulated data. Nevertheless, this feature has been implemented for the case of a single dispersion branch (the case which can be simply analysed without sophisticated algorithms of separating of different dispersion brunches) as described in Section VIII. At the moment, this feature is missing from the *semargl3* software and planned to be implemented in future releases.

The qualitative character of the dispersion can be investigated by mapping magnetization amplitude the $\tilde{\mathbf{m}}(\mathbf{k}_{ijk}, \omega_n)$ onto the colour map as discussed in Section IV.4. Then the shape of the dispersion and its main features can be estimated. Moreover the acquired image could be overlapped with an image one obtained experimentally that gives the same information, e.g. the regular *Brillouin Light Scattering* (BLS)[78],[79].

The main advantage of this technique for the calculation of magnonic dispersion curves is that the amplitude of the spin waves, $\tilde{\mathbf{m}}(\mathbf{k}_{ijk}, \omega_n)$, is always extracted in addition to the values for their wave vectors and frequencies. This amplitude can be used to study scattering processes in the magnetic system, as will be discussed in Section VIII.

An example of the spin wave dispersion extracted from OOMMF simulations is shown in Figure IV.7-1. The simulations were performed on the structure investigated experimentally in Ref. 80. In particular a Py stripe having dimensions of 40 μm x 0.6 μm x 30 nm was studied. An external field of 2.9 kOe was applied parallel (Figure IV.7-1(a)) and perpendicular (Figure IV.7-1(b)) to the long axis of the stripe. Several dispersion branches were observed when the field was parallel to the major axis of the sample. In the region of small wave vectors the entire set of dispersion branches is characterized by negative dispersions as it is expected for the BVMSSW geometry[24].

When the value of the wave vectors increases the exchange interaction eventually overcomes the magneto-static interaction at which point positive dispersion is observed. The presence of several dispersion branches is associated with spin wave confinement in the transverse direction. In particular observed dispersion branches differ by the values of the transverse component of the wave vector.

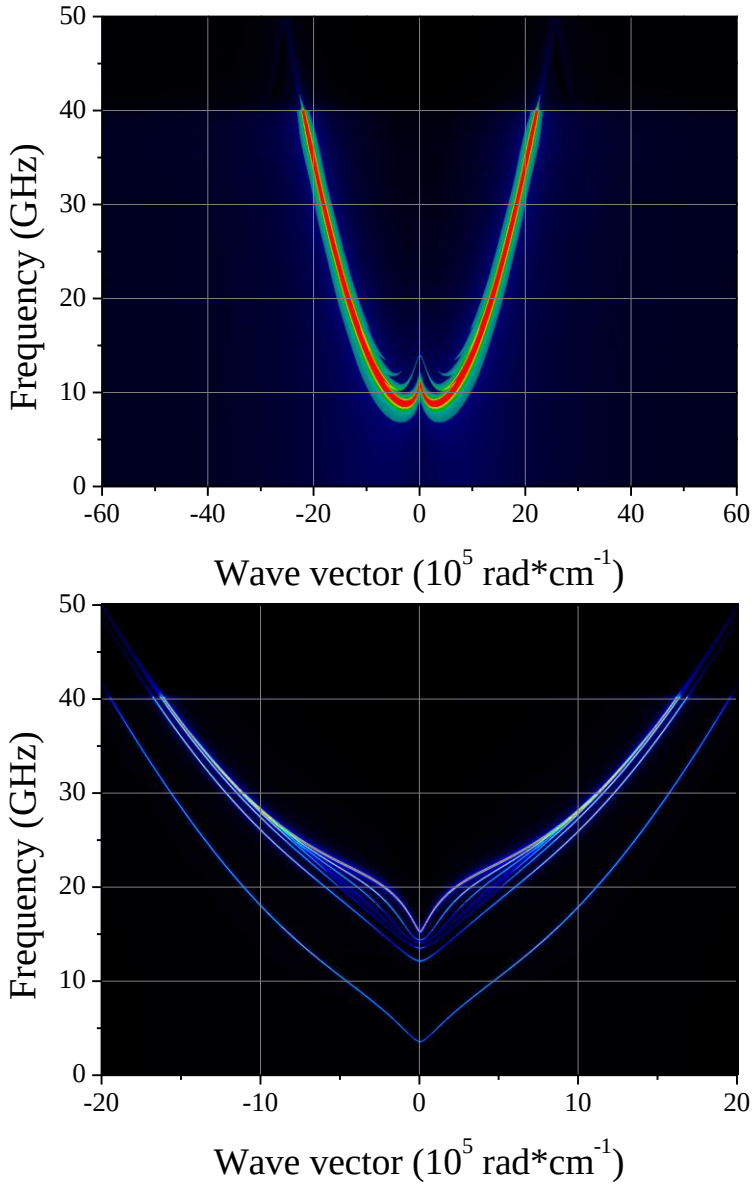

Figure IV.7-1 The spin wave dispersion is shown for the directions parallel (top panel) and perpendicular (bottom panel) to the direction of magnetisation in the ground state.

The transverse direction is characterized by positive dispersion as it coincides with the geometry studied by Damon and Eshbach[81]. Thus a higher value of the transverse wave number corresponds to branches of higher frequencies. The intensity of these branches decreases as the value of the transverse wave vector increases. This effect is related to the fact that when modes become more spatially non-uniform their coupling to the uniform excitation decreases.

When the field is applied perpendicularly (Figure IV.7-1(b)) positive dispersion is observed. This is in agreement with the expectations for the Damon-Eshbach geometry. As in the case of BVMSSW geometry several dispersion branches are observed. The lowest frequency branch is associated with spin waves localized in the demagnetized regions - where the value of the internal field is reduced[144] and so the frequencies are reduced as compared to the higher frequency group. The BVMSSW geometry does not have such demagnetized regions therefore this type of spin waves is not observed in the case when the field was applied along the major axis of the wire. The transverse component of the wave vector is now associated with the BVMSSW geometry. Thus, if the value of the transverse component of wave vector increases the frequency of the dispersion branch decreases. The reduced intensity of the dispersion branches could be explained by their reduced coupling to the spatially uniform excitation field as was described above for the BVMSSW geometry.

In conclusion the calculation of the spin wave dispersion gives one a powerful tool for understanding the physics of the observed effects.

IV.8 General notes on the analysis of the data using *semargl* software

The major disadvantage of computational techniques such as FDTD and FEM is that the volume of the sample and the time domain are discretised. Thus continuous

functions are replaced with ones that are defined only at certain points in space and time. The parameters of the spatial and temporal sampling define the properties of the Fourier transformation of the discrete datasets. Therefore the parameters of the discretization may affect the analysis performed by the *semargl* software.

Let us consider a volume discretised in a mesh with cells having dimensions of $\Delta\mathbf{r}$, while the time domain is regularly divided into intervals of time Δt. Thus according to the Nyquist–Shannon sampling theorem[82,83] the bandwidth of the spatial and temporal signals for the given discretisation will be limited by

$$\mathbf{k}_{\max} = \frac{\pi}{\Delta\mathbf{k}} \qquad \omega_{max} = \frac{\pi}{\Delta t} \tag{IV.8-1}$$

where $\mathbf{k}_{\max}$ and ω_{max} define the maximum possible values of the wave vector and the frequency corresponding to the sampling in space and time respectively. Thus, if the bandwidth of the continuous signal $\mathbf{M}(\mathbf{r}, t)$ is above the maximum value of the discrete representation $\mathbf{M}(\mathbf{r}_{ijk}, t_n)$ as given by the Nyquist–Shannon sampling theorem, the shape of the continuous signal may be misrepresented by the sampling. In particular the signals at wave vectors or frequencies above the limiting values cannot be distinguished from the lower frequency signals that lie within the allowed bands. This effect is referred as signal aliasing. Typically signal aliasing results in additional artificial signals appearing in the discretised data.

Therefore any simulations should be adjusted in order to exclude aliasing of the signal. In particular the excitation frequency of the spin waves has to be lower than the bandwidth of the simulations, fixed at ω_{max} by the time domain sampling. The same applies to the spatial character of the excitation, and so the spatial profile of the

excitation should have a bandwidth lower than $\mathbf{k}_{max}$ fixed by the dimensions of the spatial mesh.

If the form of the excitation is not fixed by the study, e.g. the investigation is not aiming to reproduce experimental conditions, and then there is a simple method to control the spatial and frequency bandwidths of the excitation. The method is based on the unique properties of the sinc function, which defined as

$$\mathrm{sinc}(x) = \frac{\sin(\lambda x)}{\lambda x} \qquad \text{(IV.8-2)}$$

The representations of the *sinc* function in the real and reciprocal domains are shown in Figure IV.8-1. The useful feature of the *sinc* function is that its Fourier image is given by the rectangular function $\mathrm{rect}(\lambda)$. Therefore by varying the parameter λ of the *sinc* function it is possible to control its bandwidth.

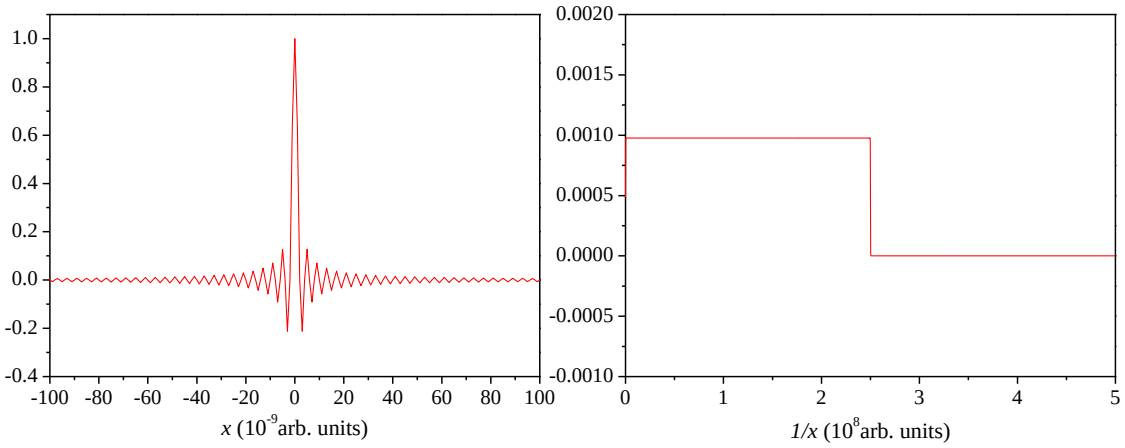

Figure IV.8-1 The temporal (left panel) and frequency (right panel) profiles of the sinc function are shown.

In simulations it is necessary to define the temporal and spatial profiles of the excitation using a superposition of *sinc* functions to control the bandwidth of the

excitation. For instance if the excitation is realized by means of a time-varying applied field then the spatial and temporal profile of this field have to be defined by

$$\mathbf{h}(\mathbf{r}_{ijk}, t_{\mathrm{n}}) = \mathbf{h}_0 \mathrm{sinc}(\mathbf{k}_0 \mathbf{r}_{ijk}) \mathrm{sinc}(2\pi f_0 t_n) \qquad \text{(IV.8-3)}$$

where $\mathbf{h}_0$ denotes the amplitude of the excitation, while $\mathbf{k}_0$ and f_0 are its spatial and frequency bandwidths respectively. Thus by simply adjusting the bandwidth of the excitation so that $\mathbf{k}_0 < \mathbf{k}_{max}$ and $f_0 < f_{max}$ it is possible to avoid the artefacts of sampling so that the analysis performed by *semargl* will not produce artefacts.

IV.9 Conclusions

semargl software provides a unique infrastructure for the analysis of dynamical data from micromagnetic simulations. By combining the information acquired using the entire set of analysis methods implemented in semargl it is possible to understand the physics of the effects observed in the studied system. For instance the dispersion analysis can be followed by the spectral analysis in order to reconstruct the spatial profiles of the modes of different dispersion branches.

semargl software has been developed to support only data produced by OOMMF simulations. Nevertheless by converting the output of any micromagnetic package to the format of OOMMF data it is possible to use *semargl* with virtually any micromagnetic package. *semargl* software extracts all necessary information about the simulation from the headers of OOMMF files. Therefore in order to make *semargl* work correctly third-party converters should be strictly compliant with the OOMMF format of data[55]. There is only one converter at the moment in the form of an extension to the Nmag micromagnetic package. Despite the fact that it is not strictly compliant with OOMMF specifications it could be used to convert the data into the OOMMF format. Thus the data produced by Nmag could be analysed using the *semargl* software[73].

Finally, *semargl* includes most recent computational technologies, such as parallel processing techniques. Therefore it can utilize all computational resources in a range of computational environments, thereby making processing extremely fast. Nevertheless the software is in an active stage of development and I am planning to adopt General-Purpose Computing on Graphics Processing Units (GPGPU) technology in order to make analysis even faster as shown in Ref. 84. Additionally *semargl* software has been developed with as small a memory pressure as makes possible to analyse large dataset produced by micromagnetic simulations.

V Collective precessional modes of pairs of closely spaced magnetic nano-elements

V.1 Introduction

There are several different magnetic interactions that define the collective oscillatory behaviour of coupled magnetic moments (spins). This results in spin waves (magnons)[24,46] exhibiting very different properties from many other kinds of waves (quasi-particles) currently studied in solid state physics. Moreover, the magnetic-dipole interaction is highly anisotropic and spatially non-uniform, leading to an anisotropic dispersion and a strong confinement of spin waves. In the past decade spin waves in isolated magnetic elements of different shapes and sizes, as well as arrays, have been extensively studied[85,86,87,88,89,90,91,92,93,94,95]. Interest in such systems has been fuelled by both the existing and potential applications of spin waves and nano-patterned magnetic media in high density data storage[96], microwave signal processing[97,98] and magnonic meta-materials[92,32].

As the packing fraction of magnetic arrays increases, the magnetic-dipole coupling between elements also increases and eventually reaches a point where it has a

dramatic effect on dynamical behaviour of the system. In particular the magnetization dynamics are no longer described by precessional (spin wave) modes of individual elements. Instead collective normal modes of precession are formed[92]. This behaviour is common to all systems of coupled oscillators, and a thorough understanding of such behaviour forms a fundamental part of any field of modern solid state physics. Collective spin waves in closely packed 2D magnetic arrays have been observed by Time Resolved Scanning Kerr Microscopy (TRSKM)[89,92] as well as Brillouin Light Scattering (BLS)[87,91,94], with the interpretation usually based upon qualitative agreement with micromagnetic simulations or analytical models. This highlights the need to gain a greater understanding of the collective spin wave modes observed in systems of closely packed magnetic elements.

In this chapter I present a numerical and theoretical study of collective spin wave modes in pairs of magnetic elements, as this is the simplest magnetic system in which collective precessional modes can be observed. The study is based upon comparison of results of micromagnetic simulations performed in OOMMF with results generated using an analytical theory that generalises the theory proposed in Refs. 86, 93. The analytical theory allows one to calculate the frequencies of collective modes of virtually any system of coupled magnetic elements and takes the spectrum and associated mode profiles of an isolated element as its starting point. The spectrum and mode profiles of the isolated element are calculated using micromagnetic simulations.

V.2 Theory

Perturbation theory is applied to the numerical solution of the Landau-Lifshitz equation for an isolated element (e.g. the one shown in Figure V.2-1(a)) in order to calculate the splitting of the element's resonant spin wave modes induced by the magnetic-dipole interaction with its environment in pairs of such elements (e.g. those

shown in Figure V.2-1(b) and (c)). This is a generalisation of the approach developed in Ref. 86 for an array of magnetic dots in a vortex state. Although this approach is also applicable to arbitrarily large or infinite arrays of magnetic elements, the corresponding general theory and its comparison with micromagnetic simulations is beyond the scope of this thesis.

Let us first assume a uniform magnetization along the long axis of the elements $\mathbf{M}_{ground} = M_s \mathbf{e}_{\boldsymbol{x}}$ for their ground state. For an isolated element, any spin wave mode can then be represented by the normalized magnon amplitudes a^+ and a which are expressed as magnon creation and annihilation operators[86]

$$\begin{aligned} M^y(\mathbf{r}) &= \sqrt{\mu_B M_0}\left(g(\mathbf{r})a^+ + g^*(\mathbf{r})a\right), \\ M^z(\mathbf{r}) &= i\sqrt{\mu_B M_0}\left(f(\mathbf{r})a^+ - f^*(\mathbf{r})a\right). \end{aligned} \tag{V.2-1}$$

Here the functions $g(\mathbf{r})$ and $f(\mathbf{r})$ describe the non-uniform mode profile and are normalized by such that $\int_{dot} g(\mathbf{r})f(\mathbf{r})d^3\mathbf{r} = 1$. For an isolated element the Hamiltonian takes the canonical form $H = \hbar\omega^{(0)}a^+a$, where $\omega^{(0)}$ is the mode frequency. The coupling between the precessional dynamics of the same mode located in different elements which are centered at points $\boldsymbol{l}$ and $\boldsymbol{l}+\boldsymbol{\delta}$ is determined by the magnetic dipole interaction. For the case of two interacting elements this can be written through the operators a_1^+, a_1 and a_2^+, a_2, corresponding to the first and second elements of the system, as

$$\mathcal{H} = \hbar\omega_0(a_1^+a_1 + a_2^+a_2) + \frac{\hbar}{2}\left[\left(J_{\boldsymbol{\delta}}^y - J_{\boldsymbol{\delta}}^z\right)a_1^+a_1 + \left(J_{\boldsymbol{\delta}}^y + J_{\boldsymbol{\delta}}^z\right)a_2^+a_2 + \text{h. c.}\right] \tag{V.2-2}$$

where $\boldsymbol{\delta}$ is the radius-vector connecting the centres of the elements. The coefficients are given by

$$J_{\boldsymbol{\delta}}^{y} = \gamma M_s \int_V \int_V \frac{\left(1 - 3\left(v_{\boldsymbol{\delta}}^{y}\right)^2\right)}{|\boldsymbol{\delta} + \mathbf{r}_2 - \mathbf{r}_1|^3} g(\mathbf{r}_1)\, g(\mathbf{r}_2) d^3\mathbf{r}_1 d^3\mathbf{r}_2,$$

$$J_{\boldsymbol{\delta}}^{z} = \gamma M_s \int_V \int_V \frac{f(\mathbf{r}_1) f(\mathbf{r}_2)}{|\boldsymbol{\delta} + \mathbf{r}_2 - \mathbf{r}_1|^3} d^3\mathbf{r}_1 d^3\mathbf{r}_2, \qquad \text{(V.2-3)}$$

where $\boldsymbol{v}_{\boldsymbol{\delta}} = \frac{(\boldsymbol{\delta}+\mathbf{r}_2-\mathbf{r}_1)}{|\boldsymbol{\delta}+\mathbf{r}_2-\mathbf{r}_1|}$, γ is the gyromagnetic ratio, M_s is the saturation magnetization and the over $\mathbf{r}_1$ and $\mathbf{r}_2$ is performed over the first and second elements, respectively. The coefficients $J_{\boldsymbol{\delta}}^{y}$ and $J_{\boldsymbol{\delta}}^{z}$ are calculated for different orientations of the elements in the pair using the same functions $f(\mathbf{r})$ and $g(\mathbf{r})$ that are obtained from simulations of an isolated element. The normal mode frequencies of the coupled elements can then be represented by

$$\omega_{\pm} = \sqrt{\left(\omega_0 \pm J_{\boldsymbol{\delta}}^{y}\right)\left(\omega_0 \pm J_{\boldsymbol{\delta}}^{z}\right)}. \qquad \text{(V.2-4)}$$

In the following, the frequencies ω_0 of the dominant modes and the corresponding functions $f(\mathbf{r})$ and $g(\mathbf{r})$ were extracted from OOMMF simulations performed for the isolated element shown in Figure V.2-1(a). The results are then used in conjunction with equations (V.2-1) - (V.2-4) to calculate the frequency splitting of the dominant modes in the isolated element into the corresponding acoustical and optical modes of the pairs of elements that shown in Figure V.2-1(b) and Figure V.2-1(c). The splitting is then compared with the corresponding values extracted from simulations performed for the pairs of elements.

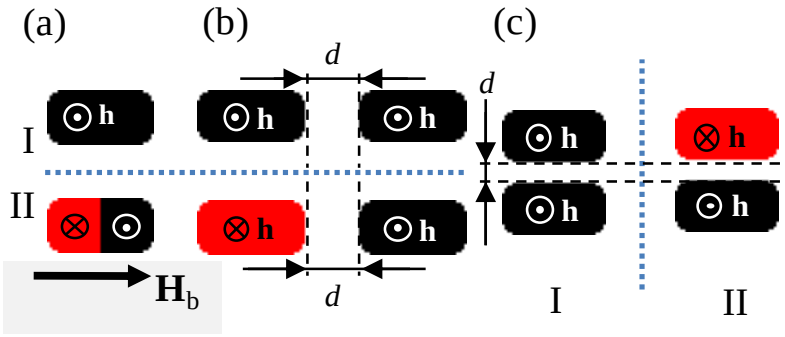

Figure V.2-1 The geometry of the problem is presented for an isolated magnetic element (a) and for pairs of magnetic elements with their major (b) and minor (c) axes aligned. Indices I and II represent the spatially uniform and anti-symmetric excitation fields respectively. Red and black correspond to mutually opposite directions of the excitation field. The insets are schematics of the coordinate system of the calculations and the orientation of the bias magnetic field.

V.3 Micromagnetic simulations

Throughout the simulations 100 x 50 x 10 nm^3 rectangular elements with rounded corners of radius of curvature 10 nm were assumed (Figure V.2-1). The magnetic parameters were close to those of *Py*[99], with the magnetic anisotropy neglected. To increase the spectral resolution the damping constant was set to a reduced value of 10^{-4}. The discretisation cell was taken as 2.5 x 2.5 x 10 nm^3. The magnetic ground states of the samples were obtained by means of a quasi-adiabatic relaxation from the completely in-plane saturated state at a field of 1300 Oe which was then gradually reduced in 5 Oe steps to the state at a bias field, H_b, of 200 Oe. The initial saturation and the applied fields were all parallel to the same in-plane direction, which

was canted by 10° from the major axis of the element; the reason for the canting will be explained later.

In the dynamical simulations the prepared static states were excited by an out-of-plane magnetic field with a sinc temporal profile: $H_e = H_0 \frac{sin(2\pi f_{max(t-t_0)})}{2\pi f_{max(t-t_0)}}$ and amplitude $H_0 = 10\ Oe$; $f_{max} = 20\ GHz$ is the cut-off frequency of the excitation. The centre of the excitation field was shifted by a time, t_0, spanning 20 zeroes of the sinc function. The dynamical states, $\mathbf{M}(\mathbf{r}, t)$, of the samples were recorded within 80 ns after the excitation with a step size, dT, of 10 ps. The subsequent Fourier analyses were therefore limited to frequencies up to $f_{BW} = \frac{1}{2dT} = 50\ GHz$. The ground magnetic state was subtracted from the transient magnetic states so that only the dynamic magnetization was analysed. The mode spectra were calculated by means of a point-wise DFT with a rectangular square window applied to the time resolved data and subsequent averaging of the DFT amplitude over the entire sample (method 2 of *semargl* as described in Section IV.6). The frequencies of the individual modes were extracted by fitting the spectral peaks to Lorentzian functions. Finally, spatial profiles of the amplitude and phase of individual modes at fitted frequencies were re-constructed from the point-wise DFT data. The spatial profiles were used to classify the character of the observed modes. Modes whose amplitudes are localized near the edges of an element were identified as "edge-type", while de-localized modes were identified as "bulk-type"[89].

As shown in Figure V.2-1 three different geometries were considered; (a) an isolated element, (b) a pair of elements with their shorter edges facing each other (and hence their major axes aligned with one another), and (c) a pair of elements with their longer edges facing each other (and hence their minor axes aligned with each other).

Two sets of simulations were performed, the first with a spatially uniform excitation field and the second with an anti-symmetric excitation field. Symmetric (acoustical) and anti-symmetric (optical) modes are expected to be excited by the uniform and anti-symmetric fields respectively.

The individual elements (both in isolation and when forming one half of a pair) were found to favour the "flower" ground state. It is also possible to induce the S state by increasing the tilt angle of the bias field. We found that the ground magnetic state had little or no influence on the dominant mode frequencies, while it affects their profiles more significantly. As a result the discussion in this thesis is limited to results obtained for elements in the flower state.

V.4 Results

The spectra of spin waves excited in the isolated element by applying uniform and anti-symmetric driving fields are shown in Figure V.4-1(a) and Figure V.4-1(b) respectively. In both cases two dominant modes were observed, a finding which is consistent with Ref. 92. For symmetric excitation, acoustic "edge" (AE) and acoustic "bulk" (AB) modes were observed at frequencies of $f_{AE} = 4.1\,GHz$ and $f_{AB} = 11.76\,GHz$, respectively. For the anti-symmetric excitation optical edge (OE) and optical bulk (OB) modes were observed at frequencies of $f_{OE} = 3.77\,GHz$ and $f_{OB} = 15.11\,GHz$ respectively. The acoustical modes are characterized by the uniform phase profile, while optical modes experience a phase shift of π. The change from the acoustical to optical character therefore manifests itself via an additional nodal line in the phase profile and the associated increase in the non-uniformity of the amplitude profile, which could also be interpreted as an increase of the effective wave number associated with the mode. However, this change is accompanied by frequency shifts of opposite sign - "red" and "blue" - for the cases of the edge and bulk modes respectively.

This difference can be explained by the different relative importance of the exchange and magneto-dipole interactions for the two mode types. The exchange and magneto-dipole interactions induce blue and red frequency shifts respectively in both cases. Taking the bulk mode behaviour as a reference, the reduced effect of the exchange interaction upon the edge mode frequency is explained by the additional nodal line being located where the mode amplitude is already minimal. The enhanced effect of the magneto-dipole interaction could be due to the increased localization of the mode amplitude in the demagnetized regions near the edges, since region of localization slightly changes when the mode character changes from acoustical to optical.

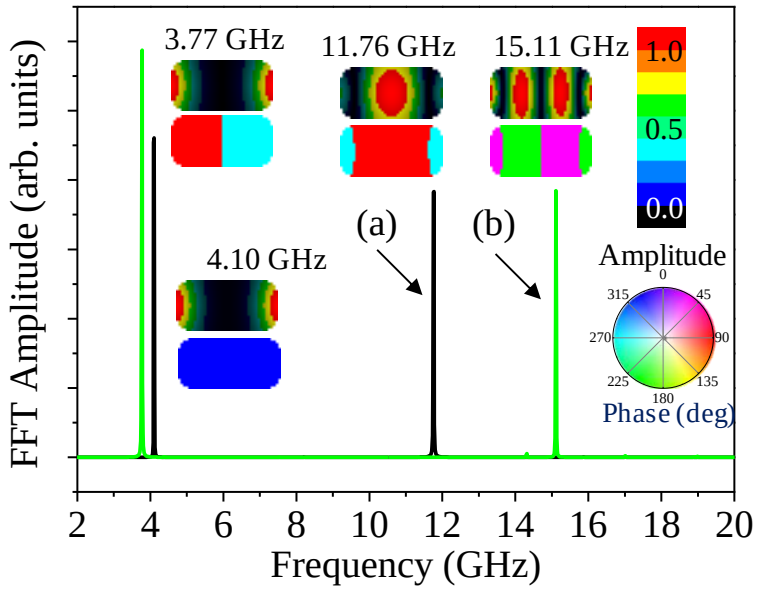

Figure V.4-1 The spectra of spin waves excited in the isolated element are shown for the case of a spatially uniform (a) and an anti-symmetric (b) excitation together with the corresponding mode profiles. The optical edge and bulk modes show reduction and increasing of their frequencies with respect to corresponding acoustical modes.

Figure V.4-2 shows mode spectra calculated from simulations for pairs of elements in which elements faced each other with their shorter side (2x1 arrays), with

the edge-to-edge separation, *d*, equal to 5, 10, 20, and 50 nm. The various spectra each contain three dominant peaks. The frequencies of the collective acoustical modes are always higher than those of the corresponding collective optical modes, although the difference is small in the case of AB and OE modes (using the classification introduced earlier for the isolated element). In each spectrum the highest frequency peak corresponds to either an acoustical or optical collective mode (according to the symmetry of the excitation) that has an AB character within individual elements. The corresponding amplitude profile is nearly identical to that observed in the isolated element. The AB mode can therefore be said to have a profile that is "rigid" with respect to the magneto-dipole interaction between elements in this geometry.

Such "rigidity" is not observed in the case of the AE and OE modes. The amplitude profiles of the collective AE and OE modes differ from those of the same modes observed in isolated elements so much that the two opposite edges of an individual element might even appear to act independently. The AE and OE modes can therefore be said to have profile that is "soft" with respect to the magnetic dipole interaction between elements. The identified "rigidity" of the bulk and "softness" of the edge modes is consistent with the aforementioned frequency changes experienced by the modes upon "twisting" their profiles by 180 degrees that is required to convert them from the acoustical to optical character.

Figure V.4-3 shows mode spectra calculated from simulations of pairs of elements in which the elements faced one other with their longer side (1x2 arrays), with the edge-to-edge separation, *d*, equal to 5, 10, 20, and 50 nm. Again, the spectra each contain three dominant peaks with the highest frequency peak always corresponding to the collective mode originating from the AB mode of the isolated element. In contrast to the 2x1 case, the frequencies of the collective acoustical modes can be both lower and

higher than those of the corresponding collective optical modes. The AB mode is still quite “rigid”, while the AE and OE modes can still be said to have profiles that are “soft” with respect to the magneto-dipole interaction between elements. However, neither manifest themselves as clearly as in the case of the 2x1 arrangement.

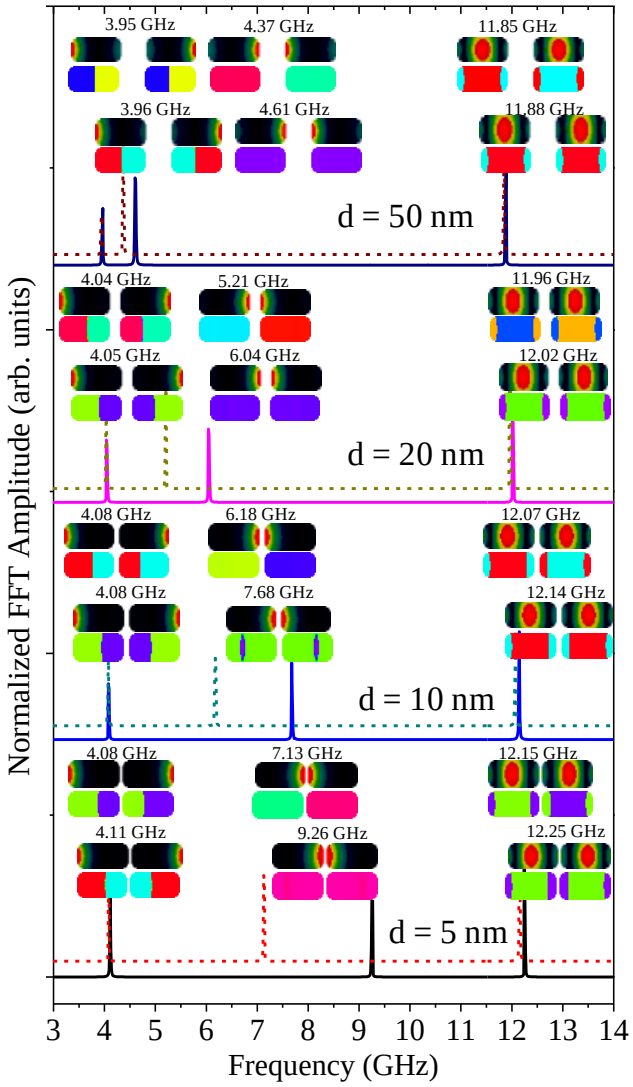

Figure V.4-2 The mode spectra of the pairs of elements with their major axes aligned (2x1 arrays) are shown together with the associated mode profiles. In each panel the lower and upper spectra correspond to excitation by a uniform and an anti-symmetric field respectively. The convention applies to the insets showing the mode profiles and frequencies.

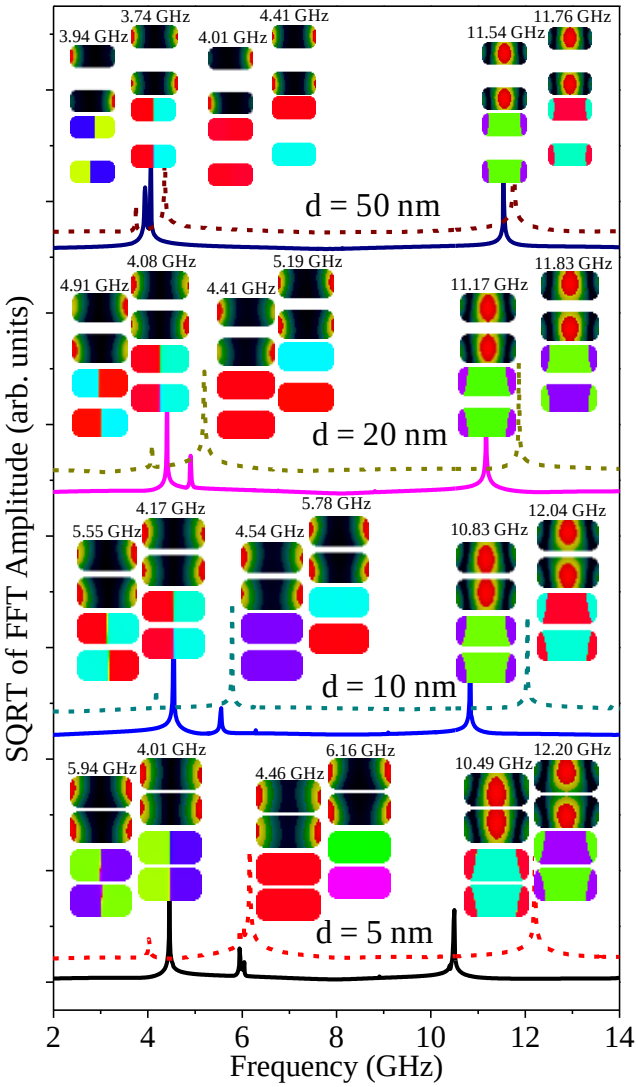

Figure V.4-3 The mode spectra of the pairs of elements with their minor axes aligned (1x2 arrays) are shown together with the associated mode profiles. The different panels correspond to different edge-to-edge separations. In each panel the lower and upper spectra correspond to excitation by a uniform and an anti-symmetric field respectively. The convention applies to the insets showing the mode profiles and frequencies.

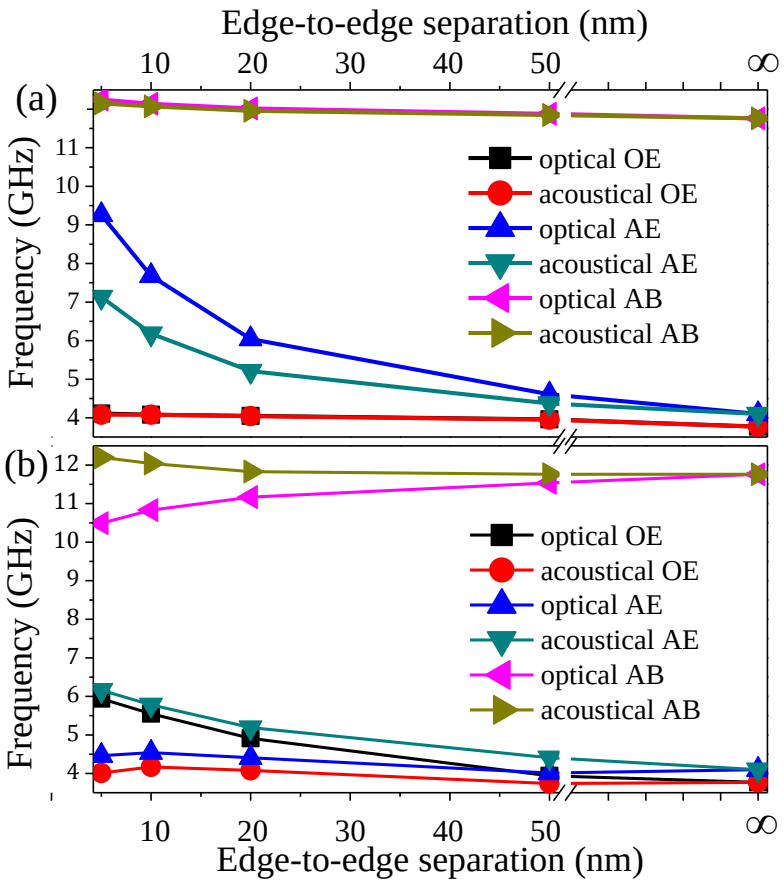

Figure V.4-4 The collective mode frequencies are plotted as a function of the edge-to-edge separation, *d*, for pairs of elements with their major (a) and minor (b) axes aligned with one another, i.e. for the 2x1 and 1x2 geometries respectively. The frequencies at an infinite edge-to-edge separation denote those calculated for the corresponding modes of an isolated element. In panel (a), the curves corresponding to the acoustical and optical OE modes virtually overlay one another.

V.5 Discussion

Figure V.4-4 shows the dependence of the mode frequencies identified in Figure V.4-2 and Figure V.4-3 upon the edge-to-edge separation, and confirms the earlier observation that unlike the frequencies of AE collective modes, the OE and AB

collective modes appear to be nearly insensitive to their symmetry and to the variation of the edge-to-edge separation in the 2x1 geometry. The greater sensitivity of the frequency of the AE collective modes is explained by the smaller average distance between the precessing areas of the neighbouring elements as compared to the OE and AB collective modes. In contrast to the 2x1 geometry, the frequencies of all collective modes in the 1x2 geometry are shown to be sensitive to their symmetry and the variation of the edge-to-edge separation. One can also see, with the exception of the collective acoustical AB mode in the 1x2 geometry, that the frequencies of all the collective modes are greater than those of the corresponding modes of an isolated element.

Figure V.5-1 shows the simulated and analytical results for the dependence of the mode splitting resulting from the magneto-dipole interaction between elements upon the edge-to-edge separation. The analytical results are calculated by substituting numerically evaluated frequencies and profiles ($f(\mathbf{r})$ and $g(\mathbf{r})$) of the eigen modes of the isolated element as shown in Figure V.4-1. From simulations a maximum value of 2.13 GHz was found for the collective AE-type mode in the 2 x 1 geometry for an edge-to-edge separation of 5 nm. The simulated profiles of the 2 x 1 AE-type modes indicate that the magnetization precesses only near the neighbouring edges, leading to a stronger dynamic interaction. This interaction is significantly stronger than that between the edges of the same element leading to the difference between frequencies of the acoustical and optical modes of the isolated element of only 0.33 GHz. The size of the splitting in the 2x1 and 1x2 geometries remains comparable despite the difference in the average distance between precessing regions.

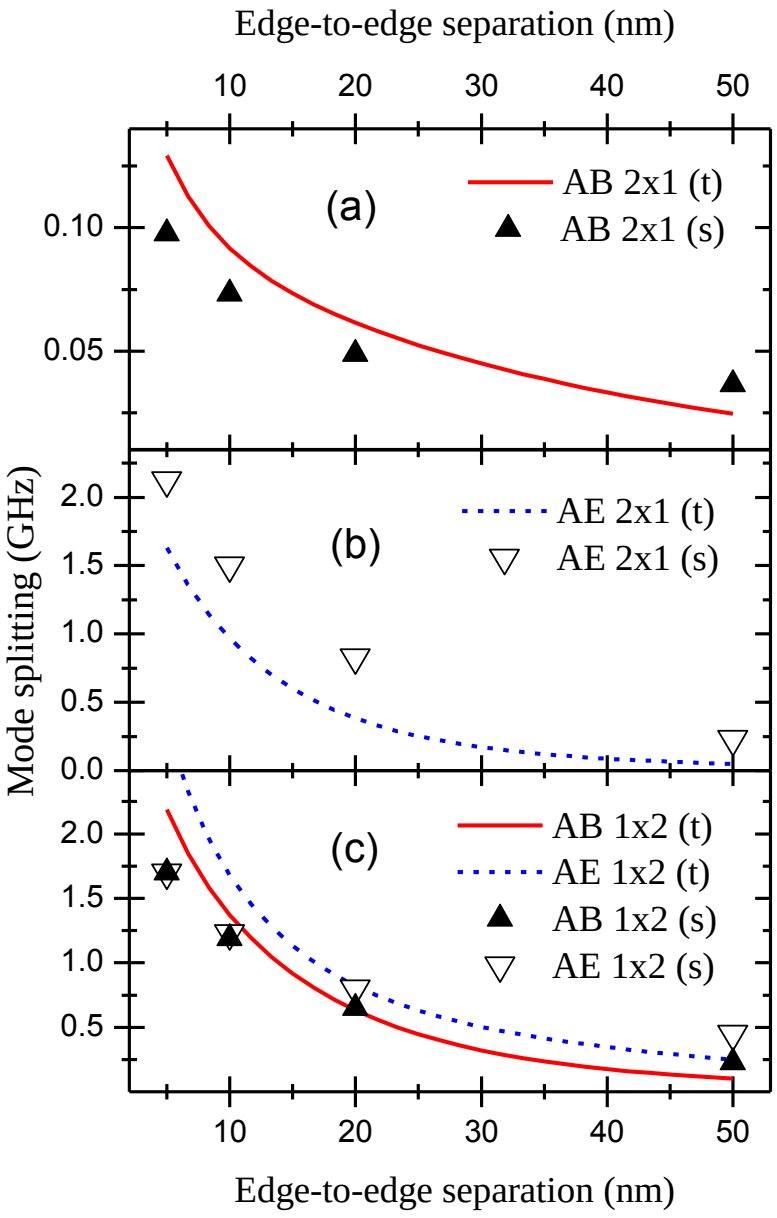

Figure V.5-1 The absolute values of the frequency splitting are plotted as a function of the edge-to-edge separation for the 2x1 (panels (a) and (b)) and 1x2 (panel (c)) geometries. The simulated and analytical curves are denoted "(s)" and "(t)" in the legend respectively.

The analytical theory describes the data well overall with the best agreement found for the bulk modes and then generally for the 1x2 geometry. This corresponds to the case when the modes preserve their character in individual elements despite the inter-element interaction, and hence to the case when the assumptions of the analytical

theory are most applicable. The analytical theory considers all mode profiles as rigid although the profile of the edge modes shows a great deal of flexibility when subject to dynamical magneto-dipole fields from neighbouring elements.

V.6 Conclusions

This chapter describes results of analytical and numerical calculations of collective spin wave modes in pairs of magnetic nano-elements. The difference in frequency of the symmetric (acoustical) and anti-symmetric (optical) modes as a measure of the strength of interaction between different elements has been investigated. For small edge-to-edge separations, the magneto-dipole interaction between neighbouring edges of the different elements can greatly exceed the combined magneto-dipole and exchange interaction between edges of the same element. The mode profile then becomes "soft" and differs substantially from that in isolated elements. The proposed perturbation theory, which uses the mode profile in an isolated element as an input and thus goes beyond the macrospin approximation, is adequate for the description of the mode splitting for medium and even small edge-to-edge separations provided that the mode profile remains "rigid".

VI Collective magnonic modes in finite sized 2D arrays of magnetic nano-elements

VI.1 Introduction

Several decades of investigations of spin waves (magnons)[24,46] in continuous and inhomogeneous magnetic media, isolated magnetic elements of different shapes and sizes and arrays of those have revealed both rich phenomenology[20,86,88,89,93,94,100-116] and important opportunities for technological applications[32,98,117-119]. As far as arrays of nano-elements are concerned, the spin wave theory has followed two main methodological approaches.

The early analyses either avoided or neglected the interaction between individual elements within arrays, so that conclusions were drawn from theories developed for isolated elements[86,103,118,120-125] Hence, within this approach the mode structure of an isolated constituent element was in the focus.

At high packing fractions, the magneto-dipolar coupling between elements within arrays could not be neglected anymore, leading to formation of collective normal modes of precession with a magnonic band spectrum[32,126-128]. Hence, at this extreme,

infinitely large arrays of magnetic elements were typically modelled, taking advantage of the Bloch theorem or periodic boundary conditions[86,89,107,93,111,113,126-133].

Micromagnetic simulations performed with specialized software packages (e.g. OOMMF or MicroMagus) have become an efficient, handy, and therefore widespread tool by which to model the spectrum of the observed spin wave modes[86,103,89,92,105,94,109,110,112,114,123,125] and, more recently, magnonic dispersion[134,135] and scattering parameters[10]. Due to limitations connected with the available computing power, the simulations were often performed for finite-sized (e.g. 3 x 3) arrays of magnetic nano-elements[89,92,94,112,123,136,137], with the expectation that the main features observed experimentally from much larger arrays would still be reproduced, at least qualitatively. The modification of the magnonic spectrum when elements are combined into larger but still finite arrays (or clusters of elements) has received independent attention only recently[138-140].

In this chapter, I present a systematic numerical study of collective magnonic modes in arrays composed of magnetic elements that are similar to those investigated in previous Chapter of this thesis.

VI.2 Micromagnetic simulations

In the simulations, we considered arrays of rectangular 100x50x10 nm^3 elements with rounded corners with the radius of curvature of 10 nm. The arrays consisted of N x N elements with N ranging from 2 to 11. In addition, the dispersion of collective spin waves was calculated for an array of 30 x 30 elements. The magnetic parameters were close to those of Permalloy (Py)[99], with the magnetic anisotropy neglected.

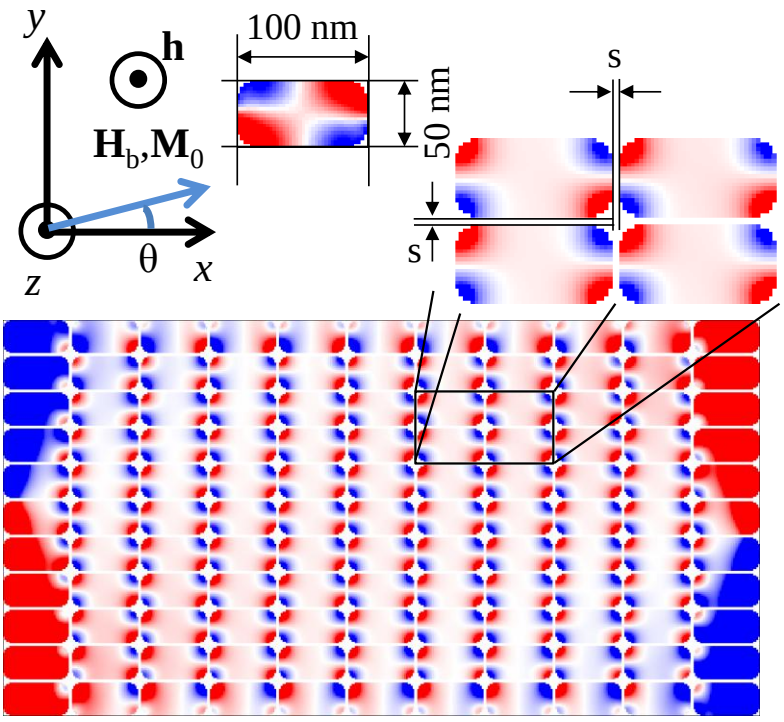

Figure VI.2-1 The static magnetic configuration and geometry used in the calculations.

To increase the spectral resolution, the damping constant was set to a reduced value of 10^{-4}. The discretization cell was 2.5 x 2.5 x 10 nm^3. The magnetic ground states of the samples were obtained by quasi-adiabatic relaxation from the perfect in-plane saturated state, first, at the field of 1300 Oe, and then, gradually (in 5 Oe steps) to the state at the bias field H_a of 200 Oe. The initial saturation and the applied fields were all parallel to the same in-plane direction, which was canted by 10° from the major axis of the element. Both the isolated nano-element and arrays of those favoured the ground state of the "flower" type (Figure VI.2-1). The details of the simulations and methods of their post-processing (e.g calculation of the spectrum and dispersion) can be found in Sections IV and V.

VI.3 Results of simulations

The mode spectrum of the isolated element excited by a uniform pulsed magnetic field could be found in Chapter V. Two dominant modes are observed. The lower and higher frequency spectral peaks correspond to the edge and bulk modes respectively, labelled here as "acoustic edge" (AE) and "acoustic bulk" (AB) modes, in agreement with our earlier studies [92,136,140]. However, in contrast e.g. to Ref. 92, the edge and bulk modes here have comparable amplitudes. In principle, by exciting the element with non-uniform (e.g. an anti-symmetric) pulsed fields, anti-symmetric modes (e.g. so called "optical edge" (OE) and "optical bulk" (OB) modes) could also be observed, as discussed in previous Chapter.

In Section V, we have studied in detail how the modes of the isolated element give rise to collective normal modes of a closely spaced pair of such elements. In an array (cluster) of elements, the number of collective modes deriving from each mode of the isolated element is generally equal to the number of coupled elements within the array (cluster). Hence, the complexity of the collective spectrum of the arrays rapidly increases with their size. At the same time, the separation between neighbouring spectral peaks decreases. To resolve the peaks, the simulated time has to be increased, while the damping constant has to be reduced, with the latter also impacting the stability and thereby speed of the calculations. With these considerations in mind, a series of simulations for arrays of 11x11 elements with different edge-to-edge separations was run first, so that the strength of the magneto-dipole coupling between elements could be optimized so as to facilitate analysis of the character of the collective magnonic modes. The resulting spectra are shown in Figure VI.3-1(a). The edge-to-edge separation of 5 nm was chosen for further analyses unless stated otherwise.

Some important observations can be made already from Figure VI.3-1. The spectra are dominated by two collective magnonic bands originating from the two modes of the isolated element. The bands consist of discrete peaks corresponding to standing collective spin waves confined within the arrays of finite size. The “bands” originating from the AE and AB modes of the isolated element behave differently as the edge-to-edge separation decreases, which can be interpreted in terms of the nonuniformity of the stray magnetic field created by elements within the array (Figure VI.3-1(b) and (c)).

At the edges of a particular element (i.e. in the region of localization of the AE mode), the stray dipolar field from the neighbours is dominated by that from the magnetic charges at the nearest “external” edge, i.e. the one located just across the edge-to-edge gap (Figure VI.3-1(b)). The stray field is antiparallel to the self-demagnetizing field from the own edge magnetic charges of the element itself. Hence, as the edge-to-edge separation decreases, the total magnetic field in the edge region increases, and the frequency of the collective AE modes therefore also increases.

In contrast, the frequencies of the AB collective modes decrease as the edge-to-edge separation decreases. Hence, for this mode, the stray field from the neighbours adds to the self-demagnetizing field of each particular element and works against the applied magnetic field (Figure VI.3-1(c)). This is a result of the smaller centre-to-centre distance between elements in the direction perpendicular to their long axis, and hence, a greater contribution to the stray magnetic field from the neighbours facing the element with their long edges.

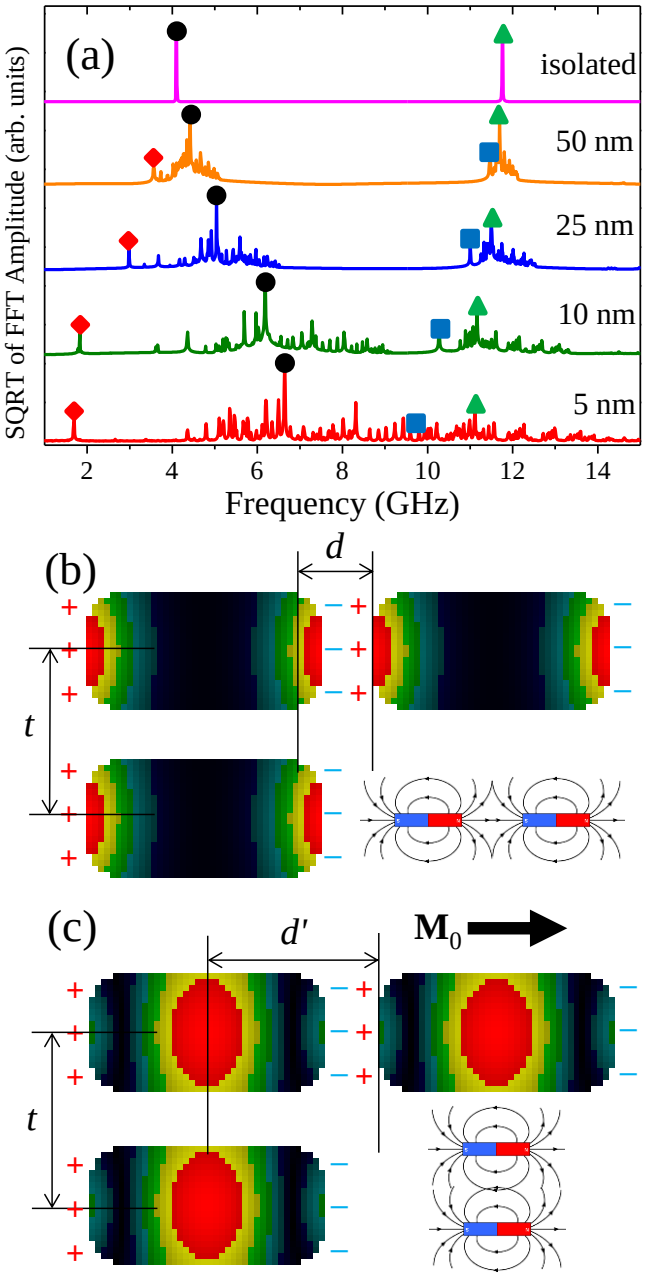

Figure VI.3-1 (a) The spectra of the 11x11 array are shown for different values of the edge-to-edge separation between the elements. The different symbols follow evolution of the lowest order ("fundamental") modes of the same character within individual elements. (b) and (c) The characteristic distances determining the frequency shift of the collective modes are schematically shown for the acoustic edge (b) and acoustic bulk (c) modes together with schematics of the stray magnetic field.

The width of both the AE and AB bands increases as the edge-to-edge separation decreases. Hence, the dynamic dipolar coupling between the elements increases for both mode types, as expected. To study the anisotropy of the coupling, we have calculated the dispersion of the collective spin waves for an array of 30x30 elements (Figure VII.3-3). A positive dispersion is observed for the "transverse direction", i.e. direction perpendicular to the major axis of the array (Figure VI.3-2, top left panel), which corresponds to the so called the Damon-Eshbach geometry (the magnonic wave vector is perpendicular to the static magnetization). At the same time, the direction parallel to the major axis of the array ("longitudinal direction") is characterized by a negative dispersion across the whole bands (Figure VI.3-2, top right panel), which corresponds to the so called backward-volume geometry (the magnonic wave vector is parallel to the static magnetization). The anisotropy of the dispersion is associated with the strong anisotropy of the dynamic magneto-dipole coupling[92,94]. The width of the magnonic bands is greater for the magnonic wave vector perpendicular to the static magnetization, indicating a stronger dispersion and hence a stronger dynamic coupling between elements facing each other with their longer edges.

Three dominant dispersive bands are observed for the transverse direction. The two higher frequency bands originate from the AE and AB modes of the isolated element. The lowest frequency band originates from the OE mode of the isolated element, where it not expected to be excited by the uniform pulsed field. So, the excitation of such modes observed here should be attributed to the effect of interaction within the system of closely packed magnetic elements. The modes are however beyond the scope of this thesis and will be addressed elsewhere.

The longitudinal direction reveals several magnonic bands, differentiated not only by the different spatial characters of the originating modes of the isolated element

but also by different values of the transverse component of the magnonic wave vector. The latter effect is barely visible in the transverse direction due to the weaker dispersion in the longitudinal direction.

The widths of the AE and AB magnonic bands for the transverse direction are similar. The observation indicates that the dynamic dipolar coupling in this direction is similar for the modes, i.e. the dynamic stray fields generated by the modes have similar symmetries and strengths. This is consistent with the effective distance between the regions of localization of the modes in the transverse direction being equal in both cases.

The situation is different for the longitudinal direction for which the widths of the AE magnonic bands are greater than those of the AB bands. Hence, the corresponding dynamic coupling for the edge mode is greater than that for the bulk mode, as was shown in Ref. 140 for pairs of elements and now generalized to the case of 2D arrays.

In addition to the dispersive bands, horizontal bands are observed in Figure VI.3-2. The bands are due to modes localized near the boundaries of the array as a whole. Due to the static magnetic charges at the boundaries, the internal field in their vicinity is reduced as compared to that in the interior of the array. So, the mode frequencies tend to be smaller than those observed within the dispersive magnonic bands. The relative contribution of the localized modes to the dynamic response of arrays to uniform excitation increases as the number of elements in the array decreases. This effect is similar to that observed in Ref. 136 for individual elements to lead to the crossover to non-uniform precession upon reduction of the element size.

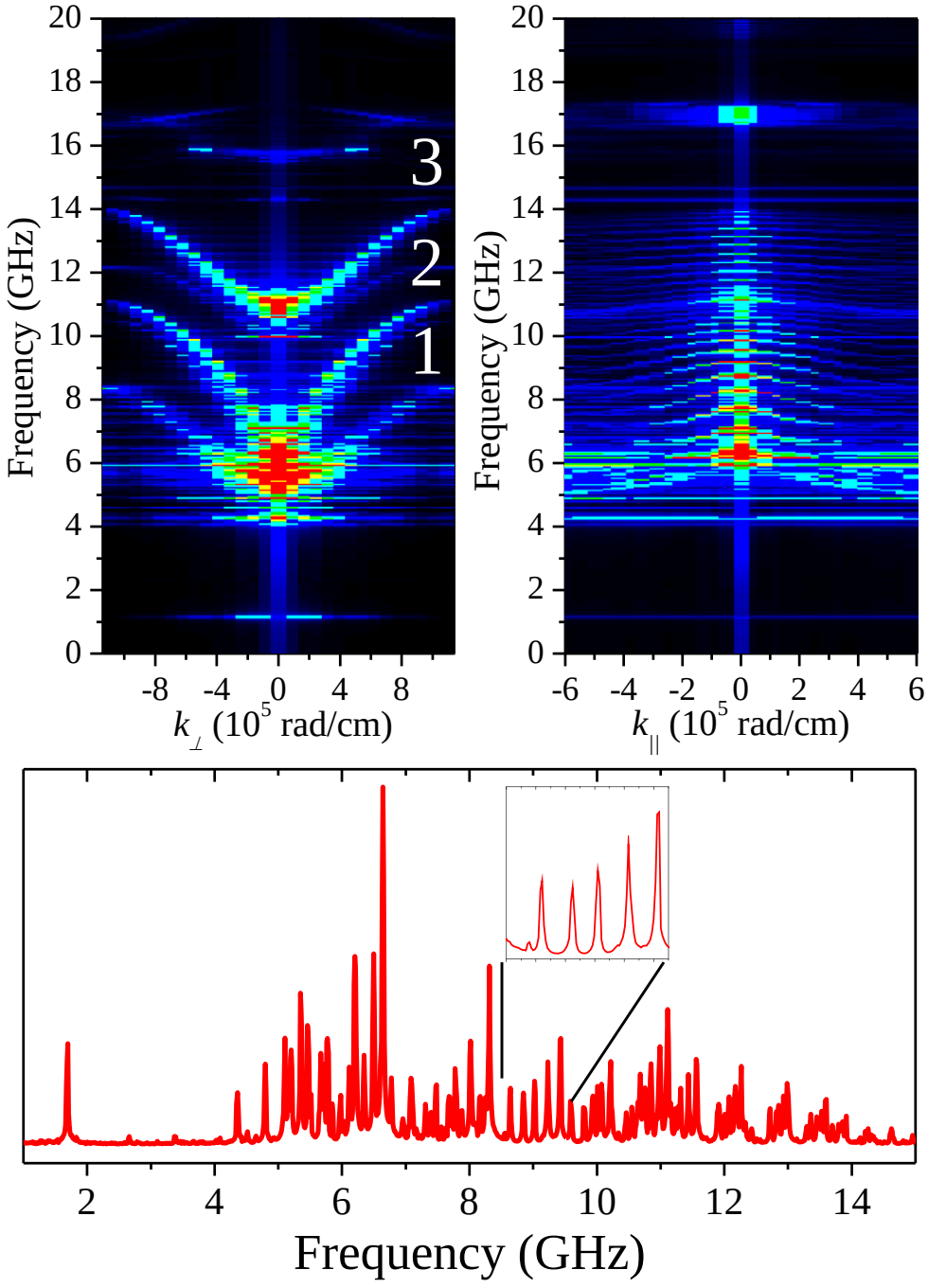

Figure VI.3-2 The dispersion and spectrum of spin waves in a 30x30 array of magnetic nano-elements is shown for the first Brillouin zone. The top left and right panels show the dispersion of the spin waves propagating along the transverse and longitudinal directions respectively. The bottom panel shows the spectrum corresponding to the dispersion shown in the top panels. The inset magnifies a portion of the spectrum.

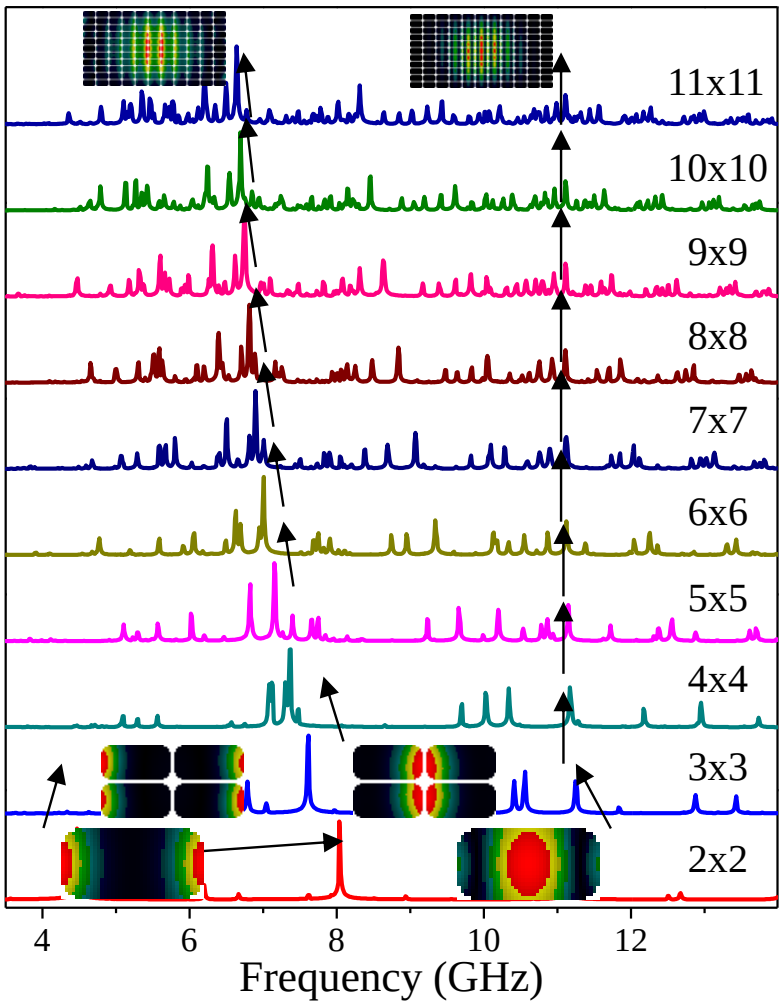

Figure VI.3-3 The spectra of spin waves excited in *N*x*N* arrays of elements are shown for *N* increasing from 2 (bottom curve) to 11 (top curve). The symbols mark peaks corresponding to fundamental modes of the same character within individual elements. The insets show the spatial profiles of the amplitude of modes corresponding to spectral peaks marked by arrows.

The bottom panel of Figure VI.3-2 shows the spectrum corresponding to the dispersion shown in the top panels. We observe several groups of peaks. The average peak height for the different groups decreases as their average frequency increases. Let us note now that the peak heights are expected to scale inversely with the order of the corresponding modes. Indeed, higher order modes have a greater number of nodal lines.

Hence, the corresponding net dynamic magnetization is smaller (for the same mode amplitude) for higher order modes. Moreover, the reduced average dynamic magnetization of the higher modes results in a weaker coupling to the uniform excitation. Hence, we can conclude that the groups follow the positive dispersion, and taking into account the top panels of Figure VI.3-2, they correspond to the different quantization orders in the transverse direction (top left panel).

However, within each group, the peak height increases (and hence the order decreases) as the frequency increases. This corresponds to the negative dispersion and hence quantization in the longitudinal direction (top right panel). The groups can be distinctly observed in the present case due to the different dispersion strengths for the transverse and longitudinal directions, as was noted earlier.

Figure VI.3-3 shows mode spectra calculated for NxN arrays with N ranging from 2 to 11. The spectra of an isolated element and a 2x2 array of such elements differ drastically. In particular, the spectrum of the 2x2 array has three dominant modes. The spatial profiles of their Fourier amplitudes reveal that the lowest frequency mode (not observed in the isolated element) is an edge type mode localized near the lateral boundaries of the array. At the same time, the mode cannot be ascribed to the AE type, which is consistent with the softness of edge modes observed in pairs of such elements[140]. The higher frequency modes should be classified as "de-localized" collective modes, with the edge mode again showing remarkable softness. We do not observe such splitting into de-localized mode and that localized near the array boundaries for the AB mode of the isolated elements. This could be understood by taking into account its high frequency and the "rigidity" of its spatial profile[140].

The spectra shown in Figure VI.3-4 reveal that the frequency of the fundamental mode of the AB character is nearly independent of the number of elements

within the arrays. The only significant change is observed when the number of elements increases from 1 to 2x2. This might suggest that, even despite the long range nature of the magneto-dipole interaction, the nearest neighbours provide the dominant contribution to the frequency of the fundamental AB mode, while the dipolar fields created by elements in each of the more distant coordination spheres (or rather "coordination circles") tend to cancel. However, this interpretation would ignore the collective character of the mode. Instead, we suggest that the observed immunity of the fundamental AB mode to the number of elements in the arrays is explained by the preserved in-plane aspect ratio of the NxN arrays with different values of N.

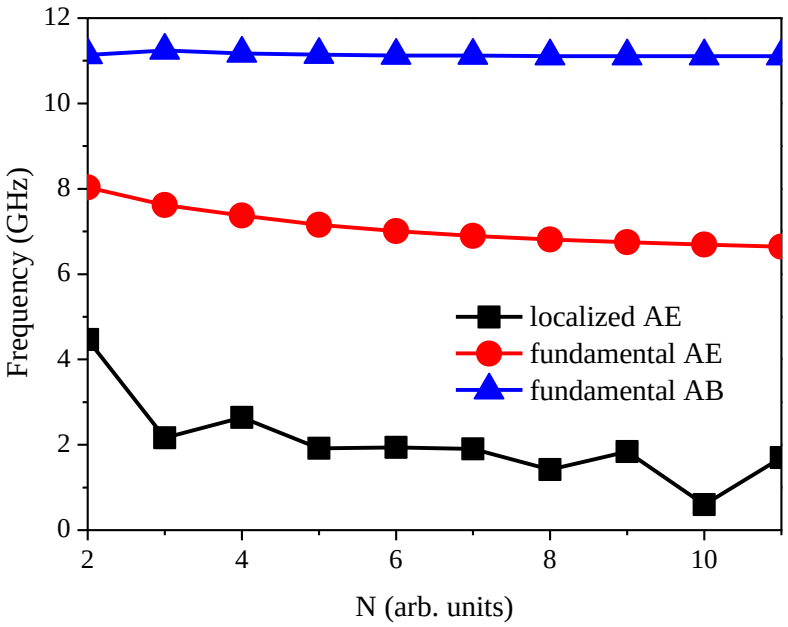

Figure VI.3-4 The frequencies of the dominant magnonic modes are shown as a function of the number of elements within the array.

As opposed to the fundamental AB mode, the frequency of the fundamental mode of the AE character decreases as the number of elements of the array increases. We attribute the observation to the strong confinement of the AE mode near the element edges. As a result of the confinement, the precession within each "bi-column" of edges (two columns of edges separated by the gap) is sensitive mostly to its own effective in-

plane aspect ratio. Hence, the precession frequency behaves (at least to some degree) as that of a rod magnetized perpendicular to its length. As the size of the array increases, the length of such a "rod" also increases, and the precession frequency therefore decreases. At even larger array sizes, the field from more distant columns of edges ("rods") becomes more significant, and the in-plane aspect ratio of the whole array becomes the dominant factor. Eventually, we observe that the dependence of the frequency of the fundamental AE mode upon the number of elements in the array saturates.

The frequencies of higher-order modes of the AB and AE character both show a similarly strong dependence upon the number of elements in the arrays. This can be easily understood taking into account that the collective modes of the same order are actually characterized by different values of the collective wave number in arrays of different sizes. In addition, the non-uniformity of the internal magnetic field in the arrays as a whole begins to contribute to the frequency and character of modes with significant amplitude near the outer array boundaries that are perpendicular to the applied magnetic field.

Similarly to the case of continuous magnetic elements[89,92], we observed modes of the AE character localized near the outer array boundaries that are perpendicular to the applied magnetic field. The frequency of such modes depends non-monotonically on the number of elements within the array. In particular, when the number of elements is smaller than *5 x 5*, the frequencies of the localized modes in arrays with even number of elements in the column are greater than those in arrays with odd numbers of elements. Then, the dependence has a *plateau.* Finally, when the number of elements becomes greater than 8 x 8, an opposite dependence is observed as the frequencies of the localized modes in "odd" arrays become greater than those in "even" arrays.

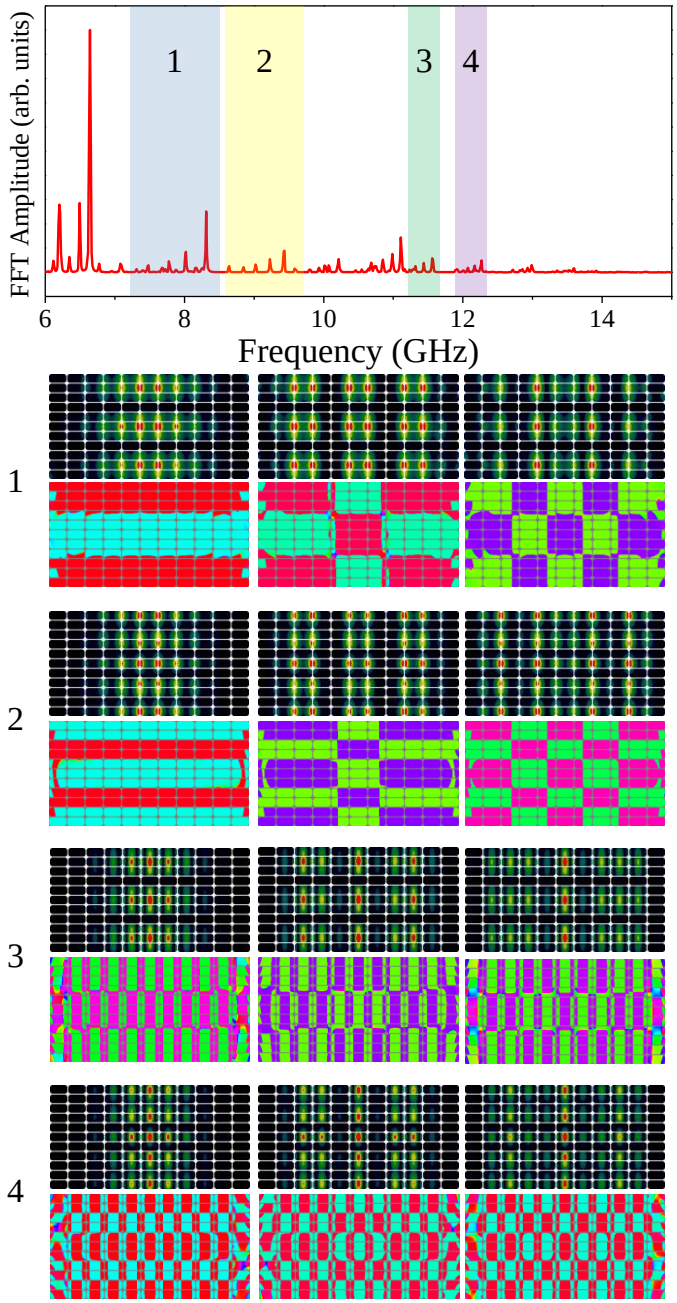

Figure VI.3-5 The spectrum of spin waves excited in the arrays of 11x11 elements is shown for the case of the spatially uniform excitation together with the corresponding modes profiles. The mode profiles organized as follows: the top and bottom images in each pair represent spatial profiles of the FFT amplitude and phase, respectively. The top pairs of images in each group correspond to the Γ-point of the Brillouin zone where the frequency is highest for the group.

To shed some light onto the behaviour, we have analysed the spatial profiles of the localized AE modes in the different arrays. We find that the modes are mainly localized in four boundary elements of the arrays (two elements at each side). The magnetization in the elements is affected most by the ground magnetic states of the arrays as a whole. Hence, we believe that the frequency of the modes is determined by the details of the symmetry of the ground magnetic state of the array and of the associated landscape of the internal static and dynamic magnetic fields.

VI.4 Discussion

We begin the discussion by noting that, similar to the case of pairs of elements considered in Ref. 140, the AE modes do not preserve their spatial character within individual elements. Indeed, the spatial profiles of the collective AE modes shown in Figure VI.3-5 reveal that, for the AE modes, the "collective" nodal lines that are perpendicular to the major axis of the array can cross the elements. This contradicts the common assumption that such arrays of strongly interacting magnetic elements could be considered as arrays of "rigid" oscillators.

In the present case of closely packed elements, the interaction between the neighbouring elements is strong. Hence, it is plausible that the interaction might overcome the energy of a particular AE mode of the individual element. In this case, it could be more appropriate to consider the AE mode of an individual element as two modes localized at its opposite edges (see Section V). The dynamical interaction between the two edge modes is weak. Hence, when the elements are combined into closely packed arrays, the nearest edge regions of neighbouring elements might form (at some frequencies) more "rigid" entities than the individual elements themselves. The corresponding collective modes of the array could then be considered as those deriving from these new entities rather than the AE modes of the isolated elements. Nonetheless,

for the sake of simplicity of notations, we will continue referring to the modes as of the AE type.

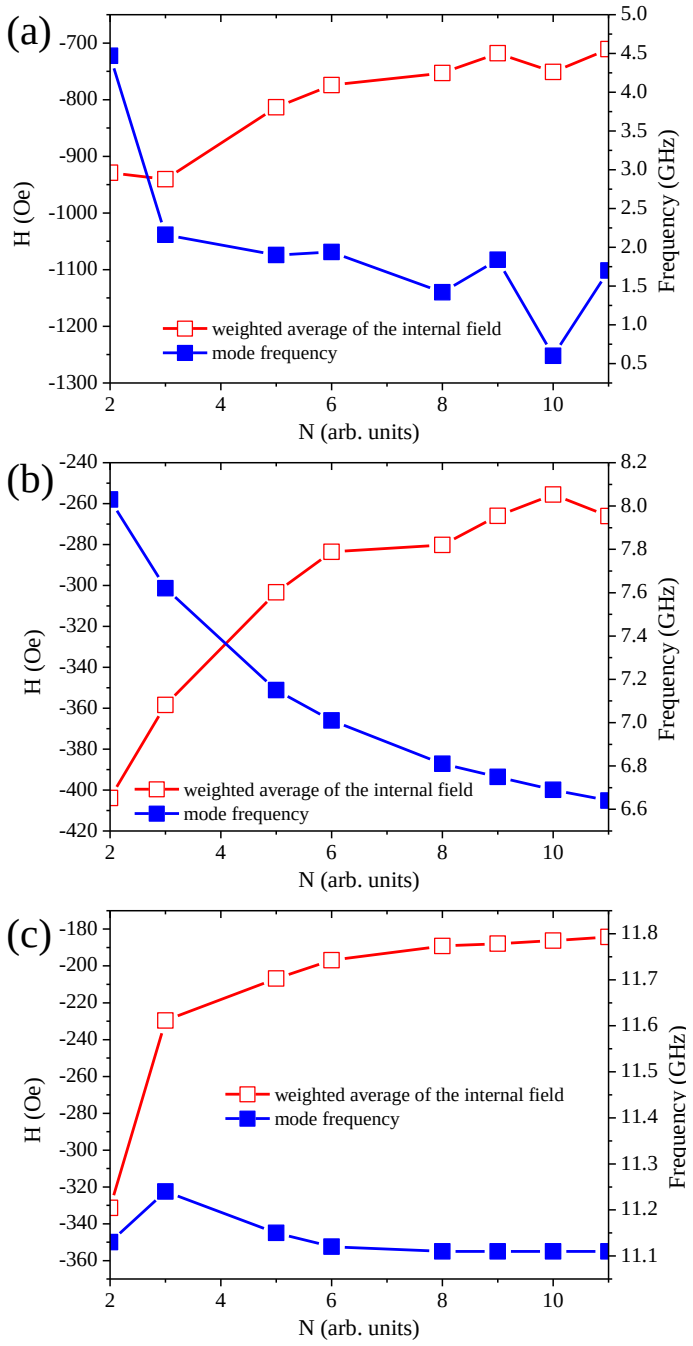

Figure VI.4-1 The average value of the superposition of the static applied and demagnetizing fields is shown for (a) the localized AE modes, (b) the fundamental AE modes, and (c) fundamental AB modes.

Further inspection of the mode images showed that the AE mode of the isolated element has a rigid profile along the transverse direction, in contrast to the longitudinal one. The AB mode of the isolated element is found to be rigid along both transverse and longitudinal directions. In other words, the spatial profile of the AB is preserved in the collective modes of the arrays.

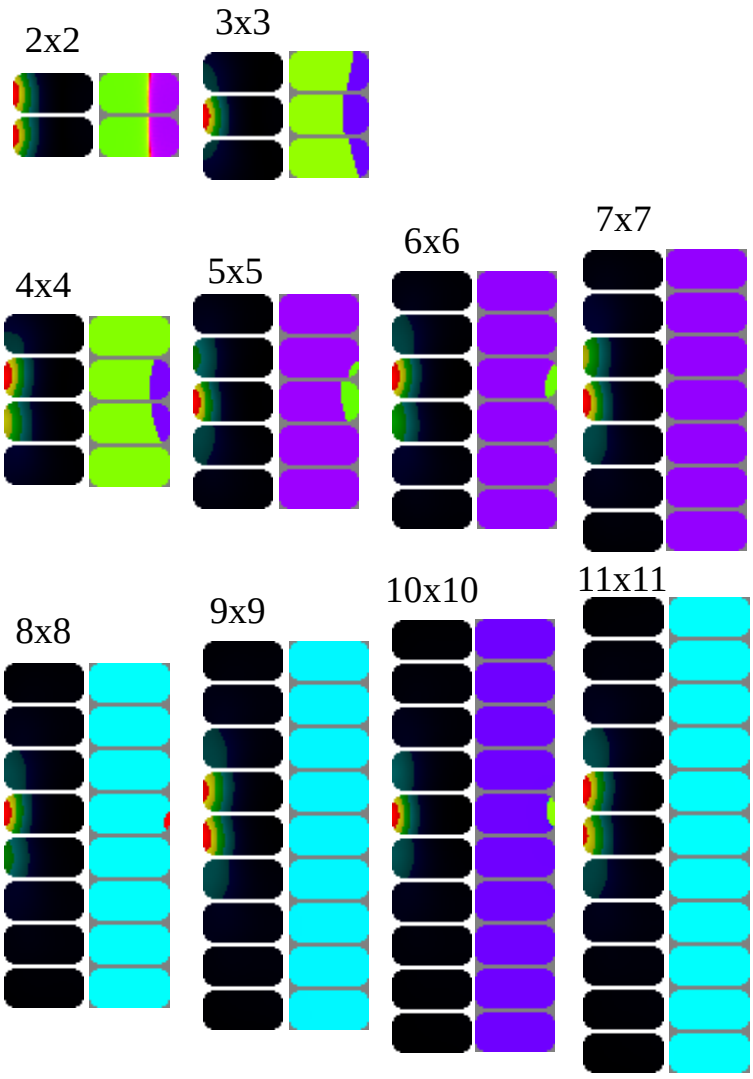

Figure VI.4-2 The spatial profiles of the Fourier amplitude (left) and phase (right) of the localized AE modes are shown for arrays with number of elements ranging from *2x2* to *11x11*. The modes are strongly localized in the edge columns of the arrays, and so, the edge columns are shown.

To gain a quantitative understanding of the observed mode frequencies, it is common to calculate the average values of the static internal field over the areas of the mode localization. The underlying assumption is that the mode frequency should scale with the average field value. The approach is widely adopted in literature for the explanation of frequencies of various localized modes in both isolated elements[123] and arrays of anti-dots[141]. Here, we present a version of the method refined to facilitate the evaluation of the average value of the internal field separately for each particular mode.

Let us assume that the spatial distribution of the mode is given by its Fourier amplitude m_i, where i refers to the different cells of the mesh used in the simulations. The spatial profile is normalized so that $\sum_i m_i = 1$. Then, the average field is calculated as $\langle H \rangle = \frac{\sum_i \mathbf{H}_i \mathbf{M}_i}{M_S}$ where the summation is performed over all cells in the micromagnetic model and H_i and M_i are internal field and magnetisation vector of ground state, respectively. In the present study, we have used the method to calculate the average values of the sum of the applied and demagnetizing fields.

We have calculated the average values of the static fields for the fundamental and localized AE modes and the fundamental AB mode. The results of the calculations are shown in Figure VI.4-1. For each mode type, the average value of the field increases with the number of elements in the array. The increase should be accompanied by an increase of the mode frequencies. However, the opposite trend is observed. On the positive side, Figure VI.4-1(a) shows some correlation between the characters of variation of the field and frequency for the localized AE mode. In particular, when the number of elements in the array is greater than 7x7, the average field of odd arrays is enhanced as compared to even arrays. Even though the value of the enhancement is quite small, the observation confirms that the average value of the field is sensitive to the parity of the arrays, at least in the regions of localization of the AE modes. Due to

the demonstrated failure of the static internal field to explain the observed variation of the mode frequencies with the number of elements in the arrays, we have to conclude that the variation is dominated by the dynamical interaction.

The spatial profiles of the localized AE modes are presented in Figure VI.4-2. The images reveal that, depending on the parity of the array, the modes are localized mainly in one or two elements of the edge column. In particular, when the number of elements is smaller than 5x5, the modes occupy two edge elements of even arrays, while in odd arrays only a single element is occupied. When the number of elements ranges from 5x5 to 7x7, a single element is occupied in both even and odd arrays. Finally, if the number of elements is greater than 7x7, the modes mainly occupy two elements and one element in odd or even arrays, respectively. So, we conclude that, if the localized mode mainly occupies one element, then the contribution of the dynamical interaction is reduced. In contrast, if the mode is localized in two elements, the effect of the dynamic magneto-dipole coupling is enhanced.

The spatial profiles of the localized modes suggest that they are formed by the eigen mode(-s) of the individual element(-s) that are localized only in the single edge region of the element(-s), and so, we can call them single edge (SE) modes. The modes have not been resolved in the simulations of the isolated element. In contrast to the AE and AB modes, the side-by-side interaction of the SE modes of the same phase increases the frequency of the collective mode, explaining the observed non-monotonic dependence of the frequency upon the number of elements in the arrays. A similar effect has been observed in Section V in a form of AE modes with abnormal dispersion. Here, the variation is enhanced even further due to the specific non-monotonic dependence of the average internal field upon the number of elements in the arrays identified earlier.

Thus, one can say that the ground magnetic state and the associated profile of the static magnetic field have a dual effect upon the dynamics of the localized modes. Firstly, the average value of the field affects the frequencies of the modes directly, and secondly, the profile of the field determines the strength of the contribution of the dynamic magneto-dipole interaction to the mode frequencies.

VI.5 Conclusions

In summary, I have showed that the dynamic response of the array is dominated by the delocalized collective magnonic modes. It has been found that static dipolar interaction play different roles for the modes of different spatial profiles. Moreover, it has been found that 2D arrays of closely packed magnetic elements show strong anisotropy of the dynamic dipolar coupling. In particular, the dynamic interaction along the column of the array is by an order of magnitude stronger than that along the rows. Finally, it has been found that the dynamics of the strongly localized modes of the edge character is strongly affected by the symmetry of the ground state of the system. In particular, arrays having odd or even number of elements along the columns show different frequencies of the localized modes of the edge character. In principle, the conclusions of this study are verifiable experimentally by the time resolved scanning Kerr microscopy (TRSKM)[92] or Micro-focus Brillouin Light Scattering (μBLS)[116].

VII Localized magnon states in finite stacks of magnetic nanoelements

VII.1 Introduction

The recent renaissance of interest in magnonic crystals[127] – media with periodic modulation of magnetic parameters – has led to several important advances in the understanding of propagation, confinement, and quantization of spin waves[24] in magnetostatically coupled 1D[130] and 2D[20,86,88] arrays of magnetic elements as well as 2D arrays of antidots (holes in otherwise continuous films)[142]. In contrast to the numerous studies of spin waves confined in continuous nano- and micro-scale magnetic elements [143,85,123,144,145], magnonics[146] has emerged as a field aiming at investigation of propagating spin waves in nano-structured magnetic samples, with a promise of re-programmable magneto-electronic devices[32,98,147].

The outlined progress is however in striking contrast to studies of nano- and micro-scale magnetic elements in three dimensions (3D). Experimentally, the situation is due to the lack of adequate techniques[32]. On the other hand, numerical micromagnetic modeling[134,135,140] is limited by available computing power. The analytical theory has shown most progress so far[129,148], yet with only the simplest models addressed.

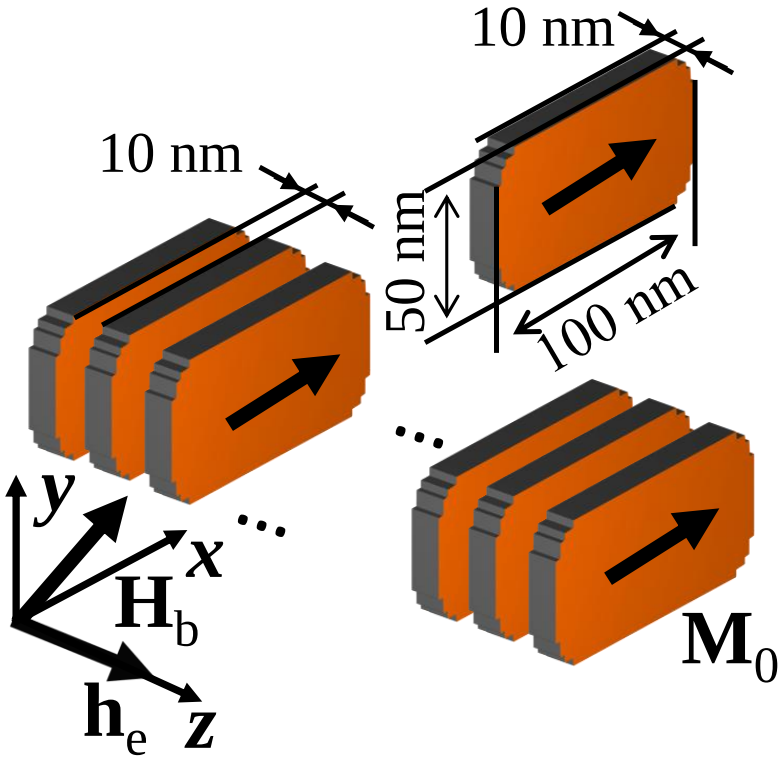

Figure VII.1-1 The geometry of the problem is schematically shown. The inset shows the coordinate system used in the calculations together with the orientations of the bias and excitation magnetic fields.

In this Chapter, I present a numerical study of collective magnonic modes in stacks of thin magnetic nanoelements. The spectrum, dispersion, and spatial character of magnonic modes are extracted from simulations performed using OOMMF and thoroughly analysed. The calculations reveal that the sign of the dispersion within magnonic bands is determined by the spatial character and ellipticity of the modes of the isolated element that give rise to the bands. In particular, we find that, in our sample, the magnonic bands originating from the edge and quasi-uniform delocalized (fundamental) modes have negative dispersion, while the higher order delocalized modes give rise to bands with positive dispersion. Moreover, we have identified a critical value of the ellipticity at which the magnonic dispersion changes its sign. I demonstrate that the critical value of the ellipticity is defined by the properties of the

magneto-dipolar interaction. Furthermore, the finite width of the magnonic bands governs the localization of magnonic modes near regions of increased internal magnetic field, complementing the earlier discovery of mode confinement within so called spin wave wells[144].

VII.2 Simulations setup

The simulations were performed for stacks of 60 and 240 elements formed by rectangular Lx50x10 nm^3 elements (see Figure VII.1-1) with rounded corners, with the radius of curvature of 10 nm and length L ranging from 30 to 200 nm. The element-to-element separation is 10 nm. The magnetic parameters are close to those of Py[99], with the magnetic anisotropy neglected and the value of the Gilbert damping constant reduced to 10^{-4}. The discretization cell was set to 2.5x2.5x10 nm^3, i.e. each element was one cell thick. The magnetic ground states of the samples were prepared by quasi-adiabatic relaxation from the perfect saturation tilted in-plane by 10^o from the x axis, first, at the field of 3000 Oe, and then in 10 Oe steps, to the state at the bias field H_b of 1500 Oe.

In the dynamical simulations, the samples were excited by a small broadband magnetic field, localized in the center of the stack and directed along the z axis and uniform in the (x,y) plane. Dynamical states $\mathbf{M}(\mathbf{r},t)$ were recorded every 10 ps within the first 80 ns of each simulation and used to calculate cell-wise Fourier spectra with the DFT. The frequencies of individual modes were extracted by fitting peaks in the sum of DFT amplitude spectra from all cells of the sample to the Lorentzian function. The spatial profiles of the amplitude and phase of individual modes at fitted frequencies were then re-constructed from the cell-wise DFT data.

To calculate the dispersion of spin waves in the 3D samples studied here, we have extended the method developed for 1D case in Refs. 134 and 135. The results were visualized by applying the 4D DFT to the entire simulated (in the real space and time) data set, and then summing the obtained Fourier amplitudes in the reciprocal space over the (k_x,k_y) plane for each value of k_z. The 2D representation of the spin wave dispersion obtained in this way contained contributions from both symmetric and anti-symmetric modes.

VII.3 Results and discussion

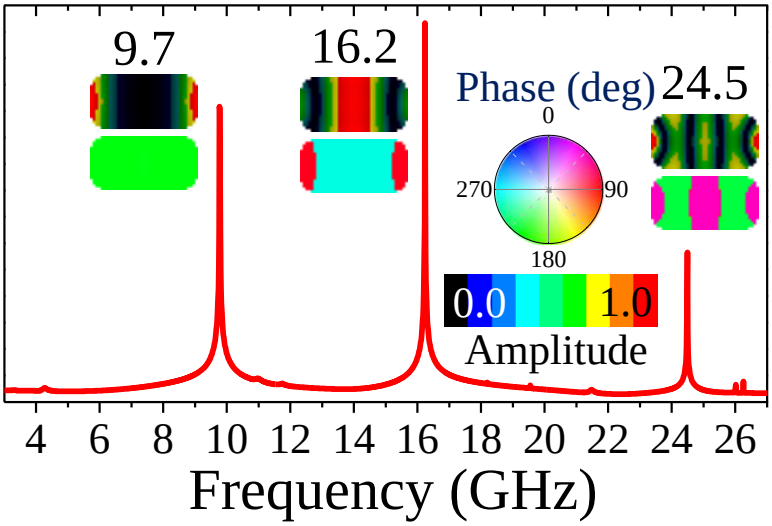

Figure VII.3-1 The mode spectrum of the isolated 100x50x10 nm^3 element is shown. For each mode, the top and bottom images represent the spatial distributions of the DFT amplitude and phase respectively, while the numbers are the frequencies in GHz.

Figure VII.3-1 shows a typical spectrum of spin waves excited in the isolated 100x50x10 nm^3 element, with 3 dominant modes observed in the frequency range of 30 GHz. The two lowest frequency modes are the "edge" and "bulk" modes respectively, discussed e.g. in Ref. 140. The highest frequency mode shown is a higher order "bulk" mode, with further higher order modes observed beyond the shown frequency range.

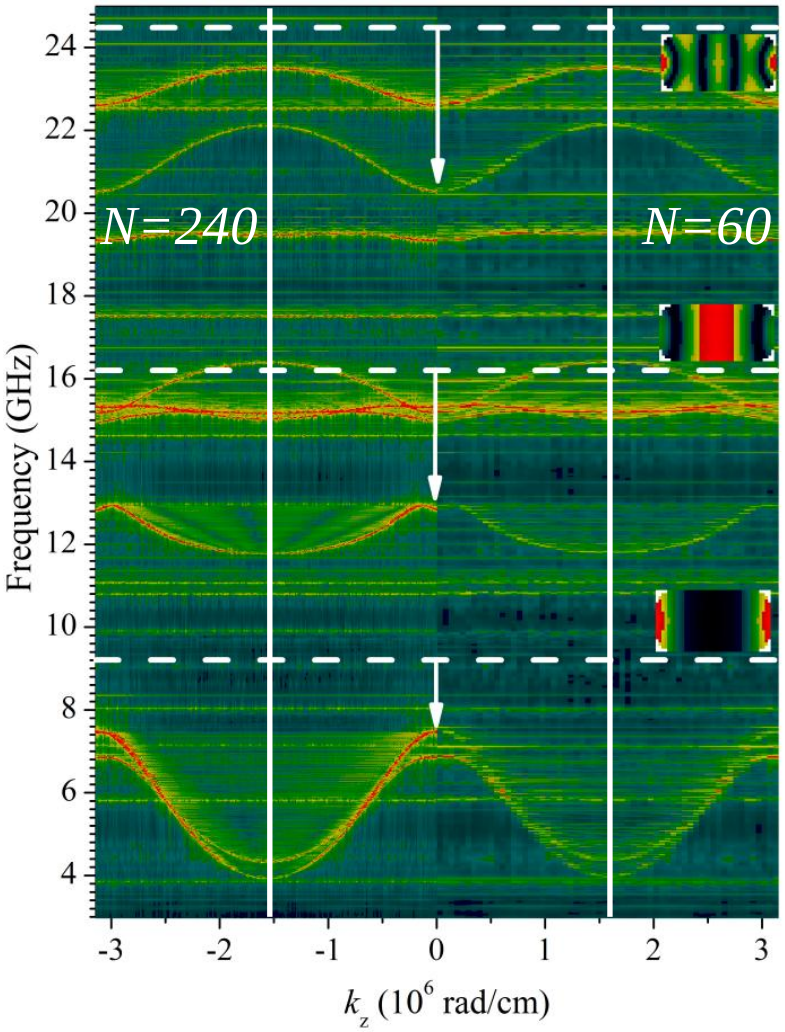

Figure VII.3-2 The magnonic dispersion is shown for stacks of 240 (left half) and 60 (right half) elements with dimensions of 100x50x10 nm^3. The insets show the spatial profiles of the modes of the isolated element, while the dashed lines represent their frequencies. The arrows point to the magnonic bands formed from the modes of the isolated element. The solid vertical lines show the boundaries of the Brillouin zone.

The positive dispersion of the modes is determined by the dominant effect of the exchange interaction. For the edge mode, the ellipticity of precession is very small ($m_z/m_y << 1$, where m_z and m_y are components of the dynamic magnetization). For the fundamental bulk mode, dynamics is still dominated by the in-plane component

($m_z/m_y \approx 0.5$). Finally, for the higher order bulk mode, the out- and in-plane components of the dynamic magnetization are of the same order of magnitude ($m_z/m_y \approx 1$).

In stacks, the magneto-dipolar coupling between elements splits modes of the isolated element into bands of collective magnonic modes (Figure VII.3-2). The frequencies of the collective modes in the centre of the Brillouin zone (Figure VII.3-2) are generally lower than those of the corresponding modes of the isolated element (Figure VII.3-1). This can be attributed to the effect of the static stray magneto-dipole field from the neighbours, since the field adds to the own demagnetizing field of each element. There are dispersive magnonic bands, which are characterized by different signs of dispersion, and also some dispersionless modes, which are represented by the horizontal lines. The intensity of the dispersionless modes is generally lower than that of the dispersive ones. This is due to the weaker coupling of the dispersionless modes to the local excitation, which can be explained by their reduced amplitude in the centre of the stack.

Two dispersion branches are observed for the lowest standing mode corresponding to the edge mode of the isolated element (Figure VII.3-1). The spatial profiles of the modes in the planes of individual elements reveal that the dispersion branches starting from the higher and lower frequencies originate from the symmetric and antisymmetric edge modes of the isolated element respectively. The width of the band originating from the symmetric edge mode is greater than that of the antisymmetric edge modes, indicating that the stray field coupling for the antisymmetric edge modes is somewhat weaker than that for the symmetric edge modes.

For the edge and fundamental bulk modes, the collective modes at the boundaries of the Brillouin zone have frequencies that are smaller than those of modes

in the centre of the Brillouin zone, i.e. a red shift (negative dispersion) is observed. At the same time, a blue shift (positive dispersion) is observed for the higher order bulk modes. We therefore observe either negative or positive dispersion depending on the mode profile within individual elements.

To interpret the observation, let us consider a chain of magnetostatically coupled magnetic moments (spins). In a chain magnetized parallel (perpendicular) to its length, the static stray magnetic field from the neighbours is approximately parallel (antiparallel) to the static orientation of individual spins, thereby increasing (decreasing) the frequency of their precession for both uniform and non-uniform collective modes. In contrast, the effect of the dynamic stray field depends on the relative phase of precession of the neighbouring spins and is therefore different for uniform (in the centre of the Brillouin zone) and non-uniform (e. g. at the boundaries of the Brillouin zone) precession.

In the present study case of magnetization perpendicular to the length of the chain, the dynamic magnetic moment has two components – one parallel and one perpendicular to the chain. For the case of in-phase (out-of-phase) precession for the modes in the centre (near the boundaries) of the Brillouin zone, the stray field due to the component of the neighbour's dynamic magnetic moment *parallel* to the chain is parallel (antiparallel) to the dynamic magnetic moment of individual elements, thereby decreasing (increasing) the frequency of their precession via decreasing (increasing) the "restoring force" acting upon the spins. In contrast, the effect of the stray field due to the component of the neighbour's dynamic magnetic moment *perpendicular* to the chain is exactly opposite.

So, the interaction due to the dynamic magnetic moments parallel and perpendicular to the chain leads to positive and negative contributions to the dispersion

respectively. The resulting dispersion of the collective modes of the chain is therefore determined by the relative strength of the two opposite effects that is in turn determined by the *ellipticity* of precession.

So, for the edge and fundamental bulk mode, the ellipticity is small, and their precession is dominated by the dynamic magnetization perpendicular to the direction of stacking, leading to the observed negative dispersion. The ellipticity is more significant for the bulk mode, leading to its weaker dispersion. In contrast, the trajectory of precession of the higher order bulk modes is almost circular with a significant component parallel to the direction of stacking, leading to their observed positive dispersion. The strength of dispersion varies depending on the exact mode profile, which could in principle be addressed by a quantitative simultaneous account of both the ellipticity, amplitude and phase profiles of the modes as described in Ref. 140. This is however beyond the scope of the present study.

To quantify the effect of ellipticity on the dispersion of the collective magnonic modes, we performed additional simulations in which the size of the constitutive elements along the major axis was varied from 30 to 200 nm. The simulations were done for stacks of 60 elements, since the previous simulations (Figure VII.3-2) had not revealed any significant differences in the responses of stacks of 60 and 240 elements.

For each eigen mode of the isolated elements of each size, the weighted average value of the ellipticity was calculated as $\bar{\varepsilon} = \frac{\sum_i \tilde{m}_i \frac{m_i^z}{m_i^y}}{\sum_i \tilde{m}_i}$ where $\tilde{m}_i$ denotes the Fourier amplitude of the given mode in i^{th} cell and the summation is performed over the volume of the element. Then, the widths of the corresponding magnonic bands were extracted from the dispersions calculated for the stacks of such elements, with the

positive and negative values of the width values assigned to the positive and negative dispersion respectively. The results are presented in Figure VII.3-3.

Generally, the ellipticity of the modes of the isolated element increases as their frequency increases, in line with the enhanced role of the exchange interaction for higher frequency modes. The ellipticity of the lower frequency modes is defined mainly by the anisotropic dipolar energy, leading to the non-circular precession. For higher frequencies, the dynamics is dominated by the isotropic exchange interaction, and so, the precession is almost circular (Figure VII.3-3). Generally, the ellipticity of the fundamental bulk mode decreases as the size of the element increases, which could be understood by the increasing shape anisotropy and decreasing exchange interaction. In turn, the ellipticity of the edge mode increases with the size of the element, which could be attributed to changes of the mode profile.

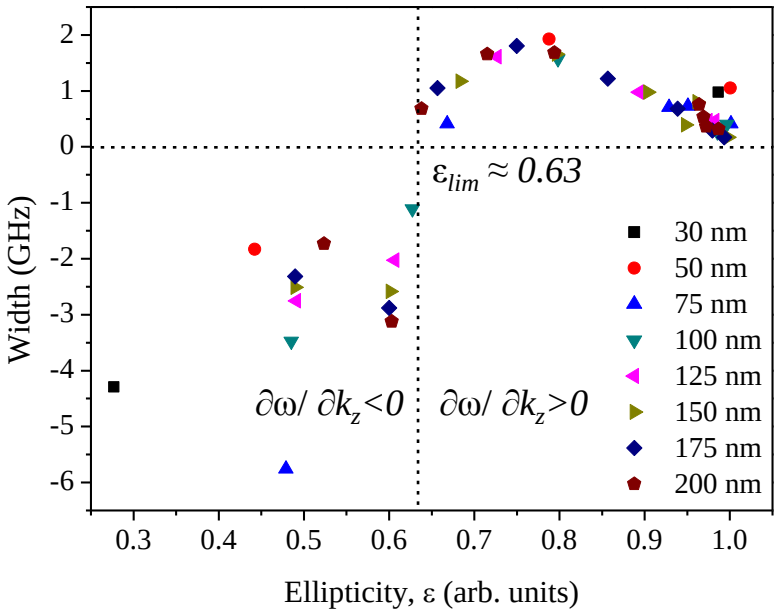

Figure VII.3-3 The widths of the collective magnonic bands are shown as a function of the ellipticity of the corresponding modes of the isolated elements.

The main feature of the data presented in Figure VII.3-3 is the presence of the critical value of the ellipticity $\varepsilon_{lim} \approx 0.63$ above which the magnonic dispersion becomes positive. Only two modes were found to have ellipticities below the critical value. In particular, the edge mode always has ellipticity below the critical value. The fundamental bulk modes have ellipticity below the critical value only for elements that are larger than 75 nm. Hence, by altering the dimensions of the constituent elements, it is possible to control the magnonic dispersion in the stack; at least as far as the fundamental bulk mode is concerned. The observed gradual decrease of the ellipticity of the higher order bulk modes with the size of the element suggests that they might also show negative dispersion eventually.

The critical value of the ellipticity is found to be independent of the shape of the isolated element, suggesting that it could be related to the fundamental properties of the magneto-dipole interaction. To verify this hypothesis, we applied the theory of collective modes developed in Ref. 140 to the case of a stack of two elements. Then, the critical value of the ellipticity can be evaluated analytically as $\varepsilon = \sqrt{\frac{1}{3(\nu_\delta^z)^2 - 1}} \approx 0.707$ where ν_δ^z denotes the z-component of the unit vector between the two points of interacting elements (for our particular case $\nu_\delta^z = 1$). The account of higher-order multipole moments would obviously change the value. Nevertheless, the result is already very close to the one obtained from simulations (≈ 0.63). The analytical theory suggests that the critical value of the ellipticity is invariant to the magnetic parameters and shape of and the distance between the elements, but will be different for different stacking geometries.

Figure VII.3-4 (a) and (b) presents the spatial character of the two groups of dispersionless modes shown in Figure VII.3-2. The spatial character of modes of the isolated element is preserved in the corresponding collective modes of the stack.

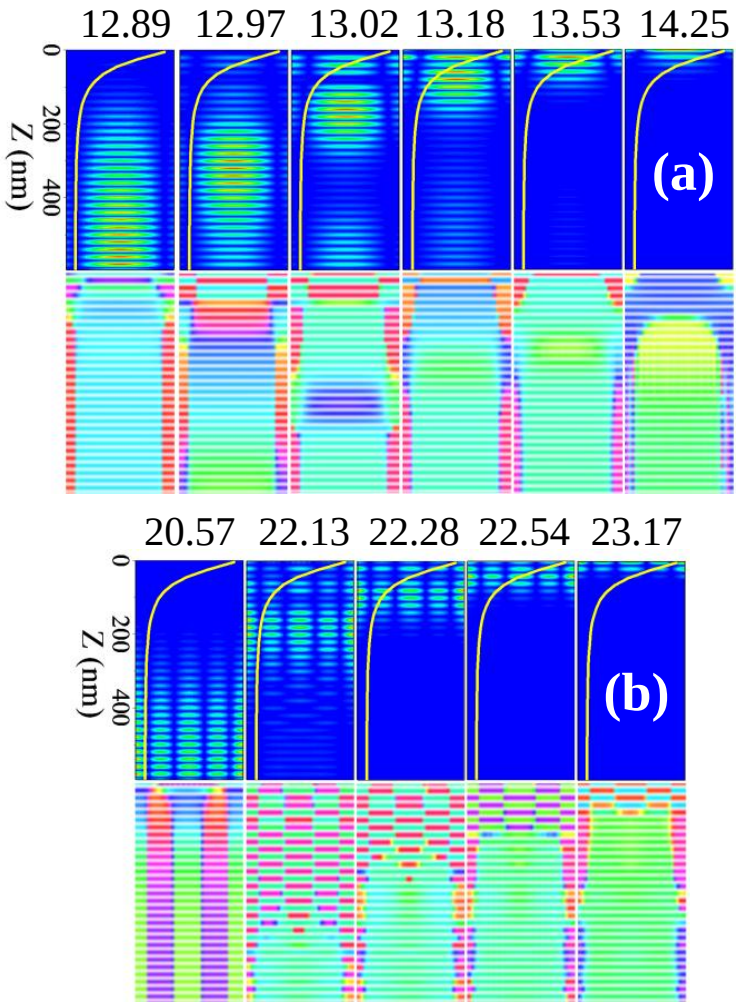

Figure VII.3-4 The spatial maps of the Fourier amplitude corresponding to the localized modes originating from the bulk (a) and high order bulk (b) modes of the isolated element (shown Figure VII.3-2). The top and bottom images in each row represent the spatial distributions of the magnetization amplitude and phase respectively. The numbers above the images represent the mode frequencies in GHz. The insets show the profile of the projection of the sum of the demagnetizing and applied fields onto the static magnetization for the major symmetry axis of the stack (z symmetry axis).

However, the amplitude of the latter modes varies in the stacking direction, which is perpendicular to that of the applied field. As expected, the frequencies of the

modes increase as they become more strongly localized near the top and bottom of the stack, where the static internal magnetic field is strongest (Figure VII.3-4 (c)).

To understand the mechanism of localization, let us consider the spatial character of a spin wave mode of a particular frequency. If the static internal magnetic field is non-uniform, the dynamic magnetic field must also vary so as to keep the mode frequency constant. The dynamic field depends upon the non-uniformity of precession in the region of interest. The character of the dependence is in turn determined by the character of the spin wave dispersion in the vicinity of the mode frequency. So, assuming that some effective "local value" of the wave number could be introduced, the increase of the static field must result in an increase (decrease) of the wave number for negative (positive) dispersion. The mode has propagating character (real wave number) as long as the dispersion can account for the variation of the static field. However, in the region of the sample where the required compensation cannot be achieved by the variation of the real wave number (classically forbidden region), the spin wave number acquires an imaginary value. Finally, the proposed mechanism of localisation of magnons is similar to the propagation of the electron in the spatially non-uniform potential, and so the same framework could be applied to magnons in order to find stable localised states.

In the present case of the magnonic band spectrum, additional limitations on the wave number are imposed by the edges of the Brillouin zones, with the maximum compensation determined by the width of the magnonic band. In particular, in magnonic bands with negative dispersion (e.g. those originating from the edge and fundamental bulk modes), the effective wave number decreases from the top and bottom of the stack towards its centre (Figure VII.3-4(a)), until the centre of the Brillouin zone is reached (if reached at all), with the corresponding point (element of the stack) playing role of a

classical "turning point". In magnonic bands with positive dispersion (e.g. those originating from the higher order bulk modes), the effective wave number increases from the top and bottom of the stack towards its centre (Figure VII.3-4(b)), and the turning point is located where the boundary of the Brillouin zone is reached. The maximal amplitudes of the modes are observed (i.e. the modes are localized) between either two turning points, or the boundaries of the stack, or a turning point and a boundary of the stack. Depending on the relative strength of the dispersion and the variation of the internal field (Figure VII.3-4(c)), there is a possibility of spin wave trapping between two turning points (defined by the top and bottom of the magnonic band) located on the slope of the non-uniform internal magnetic field. Data presented in Figure VII.3-2 confirms that the number of the localized states decreases as the dispersion within and hence the width of the associated magnonic bands increases, consistent with the localization mechanism described above.

VII.4 Conclusions

In summary, we have studied the spectrum and dispersion of magnonic modes in stacks of dipolarly coupled magnetic elements. In particular, we have found that the sign of the magnonic dispersion is determined by the spatial character and ellipticity of the corresponding modes of an isolated element. Moreover, we have determined a critical value of the ellipticity at which the sign of the magnonic dispersion changes from negative to positive in a discontinuous way. The discovered effect opens a new way of tailoring the dispersion of collective spin waves in magnonic crystals. Moreover, we have observed a new type of the spin wave localization. In contrast to the previous studies[144], the localization is associated with regions of increased rather decreased internal magnetic field formed near the boundaries of the stack.

VIII Micromagnetic method of s-parameter characterization of magnonic devices

VIII.1 Introduction

Nanoscale magnonic devices open an intriguing path towards analog signal processing in the sub-terahertz frequency band[32,149,150]. In particular, the use of propagating spin waves[24,46] offers direct processing, in which no frequency conversion is required prior to the signal manipulation, thereby reducing processing time and facilitating real-time devices. This is in addition to the long known opportunity to combine the signal processing with the re-configurability and data storage functionality within the same chip. As the number of concepts and modifications of magnonic devices continues to rapidly grow[98,149,151,152,153,154,155,156], there also grows the demand for methods of performance evaluation without building prototypes or developing theoretical models at the microscopic level of description.

Here, we propose a numerical micromagnetics version of such a method, in which magnonic devices are considered as two-port linear networks and can therefore be described in terms of their s-parameters (i.e. reflection and transmission characteristics).

The magnonic "device-under-test" is situated between input and output magnonic waveguides. The dispersion relations and amplitudes of spin waves in the input and output are calculated from micromagnetic simulations using the methodology described e.g. in Refs. 134 and 135. The results are then used to derive the reflection and transmission characteristics (coefficients) of the evaluated device as a function of the spin wave frequency. The calculations in this paper have been performed using the OOMMF. However, any of the existing micromagnetic packages[157,158,159,160] could also be used for this purpose, at least in principle, provided that the required data analysis software is developed.

VIII.2 Method

The geometry of the micromagnetic problem is shown in Figure VIII.2-1. The sample has a total length of 10.5 μm, a width of 100 nm, and a thickness of 10 nm. Its inner part consists of the 2.5 μm long "input" and "output" waveguides (marked as I and III respectively) and the 100 nm long "device-under-test" (marked as I). The input and output waveguides are made of Py[99] and the device-under-test (considered here for the purpose of demonstration) is represented by a uniform cobalt layer[161]. The Gilbert damping constant α is set to the same value 0.001 in the three layers. The outer layers (marked as "D") have the same magnetic parameters as the input and output waveguides, except the Gilbert damping constants. The latter are now set to 0.1 in order to absorb spin waves reaching the layers and thereby to suppress back reflection from the layers and hence also from the ends of the sample. No anisotropy other than that naturally resulting from the magneto-dipole energy is included in the calculation.

First, the ground state is obtained by relaxation from a perfect saturated state along the length of the sample to the state at the bias field H_b of 1 kOe applied in the

same direction. Then, the sample is excited by applying a highly localized transient magnetic field with temporal profile

$$h(t_n) = h_0 \mathrm{sinc}(2\pi f_0 t_n), \qquad \text{(VIII.2-1)}$$

at the boundary between the left damped layer and the input waveguide (I). The amplitude of the transient field is $h_0 = 50\,Oe$. Ideally, the field defined by temporal profile (VIII.2-1) should lead to excitation of propagating spin waves of nearly equal amplitude at frequencies up to the cut-off value of $f_0 = 4\,THz$, which is not the case in practice due to the limited duration of the simulation. In order to partly suppress the corresponding distortion of the excitation spectrum, the centre of the transient field is delayed relative to the start of the simulation by time t_0 equal to 10 periods of the sinc function. Each simulation is run for 8 ns and the data are recorded every $\Delta t = 120\,fs$. The corresponding frequency bandwidth f_{max} of the simulations is equal to $f_{max} = 0.5/\Delta t = 4.17\,THz$. So, the condition $f_0 < f_{max}$ necessary to prevent aliasing, is satisfied.

The cell size of the rectangular mesh is equal $s_x \times s_y \times s_z = 1 \times 100 \times 10\,nm^3$, and so, the width and thickness of the mesh cell coincide with the corresponding dimensions of the sample. Hence, the model is one dimensional (1D). So, wave vectors $\mathbf{k}_i$, $\mathbf{k}_r$ and $\mathbf{k}_t$ of the incident, reflected, and transmitted spin waves respectively are parallel to the length of the sample and therefore to the bias magnetic field and the static magnetisation. The wave vector bandwidth of the simulations is $\mathbf{k}_{max}/2\pi = 0.5/s_x = 0.5{\cdot}10^9\,m^{-1}$. Prior to the Fourier analysis, the static magnetization profile is subtracted from the dynamical data, in order to extract the pure dynamic component of the magnetization $\mathbf{m}(\mathbf{r}, t)$. The method described below is then applied to the z-component of the dynamic magnetisation $m_z(\mathbf{r}, t)$.

The method implemented here for the s-parameter extraction is based on the method of the magnonic dispersion calculation developed and described in Refs. 134 and 135. The main idea is to make use of information about spin wave amplitudes $m(k,f)$ that is obtained as a result of the calculation of spin wave dispersion $f(k)$, similar to those shown in Figure VIII.2-2. By applying this method separately to the input and output waveguides, one can calculate the complex Fourier amplitudes of the input and output signals and form complex transmission and reflection coefficients as their ratios. However, the practical realization of the idea meets some difficulties, as detailed below.

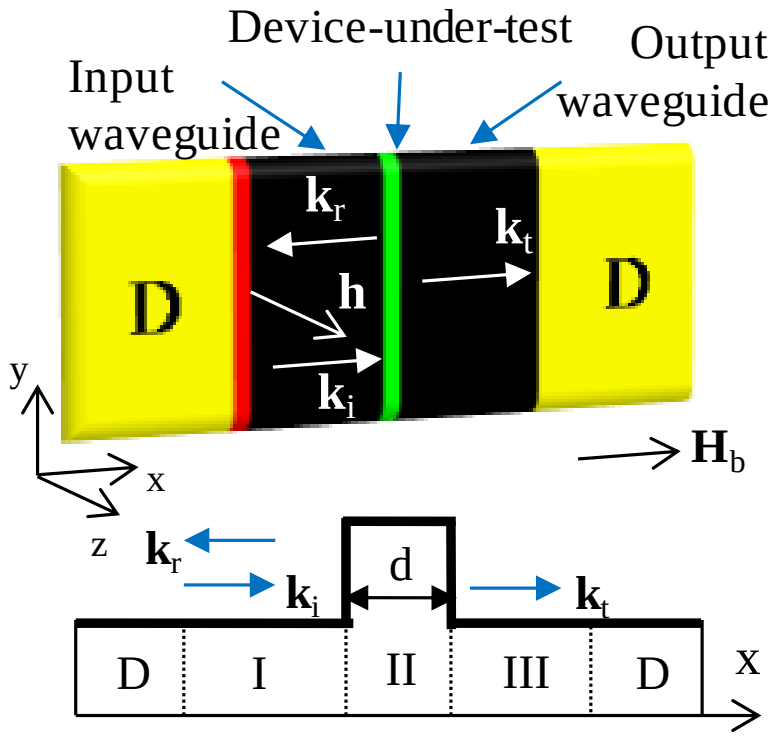

Figure VIII.2-1 The top panel shows the geometry of the micromagnetic problem. The bottom panel schematically shows the coordinate dependence of the magnetic parameters (except damping) in the sample. Both schematics are drawn not to scale.

The results of the time domain simulations are obtained as a 2D array of data $m_z(x_i, t_j)$, where i and j are integer indices of the mesh cells and time steps respectively. By performing a 2D Fourier transform of the data, spin wave amplitudes $m(k_i, f_j)$ are calculated as a function of discrete valued wave vector k_i and frequency f_j (Figure VIII.2-2). First, we find the dispersion in the form of a continuously valued frequency defined on the discrete mesh of the wave number, $f_i = f(k_i)$. We assume that the spin wave dispersion $f(k)$ is equivalent for the forward ($k > 0$) and backward ($k < 0$) propagating spin waves, i.e. $f(k) = f(-k)$ [162]. For each $|i|$, we use cubic interpolation to find frequencies $f_i = f(k_i)$ as points at which functions $m(k_i, f) + m(k_{-i}, f)$ of continuously valued frequency f reach their local maxima[163]. Then, we extract the amplitudes of the backward and forward propagating spin waves separately from the $k < 0$ and $k > 0$ branches of the dispersion respectively using bilinear interpolation of $m(k_i, f_j)$ to $m_i(k_i, f_i)$, with the latter now being a discrete 1D set of data. The interpolation algorithm is adjusted so that the discretization of the frequency rather than wave vector remains equidistant. This allows us to use the same frequency mesh to compare amplitudes of spin waves extracted from different simulations. This is preferred since we are interested in the frequency (rather than wave number) dependence of the s-parameters.

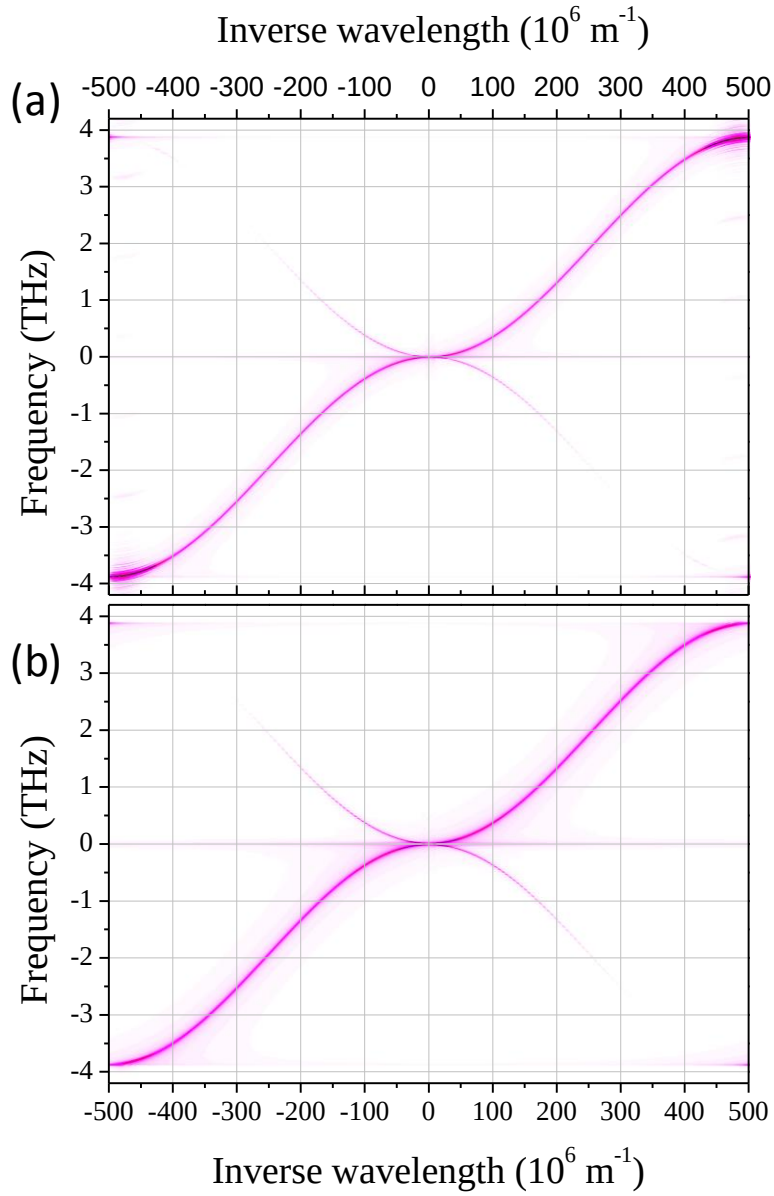

Figure VIII.2-2 The dispersion of spin waves in the "input" waveguide is shown for simulations performed in exchange (a) and dipolar-exchange (b) approximations. The colour intensity represents the absolute value of the spin wave amplitude.

Ideally, the s-parameters could be extracted from a single simulation. However, due to effects connected with the finite damping and group velocity of spin waves in the input and output waveguides, two different simulations have to be performed. First, we perform a reference simulation for a sample like the tested one but in which the device-under-test is replaced by a uniform layer with the properties, width and thickness of the

input and output waveguides and the length of the device-under-test. The reference sample is therefore magnetically uniform. Reference amplitudes $m_{R,I}^{f}(f)$ and $m_{R,III}^{f}(f)$ of the forward spin waves in the input and output waveguides respectively are then calculated as functions of the frequency. Then, simulations for the sample with the device-under-test are performed, and amplitudes $m_{I}^{b}(f)$ and $m_{III}^{f}(f)$ of the reflected from and transmitted through the device-under-test spin waves propagating in the input and output waveguides respectively are obtained.

Finally, the values of s-parameters S_{11} and S_{21} are calculated as

$$S_{11} = \frac{m_{I}^{b}}{m_{R,I}^{f}} = R(f)$$
$$S_{21} = \frac{m_{III}^{b}}{m_{R,III}^{f}} = T(f) \qquad \text{(VIII.2-2)}$$

where $T(f)$ and $R(f)$ are the transmission and reflection coefficients respectively. The damped regions must of course be excluded from the analysis. For each particular problem (i.e. magnonic device tested), the length of the input and output waveguides has to be optimized so as to obtain the required spectral resolution of the subsequent Fourier analyses and to allow spin waves with the smallest group velocities to reach the device-under-test well within the simulation time.

VIII.3 Application to the uniform inclusion of *Cobalt* as the device-under-test

In order to demonstrate advantages and limitations of the method, we apply it to calculation of the reflection and transmission characteristics of a device-under-test represented by a uniform inclusion of Co. Figure VIII.3-1 shows the dispersion of spin waves calculated for the reference sample (excluding damped regions) and then "digitized" using the method described in Section VIII.2. In OOMMF, the simulations

can be easily performed in dipole-exchange, dipole (magnetostatic) and exchange approximations. The exchange and dipole-exchange approximations produce very similar results at frequencies above about 100 GHz, while the dipole and dipole-exchange curves agree only in close vicinity of the uniform ferromagnetic resonance frequency, i.e. at wave numbers up to about $6\pi \cdot 10^4\ m^{-1}$.

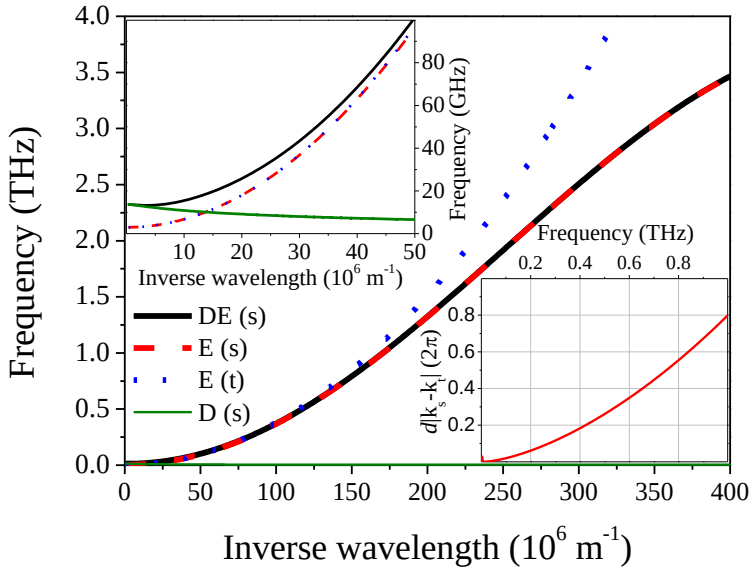

Figure VIII.3-1 The dispersion curves of spin waves calculated from simulations for the reference sample (excluding damped regions) and then digitized is shown for dipole-exchange (DE), dipole (D) and exchange (E) approximations. The curves are marked by "s" in the legend. The analytical curve (t) calculated in the exchange approximation is also shown. The upper inset shows the same dispersion on a greater scale. The bottom inset shows, as a function of the spin wave frequency, the absolute value of the difference between the analytical and simulated curves calculated in the exchange approximation in the units of the Co layer thickness.

In the exchange approximation, the dispersion can also be easily calculated analytically, facilitating verification of the method. The comparison appears to show an excellent agreement between the theory and simulations at frequencies up to about 0.5 THz. At higher frequencies, the simulated dispersion curve has a downward curvature as a result of the discrete nature of the numerically solved problem[164]. Indeed, the highest frequency and wave number accessible in the simulations correspond to the edge of the Brillouin zone of the spectrum of the 1D chain of spins with a period equal to the cell size. Nevertheless, at such a high values of wavevectors, continuous approximation used to derive magnonic dispersion analytically is not valid anymore, and so discrete model of ferromagnetic media must be used. It is worth noting that magnonic dispersion calculated with discrete model of ferromagnetic media will also has downward curvature.

Figure VIII.3-2 shows the squared amplitudes of the reflection and transmission coefficients simulated and analytically calculated in the exchange approximation. The curves are characterized by a quasi-periodic alteration of regions of high and low transmission and reflection. The alteration originates from the Fabry-Perot resonance of spin waves in the cavity represented by the Co layer, with the frequency of alteration determined by its thickness. The predictions of the simulations and analytical theory for positions of the minima and maxima of reflection and transmission agree at lower frequencies < 200 GHz, while slowly "dephasing" at higher frequencies and then coming into phase again at frequencies about 1 THz. The dephasing originates from the difference between simulated and analytical dispersion curves illustrated in the bottom inset of Figure VIII.3-2. The amplitude of variation of the simulated transmission coefficient agrees well with the analytical theory, while the simulations tend to underestimate the variation in the reflection coefficient.

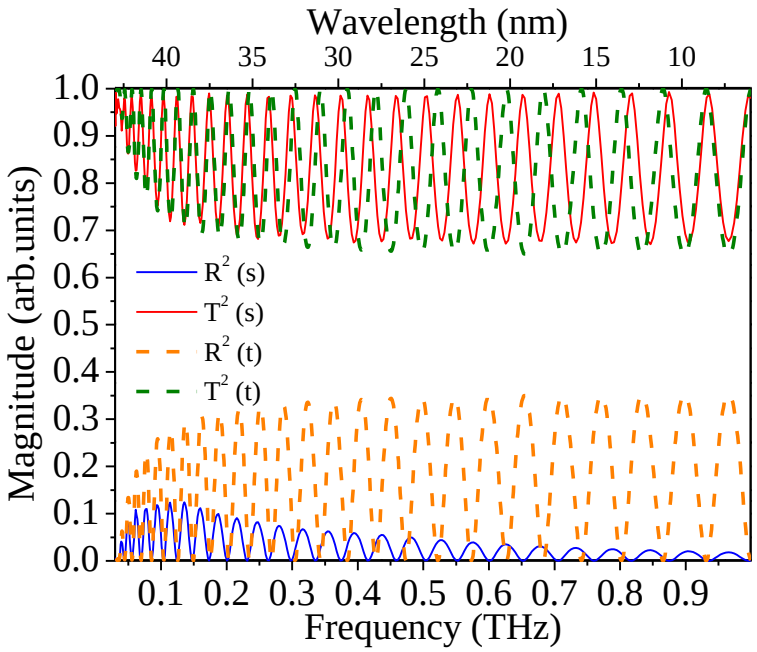

Figure VIII.3-2 The squared amplitudes of the simulated (s, solid lines) and analytical (t, dashed lines) reflection (R) and transmission (T) coefficients are shown for the exchange approximation.

The latter discrepancy could be attributed to the effect of (small but finite) damping in the simulations and then to accumulation of spin wave energy in and in the vicinity of the Co layer. In principle, the damping in the latter could be included in the theory. However, it has to be set to zero in the input and output waveguides since the incident and scattered spin waves are defined "at infinity". In contrast, the amplitude extracted from simulations represents a result of averaging over the entire length of the waveguide. At the same time, the Co layer is expected to lead to appearance of localized "defect" modes[164,165]. The localized spin waves gain their energy from the incident spin wave and hence might lead to the observed discrepancy.

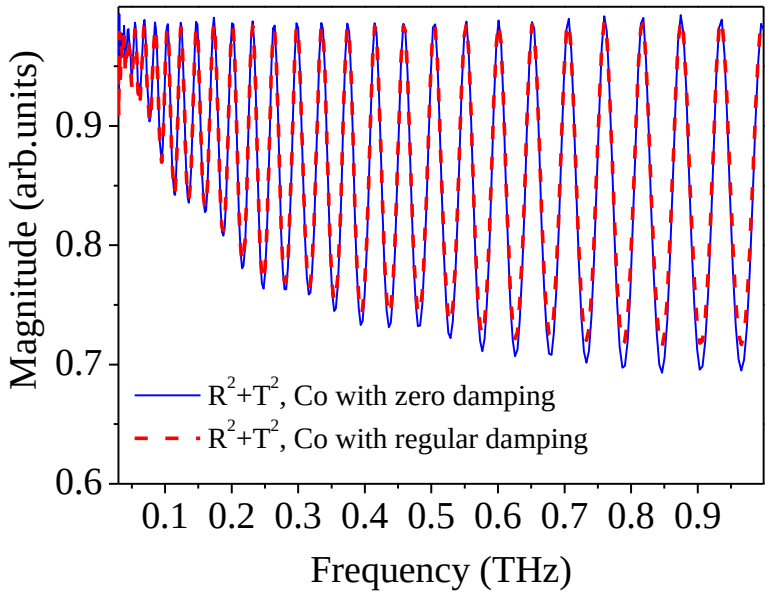

Figure VIII.3-3 The sum of the squared absolute values of the simulated reflection and transmission coefficients is shown for the case of Co layer with zero (solid line) and non-zero (α = 0.001, dashed line) damping. The frequencies at which the sum is not equal to unity correspond to those of the minimum transmission of the spin waves through the Co layer.

So, Figure VIII.3-3 compares the sums of the squared absolute values of the simulated reflection and transmission coefficients extracted from simulations with the damping in the Co layer set to zero and a finite value (α = 0.001). One can notice a set of frequencies at which the sum falls below unity and hence the energy conservation law is violated. The effect is more significant in the case of zero damping. This favours the interpretation based on the energy accumulation by the spin wave modes localized at the Co layer.

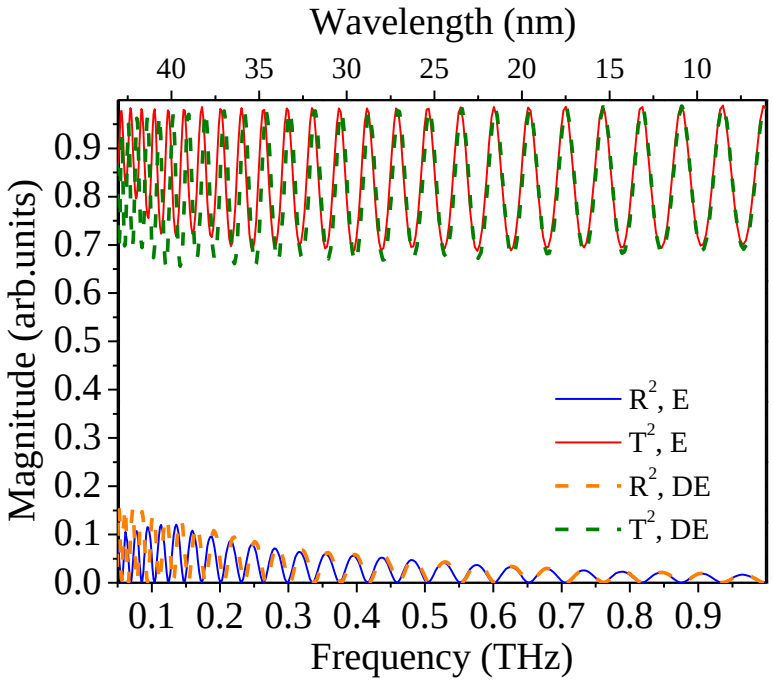

Figure VIII.3-4 The squared absolute values of the reflection (R) and transmission (T) coefficients simulated in the case of exchange (E, solid lines) and dipolar-exchange (DE, dashed lines) approximations are shown.

Figure VIII.3-4 compares the frequency dependences of the reflection and transmission coefficients calculated in the dipole-exchange and exchange approximations. Both reflection and transmission curves agree well at frequencies above about 200 GHz, as expected from the similarity of the corresponding dispersion curves in the frequency range, as shown in Figure VIII.3-2. This demonstrates the applicability of the exchange approximation at the high spin wave frequencies. This allows one to exploit the analogy existing between the exchange spin waves and the motion of an electron in a non-uniform potential, pointed out and exploited e.g. in Refs. 165, 166, 167. The analogy is due to the fact that Landau-Lifshitz equation could be rewritten to the form of Schrodinger equation, where Hamiltonian is replaced by the effective field.

VIII.4 Conclusions

In this Chapter, I have proposed a micromagnetic method by which to evaluate performance of magnonic (spin wave) devices. We have applied the method to a simple rectangular magnetic non-uniformity and have successfully calculated its reflection and transmission coefficients. Our calculation has shown that the accumulation of energy by spin wave modes localized on the non-uniformity might lead to a significant reduction of the reflection coefficient, although the effect depends on the value of damping in the non-uniformity. We have shown that the technique is very efficient in the sub-terahertz band, albeit faces some difficulties in the low gigahertz band associated with the low group velocity of spin waves. We have shown that the exchange approximation is well suited for description of propagating spin waves at THz frequencies. However, our results have also demonstrated that the accuracy of the approximation in a particular problem depends upon the relative value of the spin wave wavelength and the characteristic scale of the non-uniformities in the problem. At THz frequencies, the dispersion obtained from the simulations deviates from that calculated using the continuous medium approximation. This deviation not only emphasizes the discrete nature of the micromagnetic simulations, but also suggests that micromagnetic solvers based on truly atomistic models are required and might well be feasible computationally in future. Indeed, the cell size in the presented simulations is only a few times greater than the inter-atomic distance in the considered magnetic materials' although one should note that the implemented micromagnetic model is one-dimensional. The proposed method is directly comparable to vector network analyser ferromagnetic resonance (VNA-FMR) measurements of magnonic structures and will therefore prove useful for experimentalists working in the area of magnonics.

IX Conclusions

The linear magnetization dynamics in nano-patterned samples has a very complicated character. A certain number of factors make developing of the analytical solutions of the problems presented here almost impossible. Therefore it is crucial to utilize different approaches to the solutions of such systems. One of the possible ways is the micromagnetic simulations. Moreover, micromagnetic simulations could be used along with the analytical approaches. This gives even more insight into dynamic behaviour of the nanoscale magnetic systems.

In Chapter IV, we have developed a numerical tool which allows one to analyse the real space and time domain data generated by micromagnetic packages. In particular our software allows one to extract the spectrum (or dispersion where applicable) of spin-wave modes along with their spatial profiles. This gives virtually full information about the system. Our implementation benefits from reduced memory pressure and exceptional runtime performance. It is the only publically available solution with the described set of capabilities. We have proved its effectiveness through the analysis of the simulations of several large-scale problems including the results presented in this manuscript.

In Chapter V, the dynamic dipolar coupling of two nanoscale rectangular elements have been estimated by the frequency difference between the acoustical and optical modes. In general it has been found that edge mode of the isolated element is subject to larger coupling then the bulk mode. We showed that for two elements placed edge-to-edge the frequencies of the optical modes are lower than that of acoustical. The situation is opposite when the elements are placed side-by-side. This is in line with the symmetry of the dipolar field. Then the results have been compared against an analytical theory. A good agreement has been found for the bulk mode, while only qualitative agreement has been found for the edge mode. This suggests to us that approximation of the rigid oscillators used in the theory is only valid for bulk mode. Indeed micromagnetic simulations confirmed that profile of the edge modes is changed for the closely packed pair. So the energy of interaction of the neighbouring edge regions of different elements exceeds the internal energy of the edge mode, so the latter is non-rigid.

In Chapter VI, the theory study of pairs of closely packed elements has been extended to the case of 2D arrays. The dispersion of the magnonic modes has been calculated numerically for the first time. Moreover we have found that approximation of 3x3 arrays which is widely used in the literature is not valid to describe the large arrays. The localized states of the arrays are found to be sensitive to the parity of the arrays (defined by parity of the number of elements within the column of arrays). In particular the symmetrical properties of the ground state give rise to the dynamic dipolar coupling of the localized modes. We have proposed a method how the influence of the ground state could be evaluated by estimating a weighted average of the static internal field for each particular mode. It has been found that dispersion of collective modes is much stronger across the columns of arrays then along the rows. This is in line with the observations for the pairs of elements.

The investigation of 3D confinement of spin waves in stacks of dipolar coupled rectangular nano-elements provided in Chapter VII revealed that the sign of the group velocity of the magnonic modes is in strong correlation with the ellipticity of the originating modes of the single element. In particular there is a critical value of the ellipticity above which the dispersion of magnonic modes becomes positive. Numerical simulations of the stacks of elements of different in-plane aspect ratio depict that this critical value is independent on the shape of the element. The latter has been confirmed by simple analytical considerations. Thus, we conclude that critical value of ellipticity is fixed by the topology (fine structure) of the sample only. This opens new ways in tailoring the dispersion of spin waves in magnetic nano-structures. Additionally, we have found that finite width of the magnonic bands results in localization of modes on the regions of gradually increasing internal field. This is in contrast to the previous studies, where similar effect has been observed but for gradually decreasing fields (by the analogy to localizations on potential wells in quantum mechanics).

In Chapter VIII, the method for the estimation of scattering parameters of magnonic devices is proposed. It is based on the calculation of the dispersion of spin waves in input and output waveguides, so that the amplitudes of propagating spin waves could be extracted. The values of scattering parameters are calculated as a ratio of corresponding amplitudes of reflected and transmitted waves to the amplitude of the incident spin waves. We have applied the method to the simplistic model of a uniform inclusion (by analogy to the rectangular potential barrier in quantum mechanics). The analytical expression has been derived for the given problem in exchange approximation. We have found that our method is in a good agreement with an analytical theory. Nevertheless, we have found that dispersion of spin waves calculated in OOMMF differs from that of analytical theory. In particular the analytical theory is developed for the continuous approximation, while OOMMF simulates a lattice of

magnetic moments. For the large wave vectors the continuous approximation is not valid. Thus dispersion calculated by OOMMF has more realistic shape. In order to reproduce the correct dispersion of spin waves in the regions of the large values of vectors it is essential to run atomistic scale simulations. Nevertheless we have found that OOMMF could be used to study spin waves in Permalloy with the frequencies up to 200 GHz. Finally, we have found that potential barrier supports existence of localized modes. This explains the break of the energy conservation law observed in our simulations, since localized modes accumulate energy from the incident spin waves. This effect is not accounted in the calculations of scattering parameters.

Here we have demonstrated through the set of systematic investigations, that micromagnetic simulations could be successfully used to predict the results unknown before. Moreover they can be used to estimate the approximations of the analytical theories, when it is not possible from experimental point of view. Thus micromagnetic simulations are essential tool for exploration of magnetic systems on nanoscale.

X List of Publications

1. M. Dvornik and V. V. Kruglyak, *Dispersion of collective magnonic modes in stacks of nanoscale magnetic elements*, Phys. Rev. B **84**, 140405R (2011).
2. M. Dvornik, P. V. Bondarenko, B. A. Ivanov, and V. V. Kruglyak, *Collective magnonic modes of pairs of closely spaced magnetic nano-elements*, J. Appl. Phys. 109, 07B912 (2011).
3. M. Dvornik, A. N. Kuchko, and V. V. Kruglyak, *Micromagnetic method of s-parameter characterization of magnonic devices*, J. Appl. Phys. 109, 07D350 (2011).
4. P. S. Keatley, P. Gangmei, M. Dvornik, R. J. Hicken, J. R. Childress, and J. A. Katine, *Large amplitude magnetization dynamics and the suppression of edge modes in a single nanomagnet*, Appl. Phys. Lett. 98, 082506 (2011).

XI Bibliography

1 V.V. Zhirnov, R.K. III Cavin, J.A. Hutchby, G.I. Bourianoff, Proceedings of the IEEE **91**, 1934 (2003).

2 G. Moore, Electronics **38** (1965).

3 V. M. Kendon, K. Nemoto, W. J. Munro, Philosophical Transactions Of The Royal Society A-Mathematical Physical And Engineering Sciences **368**, 3609 (2010).

4 F. Schwierz, Nature Nanotechnology **5**, 487 (2010).

5 J. Clark, G. Lanzani, Nature Photonics **4**, 438(2010).

6 S. Shoshani , T. Ratner, R. Piran, E. Keinan, Israel Journal Of Chemistry **51**, 67 (2011).

7 Y.-M. Lin, C. Dimitrakopoulos, K. A. Jenkins, D. B. Farmer, H.-Y. Chiu, A. Grill and Ph. Avouris, Science **327**, p. 662 (2010).

8 K. L. Brown, W. J. Munro, V. M. Kendon, Entropy **12**, 2268 (2010).

9 K. Vogt, H. Schultheiss, S. J. Hermsdoerfer, P. Pirro, A. A. Serga, and B. Hillebrands, Appl. Phys. Lett. 95, 182508 (2009).

10 M. Dvornik, A. N. Kuchko, and V. V. Kruglyak, J. Appl. Phys. **109**, 07D350 (2011).

11 P. Gepner, D. L. Fraser and M. F. Kowalik, Lecture Notes in Computer Science **6067** (2010).

12 C. W. Sandweg, Y. Kajiwara, A. V. Chumak, A. A. Serga, V. I. Vasyuchka, M. B. Jungfleisch, E. Saitoh, and B. Hillebrands, Phys. Rev. Lett. 106, 216601 (2011).

13 K. Uchida, S. Takahashi, K. Harii, J. Ieda, W. Koshibae, K. Ando, S. Maekawa and E. Saitoh, Nature **455**, pp. 778-781 (2008).

14 V. E. Demidov, S. Urazhdin, V. Tiberkevich, A. Slavin, and S. O. Demokritov, Phys. Rev. B **83**, 060406 (2011) .

15 K.-S. Lee and S.-K. Kim, J. Appl. Phys. **104**, 053909 (2008).

16 A. D. Karenowska, A. V. Chumak, A. A. Serga, J. F. Gregg, and B. Hillebrands, Appl. Phys. Lett. **96**, 082505 (2010).

17 S.-K. Kim, K.-S. Lee, and D.-S. Han, Appl. Phys. Lett. **95**, 082507 (2009).

18 M. Dvornik and V. V. Kruglyak, accepted to Phys. Rev. B Rapid. Comm.

19 M. Kostylev, P. Schrader, R. L. Stamps, G. Gubbiotti, G. Carlotti, A. O. Adeyeye, S. Goolaup, and N. Singh, Appl. Phys. Lett. **92**, 132504 (2008).

20 V. V. Kruglyak, P. S. Keatley, A. Neudert, R. J. Hicken, J. R. Childress, and J. A. Katine, Phys. Rev. Lett. **104**, 027201 (2010).

21 F. Moussa, M. Hennion, P. Kober-Lehouelleur, D. Reznik, S. Petit, H. Moudden, A. Ivanov, Ya. M. Mukovskii, R. Privezentsev, and F. Albenque-Rullier , Phys. Rev. B **76**, 064403 (2007).

22 T. Tsuboi, Phys. Rev. B **32**, 3164 (1985).

23 A. Misra and R. H. Victora, Phys. Rev. B **73**, 172414 (2006).

24 A. G. Gurevich and G. A. Melkov, Magnetization Oscillations and Waves (Chemical Rubber Corp., New York, 1996).

25 V. E. Demidov, S. O. Demokritov, K. Rott, P. Krzysteczko, and G. Reiss, Phys. Rev. B **77**, 064406 (2008).

26 V. E. Demidov, H. Ulrichs, S. Urazhdin, S. O. Demokritov, V. Bessonov, R. Gieniusz, and A. Maziewski, Appl. Phys. Lett. **99**, 012505 (2011).

27 A. B. Ustinov, B. A. Kalinikos, V. E. Demidov, and S. O. Demokritov, Phys. Rev. B **81**, 180406 (2010).

28 V. E. Demidov, J. Jersch, K. Rott, P. Krzysteczko, G. Reiss, and S. O. Demokritov, Phys. Rev. Lett. **102**, 177207 (2009).

29 S. O. Demokritov, V. E. Demidov, O. Dzyapko, G. A. Melkov, A. A. Serga, B. Hillebrands and A. N. Slavin, Nature **443**, 430 (2006)

30 A. Kirilyuk, A. V. Kimel and T. Rasing, Rev. Mod. Phys. 82, pp. 2731-2784 (2010).

31 L.D. Landau, E.M. Lifshitz, Phys. Z. Sowietunion **8**, 153 (1935).

32 V. V. Kruglyak, S. O. Demokritov, and D. Grundler, J. Phys. D: Appl. Phys. **43**, 264001 (2010).

33 I. Neudecker, G. Woltersdorf, B. Heinrich, T. Okuno, G. Gubbiotti, and C. H. Back, J. Magn. Magn. Mater. **307**, 148 (2006).

34 A. V. Chumak, A. A. Serga, S. Wolff, B. Hillebrands, and M. P. Kostylev , Appl. Phys. Lett. **94**, 172511 (2009).

35 P. Langivin, Ann. Chim. Phys. **5**, 70 (1905).

36 P. Weiss, J. de Phys. Rad. **6**, 661 (1907).

37 J. Frenkel, Z. Phys. **49**, 31 (1928).

38 W. Heisenberg, Z. Phys. **49**, 619 (1928).

39 N. S. Akulov, Z. Phys. **67**, 794 (1931).

40 J. Frenkel and J. Dorfman, Nature **126**, 274 (1930).

41 W. Heisenberg, Z. Phys. **69**, 287 (1931).

42 W. Heisenberg, H. Wagner and K. Yamazaki, Il Nuovo Cimento A **59**, 377 (1969).

43 T. Holstein and H. Primakoff, Phys. Rev. **58**, 1098 (1940).

44 J. H. Van Vleck, Rev. Mod. Phys. **25**, 220 (1954).

45 P. A. M. Dirac, Proc. R. Soc. Lond. A October 1, 1926.

46 A. I. Akhiezer, V. G. Baryakhtar, and S. V. Peletminskii, Spin Waves and Magnetic Excitations (North-Holland, Amsterdam, 1968).

47 F. Bitter, Phys. Rev. **38**, 1903 (1931); ibid.**41**, 507 (1932).

48 J. McCord and J. Westwood, IEEE Trans. on Magn. **37**, pp. 1755 – 1757 (2001).

49 I. V. Baryakhtar and V. G. Baryakhtar, Ukr. J. Phys. **43**, 1433 (1998).

50 F. Bloch, Nuclear Induction, Phys. Rev. **70**, pp. 460-473 (1946).

51 S. S. Kalarickal, Pavol Krivosik, M. Wu, C. E. Patton, M. L. Schneider, P. Kabos, T. J. Silva, and J. P. Nibarger, J. Appl. Phys. 99, 093909 (2006).

52 C. Kittel, Phys. Rev. **73**, 155–161 (1948).

53 L. R. Walker, Phys. Rev. 105, 390 (1957).

54 J. R. Eshbach and R. W. Damon, Phys. Rev. **118**, 1208–1210 (1960).

55 M. Donahue and D. G. Porter, OOMMF User's guide, Version 1.0, NISTIR 6376, NIST, 1999, http://math.nist.gov/oommf.

56 K.W. Morton and D.F. Mayers, *Numerical Solution of Partial Differential Equations, An Introduction*., Cambridge University Press, 2005.

57 http://math.nist.gov/oommf/contrib/

58 michael.donahue@nist.gov

59 M. J. Donahue, IEEE Trans. on Magn. **45**, 3923-3925 (2009).

60 J. C. Butcher, Numerical Methods for Ordinary Differential Equations, Wiley (2008).

61 Y. Katznelson, *An Introduction to Harmonic Analysis*, 3rd edition, Cambridge University Press (2004).

62 A. Aharoni, J. App. Phys. **83**, 3432-3434 (1998).

63 A. J. Newell, W. Williams, and D. J. Dunlop, J. Geophysical Research - Solid Earth **98**, 9551-9555 (1993).

64 O. Lemcke, http://www.nanoscience.de/group_r/stm-spstm/projects/temperature/download.shtml

65 K. Lebecki, http://info.ifpan.edu.pl/~lebecki/pbc.htm

66 J. Zimmermann, R. Boardman, and H. Fangohr, http://www.soton.ac.uk/~fangohr/software/oxs_uniaxial4.html

67 J. Zimmermann and H. Fangohr, http://www.soton.ac.uk/~fangohr/software/oxs_cubic8.html

68 A. Vanhaverbeke, http://www.zurich.ibm.com/st/magnetism/spintevolve.html

69 W. Wang, C. Mu, B. Zhang, Q. Liu, and J. Wang, http://oommf-2dpbc.sourceforge.net/

70 J.C. Slonczewski, Journall of Magnetism and Magnetic Materials **159,** p. L1-L7 (1996)).

71 K. Diefendorff, *Pentium III = Pentium II + SSE*, Microprocessor Report **13** (1999).

72 N. Soveiko, M. S. Nakhla, R. Achar, IEEE Trans. On Computer-Aided Design Of Integrated Circuits And Systems **29**, p. 65-77 (2010).

73 O. Dmytriiev et al., "High frequency permeability of magnonic metamaterials with complex magnetic inclusions", to be submitted to PRB.

74 http://www.originlab.com/

75 http://www.mathworks.co.uk

76 http://developer.amd.com/libraries/acml/downloads/pages/default.aspx

77 S.O. Demokritov and V.E. Demidov, IEEE Trans. on Magn. **44**, p. 6-12(2008).

78 Léon Brillouin, Ann. Phys. (Paris) 17, 88 (1922).

79 L.I. Mandelstam, Zh. Russ. Fiz-Khim., Ova. 58, 381 (1926).

80 M. P. Kostylev, G. Gubbiotti, J.-G. Hul, G. Carlotti, T. Ono, and R. L. Stamps, Phys. Rev. B **76**, 054422 (2007).

81 R. W. Damon and J. R. Eshbach, J. Phys. Chem. Solids **19**, 308 (1961).

82 H. Nyquist, "Certain topics in telegraph transmission theory", Trans. AIEE **47**, pp. 617–644 (1928).

83 C. E. Shannon, "Communication in the presence of noise", Proc. Institute of Radio Engineers **37**, pp. 10–21 (1949).

84 A. Vansteenkiste and B. Van de Wiele, arXiv:1102.3069v2.

85 M. Pardavi-Horvath, C. A. Ross, and R. D. McMichael, IEEE Trans. Magn. **41**, 3601 (2005).

86 A. Y. Galkin, B. A. Ivanov, and C. E. Zaspel, Phys. Rev. B **74**, 144419 (2006).

87 G. Gubbiotti, S. Tacchi, G. Carlotti, N. Singh, S. Goolaup, A. O. Adeyeye, and M. Kostylev, Appl. Phys. Lett**. 90**, 092503 (2007).

88 L. Giovannini, F. Montoncello, and F. Nizzoli, Phys. Rev. B **75**, 024416 (2007).

89 P. S. Keatley, V. V. Kruglyak, A. Neudert, E. A. Galaktionov, R. J. Hicken, J. R. Childress, and J. A. Katine, Phys. Rev. B **78**, 214412 (2008).

90 J. B. Wang, B. Zhang, Q. F. Liu, Y. Ren, and R. L. Liu, J. Appl. Phys. **105**, 083908 (2009).

91 Z. K. Wang, V. L. Zhang, H. S. Lim, S. C. Ng, M. H. Kuok, S. Jain, and A. O. Adeyeye, ACS Nano **4**, 643 (2010).

92 V. V. Kruglyak, P. S. Keatley, A. Neudert, R. J. Hicken, J. R. Childress, and J. A. Katine, Phys. Rev. Lett. **104**, 027201 (2010).

93 P. V. Bondarenko, A. Y. Galkin, B. A. Ivanov, and C. E. Zaspel, Phys. Rev. B **81**, 224415 (2010).

94 S. Tacchi, M. Madami, G. Gubbiotti, G. Carlotti, H. Tanigawa, T. Ono, and M. P. Kostylev, Phys. Rev. B **82**, 024401 (2010).

95 Y. J. Cao, G. H. Yun, X. X. Liang, and N. S. Bai, J. Phys. D: Appl. Phys. **43**, 305005 (2010).

96 B. C. Stipe et al, Nature Photonics **4**, 484 (2010).

97 V. I. Vasyuchka, G. A. Melkov, A. N. Slavin, A. V. Chumak, V. A. Moiseienko, and B. Hillebrands, J. Phys. D: Appl. Phys. **43**, 325001 (2010).

98 A. Khitun, M. Q. Bao, and K. L. Wang, J. Phys. D: Appl. Phys. **43**, 264005 (2010).

99 The magnetization of saturation Ms = $8 \cdot 10^5$ A/m, the gyromagnetic ratio g = 2.1, the exchange constant A = $1.3 \cdot 10^{-11}$ J/m, and the corresponding exchange length $\sqrt{\frac{2A}{\mu_0 M_S^2}} \approx 5\,\mathrm{nm}$.

100 O. Gerardin, H. Le Gall, M. J. Donahue, and N. Vukadinovic, J. Appl. Phys. **89**, 7012 (2001).

101 S. McPhail, C. M. Gurtler, J. M. Shilton, N. J. Curson, and J. A. C. Bland, Phys. Rev. B **72**, 094414 (2005).

102 Z. K. Wang, H. S. Lim, V. L. Zhang, J. L. Goh, S. C. Ng, M. H. Kuok, H. L. Su, and S. L. Tang, Nanolett. **6**, 1083 (2006).

103 B. B. Maranville, R. D. McMichael, and D. W. Abraham, Appl. Phys. Lett. **90**, 232504 (2007).

104 J. Gómez, F. Perez, E. M. Hankiewicz, B. Jusserand, G. Karczewski, and T. Wojtowicz, Phys. Rev. B **81**, 100403 (2010).

105 B. C. Choi, E. Girgis, C. A. Ross, T. Speliotis, Y. K. Hong, G. S. Abo, D. Niarchos, and H. Miyagawa, Phys. Rev. B **81**, 092404 (2010).

106 J. Topp, D. Heitmann, M. P. Kostylev, and D. Grundler, Phys. Rev. Lett. **104**, 207205 (2010).

107 R. P. Tiwari and D. Stroud, Phys. Rev. B **81**, 220403 (2010).

108 I. V. Ovchinnikov and K. L. Wang, Phys. Rev. B **82**, 024410 (2010).

109 S. Neusser, G. Duerr, H. G. Bauer, S. Tacchi, M. Madami, G. Woltersdorf, G. Gubbiotti, C. H. Back, and D. Grundler, Phys. Rev. Lett. **105**, 067208 (2010).

110 K.-D. Lee, K.-S. Ryu, J.-W. Kim, H.-S. Song, J.-W. Jeong, and S.-C. Shin, Phys. Rev. B **82**, 140401 (2010).

111 N. I. Polushkin, Phys. Rev. B **82**, 172405 (2010).

112 S. Jain, M. Kostylev, and A. O. Adeyeye, Phys. Rev. B **82**, 214422 (2010).

113 R. Zivieri, F. Montoncello, L. Giovannini, F. Nizzoli, S. Tacchi, M. Madami, G. Gubbiotti, G. Carlotti, and A. O. Adeyeye, Phys. Rev. B **83**, 054431 (2011).

114 H. T. Nembach, J. M. Shaw, T. J. Silva, W. L. Johnson, S. A. Kim, R. D. McMichael, and P. Kabos, Phys. Rev. B **83**, 094427 (2011).

115 N. Martin, I. Mönch, R. Schäfer, J. Fassbender, L. Schultz, and J. McCord, Phys. Rev. B **83**, 174423 (2011).

116 H. Ulrichs, V. E. Demidov, S. O. Demokritov, A. V. Ognev, M. E. Stebliy, L. A. Chebotkevich, and A. S. Samardak, Phys. Rev. B **83**, 184403 (2011).

117 S. D. Bader, Surf. Sci. **500**, 172 (2002).

118 R. V. Mikhaylovskiy, E. Hendry, and V. V. Kruglyak, Phys. Rev. B **82**, 195446 (2010).

119 L. Bai, M. Kohda, and J. Nitta, Appl. Phys. Lett. **98**, 172508 (2011).

120 R. Zivieri and F. Nizzoli, Phys. Rev. B **71**, 014411 (2005).

121 R. Zivieri and R. L. Stamps, Phys. Rev. B **73**, 144422 (2006).

122 P. Chu and D. L. Mills, Phys. Rev. B **75**, 054405 (2007).

123 V. V. Kruglyak, P. S. Keatley, R. J. Hicken, J. R. Childress, and J. A. Katine, Phys. Rev. B **75**, 024407 (2007).

124 R. E. Arias and D. L. Mills, Phys. Rev. B **79**, 144404 (2009).

125 C. S. Lin, H. S. Lim, C. C. Wang, A. O. Adeyeye, Z. K. Wang, S. C. Ng, and M. H. Kuok, J. Appl. Phys. **108**, 114305 (2010).

126 J. O. Vasseur, L. Dobrzynski, B. Djafari-Rouhani, and H. Puszkarski, Phys. Rev. B **54**, 1043 (1996).

127 S. A. Nikitov, P. Tailhades, and C. S. Tsai, J. Magn. Magn. Mater. **236**, 320 (2001).

128 V. V. Kruglyak and A. N. Kuchko, Physica B **339**, 130 (2003).

129 M. Krawczyk and H. Puszkarski, Phys. Rev. B **77**, 054437 (2008).

130 G. Gubbiotti, S. Tacchi, M. Madami, G. Carlotti, A. O. Adeyeye, and M. Kostylev, J. Phys. D: Appl. Phys. **43**, 264003 (2010).

131 A. A. Serga, A. V. Chumak, B. Hillebrands, J. Phys. D: Appl. Phys. **43**, 264002 (2010).

132 M. Krawczyk, J. Klos, M. L. Sokolovskyy, S. Mamica, J. Appl. Phys. **108**, 093909 (2010).

133 A. A. Awad, G. R. Aranda, D. Dieleman, K. Y. Guslienko, G. N. Kakazei, B. A. Ivanov, and F. G. Aliev, Appl. Phys. Lett. **97**, 132501 (2010).

134 V. V. Kruglyak and R. J. Hicken, J. Magn. Magn. Mater. **306**, 191 (2006).

135 S. – K. Kim, J. Phys. D: Appl. Phys. **43**, 264004 (2010).

136 V. V. Kruglyak, A. Barman, R. J. Hicken, J. R. Childress, and J. A. Katine, Phys. Rev. B **71**, 220409 (2005).

137 G. Gubbiotti, M. Madami, S. Tacchi, G. Carlotti, and T. Okuno, J. Appl. Phys. **99**, 08C701 (2006).

138 C. C. Dantas and L. A. de Andrade, Phys. Rev. B **78**, 024441 (2008).

139 A. Barman and S. Barman, Phys. Rev. B **79**, 144415 (2009).

140 M. Dvornik, P. V. Bondarenko, B. A. Ivanov, and V. V. Kruglyak, J. Appl. Phys. **109**, 07B912 (2011).

141 V. N. Krivorouchko and A. I. Marchenko, J. Appl. Phys. **109**, 083912 (2011).

142 B. Lenk, H. Ulrichs, F. Garbs, and M. Münzenberg, Phys. Rep. (to be published), and references therein.

143 C. Mathieu, *et al*, Phys. Rev. Lett. **81**, 3968 (1998); G. Gubbiotti, *et al*, J. Appl. Phys. **87**, 5633 (2000); Y. Roussigné, S. M. Chérif, C. Dugautier, and P. Moch, Phys. Rev. B **63**, 134429 (2001).

144 J. Jorzick, *et al*, Phys. Rev. Lett. **88**, 47204 (2002); J. P. Park, *et al*, Phys. Rev. Lett. **89**, 277201 (2002); A. Barman, *et al*, Phys. Rev. B **69**, 174426 (2004);

M. Bailleul, R. Höllinger, K. Perzlmaier, and C. Fermon, Phys. Rev. B **76**, 224401 (2007).

145 G. Gubbiotti, *et al*, J. Phys.: Condens. Matter. **16**, 7709 (2004).

146 V. V. Kruglyak, S. O. Demokritov, and D. Grundler, J. Phys. D: Appl. Phys. **43**, 264001 (2010), and references therein.

147 Y. Au, T. Davison, E. Ahmad, P. S. Keatley, R. J. Hicken, and V. V. Kruglyak, Appl. Phys. Lett. **98**, 122506 (2011).

148 P. Chu, D. L. Mills, and R. Arias, Phys. Rev. B **73**, 094405 (2006).

149 A. Khitun, M. Bao, and K. L. Wang, J. Phys. D: Appl. Phys. **43**, 264005 (2010).

150 The International Technology Roadmap for Semiconductors, http://www.itrs.net/Links/2009ITRS/Home2009.htm.

151 S. V. Vasiliev, V. V. Kruglyak, M. L. Sokolovskii, and A. N. Kuchko, J. Appl. Phys. **101**, 113919 (2007).

152 T. Schneider, A. Serga, B. Hillebrands, and M. Kostylev, Journal of Nanoelectronics and Optoelectronics **3**, 69 (2008).

153 A. A. Serga, T. Neumann, A. V. Chumak, and B. Hillebrands, Appl. Phys. Lett. **94**, 112501 (2009).

154 S. - K. Kim, K. - S. Lee, and D. - S. Han, Appl. Phys. Lett. **95**, 082507 (2009).

155 V. E. Demidov, S. Urazhdin, and S.O. Demokritov, Appl. Phys. Lett. **95**, 262509 (2009).

156 H. Al-Wahsh, Eur. Phys. J. B **73**, 527 (2010).

157 D. V. Berkov and N. L. Gorn, J. Phys. D – Appl. Phys. 41, 164013 (2008); http://www.micromagus.de/.

158 B. C. Choi, J. Rudge, M. R. Freeman, Y. K. Hong, and Q. F. Xiao, IEEE Trans. Magn. **43**, 2 (2007); http://llgmicro.home.mindspring.com/.

159 S. Bance, T. Schrefl, G. Hrkac, A. Goncharov, D. A. Allwood, and J. Dean, J. Appl. Phys. **103**, 07E735 (2008); http://magnet.atp.tuwien.ac.at/scholz/magpar/

160 H. Fangohr, G. Bordignon, M. Franchin, A. Knittel, P. A. J. de Groot, and T. Fischbacher, J. Appl. Phys. **105**, 07D529 (2009); http://www.soton.ac.uk/~fangohr/nsim/nmag/

161 The magnetization of saturation Ms $=14\cdot10^5$ A/m, the gyromagnetic ratio g = 2.1, and the exchange constant $A = 3\cdot10^{-11}$ J/m.

162 We note that, in general, the corresponding amplitudes are not equal since they correspond to spin waves propagating in opposite directions

163 The summation of the two amplitudes is required to avoid errors connected with the decreases of amplitude of either reflected or transmitted wave due to physical reasons (interference etc).

164 See any textbook in solid state physics, e.g. C. Kittel, *Introduction to Solid State Physics* (John Wiley & Sons, New York, Chichester, 1996).

165 V. V. Kruglyak, M. L. Sokolovskii, V. S. Tkachenko, and A. N. Kuchko, J. Appl. Phys. **99**, 08C906 (2006).

166 E. Schlömann, J Appl. Phys. **35**, 159 (1964); *ibid*. **35**, 167 (1964).

167 H. Al-Wahsh, E. H. El Boudouti, B. Djafari-Rouhani, A. Akjouj, T. Mrabti, and L. Dobrzynski, Phys. Rev. B **78**, 075401 (2008).